Magnetic and photocatalytic studies of electrically conducting Ni/NiO nanocomposites in carbon matrix

Thesis submitted to

Cochin University of Science and Technology

in partial fulfilment of the requirements

for the award of the degree of

Doctor of Philosophy

In

Physics

By

Ganeshchandra Prabhu .V

Nano Functional Materials Lab

Department of Physics

Cochin University of Science and Technology

Kochi- 682 022, Kerala, India

August 2018

Magnetic and photocatalytic studies of electrically conducting Ni/NiO nanocomposites in carbon matrix

Ph.D. thesis in the field of Physics

Author:

Ganeshchandra Prabhu .V
Nano Functional Materials Laboratory
Department of Physics
Cochin University of Science and Technology
Cochin - 682 022, Kerala, India.
Email: ganeshchandra.v@gmail.com.

Supervisor:

Prof. M. Junaid Bushiri
Nano Functional Materials Laboratory
Department of Physics
Cochin University of Science and Technology
Cochin - 682 022, Kerala, India.
Email: junaidbushiri@gmail.com
Front cover:

August 2018

Department of Physics
Cochin University of Science and Technology
Cochin- 682 022, Kerala, India

Dr. M. Junaid Bushiri
Professor
Department of Physics
Cochin University of Science and Technology
Cochin- 682 022, Kerala, India.

Certificate

*Certified that the work presented in this thesis entitled "**Magnetic and photocatalytic studies of electrically conducting Ni/NiO nanocomposites in carbon matrix**" submitted by Mr.Ganeshchandra Prabhu .V in partial fulfilment of the requirements for the degree of Doctor of Philosophy in Physics to Cochin University of Science and Technology, is an authentic and bonafide record of the original research work carried out by him under my supervision at the Department of Physics. Further, the results embodied in this thesis, in full or in part, have not been submitted previously for the award of any degree. All the relevant corrections and modifications suggested by the audience during the pre-synopsis seminar and recommended by the Doctoral committee have been incorporated in the thesis.*

Cochin -22
Date: 21-08-2018

Prof. M. Junaid Bushiri
(Supervising Guide)

Phone: +91-4842577404 Fax: 91 4842577595, Email: junaidbushiri@cusat.ac.in

Declaration

Certified that the work presented in the proposed thesis entitled "**Magnetic and photocatalytic studies of electrically conducting Ni/NiO nanocomposites in carbon matrix"** is based on the original work done by me under the guidance of Dr. M. Junaid Bushiri, Professor, Department of Physics, Cochin University of Science and Technology, Cochin–22, India and it has not been included in any other thesis submitted previously for the award of any degree.

Place : Cochin – 22 *Ganeshchandraprabhu .V*

Dated: / /2018

Acknowledgements

It is very pleasure to know that lots of people had influenced me during my PhD time and their contributions in making of my thesis. Words will not be enough to express my gratitude to my family members, teachers and friends. I recollect all my teachers from school days who inspired me a lot in the area of science particularly in physics.

At this juncture first I would like to thank Prof. M. Junaid Bushiri, my supervising guide and Head of the Department of Physics, CUSAT for his valueble advice, help and support throughout the research period. He spent a lot of time in hearing me and discussing the new frontiers of research problems. I would like to express my whole hearted gratitude towards him.

I express my sincere thanks to all the former heads of the Department of Physics, CUSAT Prof .S. Jayalekshmi, Prof. B. Pradeep, Prof. M.R. Anantharaman for proving and permitting me to use the research facilities in the department. I would like to sincerely thank Prof. M. K. Jayaraj and Prof. Titus. K. Mathew, Doctoral committee members for their valuable support, advice and help. I also thank all the teachers and non- teaching staff in Department of Physics, CUSAT for their kind help and support.

I am very happy to express my thanks especially Prof. S. Jayalekshmi and Mr. Anil kumar K M for helping to carryout d.c conductivity measurement of my samples in their lab.

I would like to thank my School teacher Mr. Jaydeep Shenoy who inspired me in the fundamental area of science especially physics.

I am obliged to Prof. M.K. Jayaraj, Professor Department of Physics, and CUSAT for XRD and Raman analysis. I also thank Dr. Senoy Thomas, Assistant Professor, Department of Physics, and CUSAT for fruitful discussion of my research work.

I thank Dr. Shibu .M. Eppen, SAIF, STIC, CUSAT for TGA, SEM analysis. I also thank to Dr. Anuradha Ashok and Mr. Vijayaraghavan, PSG, Institute of Advanced Studies, Peelamedu, Tamilnadu for TEM analysis.

I am obliged to Mr. Sivaramakrishnan, SAIF, IIT Madras for VSM analysis. I would like thank Mr.Sarath, Amritha Institute of Medical Science for XPS measurement.

I acknowledge University Grants Commission for providing me junior research fellowship and Teacher fellowship under Faculty Devolvement Program.

The research period in Nano-Functional Materials lab was joyful and words will be enough for the cooperation provided by my lab mates. I express my gratitude towards my lab members, Bini, Shajira, Sajan, Vinod, Satheesh, Rasheed, Sagar, Beena, Johncy, Divya, Haseena, M.Phil and M.sc. Students for their help and support. I thank all the research scholars in Department of Physics, CUSAT for their kind support and cooperation.

I have no words to express my gratitude and feelings towards my mother, father, wife, brothers and other members of family for their help and moral support.

Lastly I thank all my well-wishers and friends who have given by unbiased supporting for completing my thesis. Above all, I thank God Almighty.

Dedicated to my family and teachers

Contents

List of Figures

Preface

Research on nanomaterials with multifunctional properties which can provide better performance has got attention of the scientific community because of its technological applications. Among the multifunctional materials, a single material having conducting, magnetic and photocatalytic properties are useful for the fabrication of multifunctional devices. Investigations on these novel materials are focus of research recently in order to explore the possibility to use it for magnetic data storage application, treatment of waste water from textile industries and as conducting magnetic ink etc. A combination of metallic nickel (Ni) and nickel oxide (NiO) is a good multifunctional material which posses magnetic exchange bias, room temperature coercivity, electrical conductivity as well as photocatalytic properties. Interestingly, Ni is a conducting ferromagnetic material whereas NiO is semiconducting antiferromagnetic material. Nanoparticles of these materials can be protected from further oxidation if they are impregnated into the amorphous or crystalline non magnetic carbon matrix. Crystalline carbon materials such as graphite, graphene and multiwalled carbon nano tubes (MWCNT) can be used for the above purpose. These matrix materials can reduce the magnetic interactions of magnetic moments of adjacent Ni atoms, consequently enhancement of the magnetic coercivity of these materials.

The present work is focused on the synthesis of Ni/NiO nanocomposites in amorphous/crystalline carbon matrix using precursor salts of Ni/NiO and with carbon source by solution combustion method. The samples are characterized using XRD, FTIR, Raman, TEM, SAED, SEM, EDAX, XPS and CHN etc.. Magnetic, conducting (*d.c*) and photocatalytic properties of these materials are also investigated.

Chapter 1 describes the crystal structure of Ni and NiO, basics of electrical conductivity, photocatalysis, magnetism and surface plasmon resonance (SPR) properties etc.. Apart from that an extensive review of earlier works of nickel related materials is also presented in this chapter. **Chapter 2** focuses on the fundamental principles of characterization tools like XRD, FTIR, SEM,EDAX, Raman, XPS,TEM, SAED, CHN,VSM, four probe method for conductivity (*d.c*) measurement used in the present work.

Chapter 3 deals with the synthesis of Nickel rich Ni/NiO nanocomposites in amorphous carbon matrix by solution combustion method with nickel acetate as oxidizer and citric acid as fuel. An effort is also made to understand the effect of quantity of nitric acid (HNO_3) used along with precursor solution in the combustion reaction for the formation of NiO. This chapter also discusses the temperature dependent *d.c* conductivity, photodegradation efficiency and magnetic properties of Ni rich Ni/NiO nanocomposites. *d.c* conductivity studies show that Ni rich Ni/NiO behaves like metallic conductors. Photocatalytic efficiency increases with increase of Ni content which may be attributed to SPR of conduction electron in the Ni nanoparticles. Magnetic studies reveal that saturation magnetization of Ni rich Ni/NiO nanocomposites decreases with increase in the quantity of HNO_3 used along with precursor solution for the combustion synthesis. Unintentionally incorporated carbon during the combustion synthesis of Ni rich Ni/NiO decrease the exchange interaction between the Ni and NiO and which reduces the magnitude of exchange bias (EB).

Chapter 4 describes the synthesis of NiO rich Ni/NiO nanocomposites using solution combustion method. This chapter also includes the effect of fuel to oxidiser ratio on the *d.c* conductivity,

photocatalytic and magnetic properties of Ni/NiO nanocomposites. Raman studies reveals that amorphous carbon matrix exists in Ni/NiO nanocomposites, since the intensity ratio ($I_D/I_{G)}$ of Raman band corresponds to the defect related carbon (I_D) to graphitic carbon (I_G) is more than 1. It is found that *d.c* electrical conductivity of NiO rich Ni/NiO nanocomposites increases with respect to temperature due to the presence of semiconducting NiO. Thermal activation energy and photodegradation efficiency is increased with respect to Ni content of the Ni/NiO. It is also found that magnetic coercivity is increased with NiO content in Ni/NiO.

Chapter 5 deals with the synthesis of Ni rich Ni/NiO embedded in graphite and graphene matrix using combustion method. Raman analysis shows that I_D/I_G ratio is less than 1, which suggests that Ni rich Ni/NiO is embedded in crystalline matrix. Electrical conductivity (*d.c*) of Ni/NiO embedded in graphitic matrix shows higher conductivity than Ni/NiO composites embedded in graphene. Photodegradation efficiency of Ni/NiO nanocomposites embedded in graphene is higher than that of Ni/NiO in graphite and may be due to larger surface area of graphene. Wrapping of magnetic moment of nickel can be effectively done with graphite than graphene which leads to the increase of magnetic coercivity of Ni/NiO embedded in graphite.

Chapter 6 discusses the combustion synthesis of Ni rich Ni/NiO/MWCNT nanocomposites with MWCNT and precursor salt of Ni/NiO. From the Raman analysis it is found that crystallinity of MWCNT in Ni/NiO/MWCNT is higher than virgin MWCNT, the enhancement in crystallinity leads to the reduction in conductivity compared to Ni rich Ni/NiO. Lower order conductivity of the Ni rich Ni/NiO/MWCNT

nanocomposites decreases the photodegradation efficiency of the material because photodegradation process is related to conductivity. The presence of MWCNT matrix prevents the interaction of magnetic moments of the adjacent magnetic clusters of Ni which leads to the enhancement of coercivity of the material to 108 Oe when compared to Ni rich Ni/NiO. **Chapter 7,** gives the summary of the results presented in the thesis and discusses the scope for future studies.

List of publications

Journal papers

1) **V. Ganeshchandra Prabhu**, P.S. Shajira, N.Lakshmi, M.Junaid Bushiri, J. Phys. Chem. Solids **87** 238 (2015). "Magnetic properties of Ni/NiO nanocomposites synthesized by one step solution combustion method" (included in this thesis)
2) **V. Ganeshchandra Prabhu**, Abdul Rasheed Paloly, N.G. Divya, M. Junaid Bushiri, Mater. Sci. Eng., B **228** 132 (2018). "Photocatalytic and ferromagnetic properties of electrically conducting multifunctional Ni/NiO nanocomposites in amorphous carbon matrix" (included in this thesis)
3) P.S. Shajira, M. Junaid Bushiri, Bini.B.Nair, **V. Ganeshchandra Prabhu** Journal of Luminescence**145** 425 (2014) "Energy band structure investigation of blue and green light emitting Mg doped SnO_2 nanostructures synthesized by combustion method".
4) P.S.Shajira,**V.Ganeshchandra Prabhu,** M.JunaidBushiri J. Phys. Chem. Solids **87** 244 (2015) "Sunlight assisted photodegradation by tin oxide quantum dots".

Conference papers

1) Synthesis of Ni/NiO composites", **V.Ganeshchandra prabhu,** M. Junaid Bushiri, National conference on advanced nanomaterials February 6-7, 2012, Periyar university, Salem.
2) "Magnetic studies of Nickel nano particles" **V. Ganeshchandra prabhu**, M. Junaid Bushiri, National conferrence on biotic and abiotic moloecules-Their health effects and therapeutic application, 24^{th} -25^{th} February 2012 Sri venkateswara university, Thirupathi.

Chapter-1

Contents

Introduction; Electrical Conductivity, Photocatalysis and Magnetism

1.1 Introduction

Materials in the range 1 to 100 nm have fascinated the scientific community due to its enhanced physical properties when compared to bulk counter parts. These materials play important role in improving the quality of the life of modern society. Recent developments in nanotechnology made nanoparticles to be used in medical imaging, disease diagnosis, cancer treatment etc. Nanoparticles especially having magnetic properties are

important because of its use in magnetic data storage, drug delivery, water treatment etc. Faster and smaller computers which consumes less power is the recent demand of modern society and it can be only realized through progresses in the area of nanotechnology. Recently, nanomaterial with multifunctional properties such as conducting, magnetic and photocatalytic are explored by the researchers. Photocatalytic materials having magnetic properties are desired as they can be removed easily by using the magnets once the photoreaction is completed from the treated solution.

1.2 Introduction to Nickel

Nickel is one of the important metallic material with fascinating properties. It is silvery white, hard and ductile transition metal, which belongs to group VIIIB of the periodic table. Atomic number of Ni is 28 with electronic configuration [Ar] $3d^8$ $4s^2$ having atomic weight of 58.69. Nickel crystallizes mostly in face centered (fcc) cubic crystalline system, its lattice parameter and atomic radius are 0.352 nm and 0.124 nm respectively. Nickel also exists with hexagonal close packing (hcp) crystalline structure. Nickel is a transition metal which shows multi oxidation states +2, +3 and +4 with a common state +2 [Tundermann *et al*; 2005]. When compared to iron, cobalt and copper nickel is stable in +2 oxidation state in aqueous solution [Kerfoot; 2002]. Nickel is an important coinage metal, its alloys with other elements are corrosion resistive and heat resistive. Its alloys are commonly used for making jewelleries, stainless steel and other metallic alloys with potential applications. Nickel protects the material from corrosion and useful for plating metals. Nickel is an important catalyst and is widely used as an industrial catalyst. It is one of the important components of Ni-Cd batteries.

1.3 Introduction to Nickel Oxide nanoparticles (NiO)

Nickel oxide (NiO) is one of the transition metal oxides which have been investigated as a type of important inorganic materials [Wu *et al*; 2007]. Bunsenite is the mineral of the nickel (II) oxide. NiO has crystal structure similar to NaCl with octahedral Ni (II) and O^{-2} sites. NiO usually shows nonstoichiometry. If the stoichiometry is 1:1 then the colour of NiO appears in green. If the stoichiometry deviates from 1:1 then colour of NiO becomes black. NiO is a stable wide band gap material with an energy band gap varies from 3.6 to 4 eV and exhibits semiconducting behavior [Sato *et al*; 1993]. NiO is found in multi oxidation state like Ni_2O_3 and NiO_2. NiO received large amount of attention in the recent years due to its wide range of applications in catalysis, battery cathodes and gas sensors [Dooley *et al*; 1994, Yang *et al*; 1999, Miller *et al*; 1997]. As NiO is a p-type semiconductor, it finds uses in the fabrication of transparent p-type semiconductor layers. Another area where NiO is widely used is in dye sensitized photocathode [Nikolaou *et al*; 2017]. NiO has been an inspiring topic of research since it is a low cost ion storage material [El-Kemary *et al*; 2013].

Nanosized materials have fascinated the research community due to its unusual physical and chemical properties compared to the bulk materials. These materials have potential application in the fields such as catalysts, drug delivery materials, photonic materials and battery materials. Among such materials transition metal oxides have gained much importance due to their wide range of applications.

1.4. Electrical Conductivity

Electronic transport properties of the materials can be studied by measuring the electrical conductivity of the material. The equation to find the conductivity of the material is given by $\sigma = N_f e^2\tau/m$, where N_f is the number of electrons per unit volume, e is the electronic charge, τ is the relaxation time and m is mass of the electron. Conductivity depends on the temperature and by measuring the electrical conductivity as function of temperature fundamental mechanisms of electrical conduction in solids can be studied. The temperature dependent conductivity of a material can be studied by the Arrhenius equation $\sigma T = \sigma_0 \exp [-E_a/ kT]$. From this relation activation energy can be calculated from a plot of $\ln\sigma_T$ versus 1000/T [Hummel; 2010].

1.5. Photocatalysis in Semiconductors

Industrial contaminants caused by the industries produce major environmental issues, they must be addressed seriously. Consumer goods industry plays major role using synthetic dyes. Commercially about 10,000 tons of dyes are manufactured per year [Double *et al*; 2005] and during its production, about 12 % is lost [Jan *et al*; 2013, Peternel *et al*; 2007] and become part of industrial effluents which are stained, toxic and cancerous. As these dyes are resistant to light, different techniques must be used to remediate such issues. One of the important techniques that can be used to disintegrate contaminants dissolved in water is semiconductor based photocatalysis. There are several advantages of using semiconductor photocatalysis over conventional oxidation technique used for the treatment of dyes contained in industrial waste water. There may be possibility of

complete mineralization of the contaminants on the other hand the use of solar light restrict the use of additional chemicals. Interestingly, these experiments can be performed at room temperature [Rajesh *et al*; 2007]. Semiconductor material like ZnO, TiO_2, and NiO can be used as catalysts because of their relatively high stability, negligible cost, high efficiency and nontoxicity [Jan *et al*; 2013, Hayat *et al*; 2011]. In the past a few years several of such photocatalysts have been developed by the researchers and some of them are WO_3, SnO_2, ZrO_2, CeO_2, CdS and ZnS [Dong *et al*; 2017, Kim *et al*; 2016, Polisetti *et al*; 2011, Neppolian *et al* ; 2002].

1.6 Introduction to magnetic materials

1.6.1 Introduction

The fundamental idea of magnetism begins with the discovery of magnetite (Fe_3O_4) which has the power of attracting iron. The name of this mineral is related to the district of Magnesia in Turkey and it is a Greek word of Magnesia. In ancient time Greeks knew that when magnetite was rubbed with iron it become magnetic. Sufficiently polished and shaped piece of magnetite could float in the water, turn in the direction of north and south. This idea was used to make mariner's compass i.e if iron needle pivoted is previously rubbed with magnetite it points towards north. The north pointing behaviour of magnetite in old English is known as loadstone which means 'waystone'.

Englishman William Gilbert (1540-1603) who pioneered the research on magnets and he published his book 'On the magnet' in 1600. There are many innovations in manufacturing of magnets is developed. The

major technique is rubbing iron or steel with loadstone. It was during 1825 first electromagnet was made after the discovery of in 1820 by Hans Christian Oersted (1775-1851). The great discovery was current carrying conductor can produce magnetic field. New era was born after invention of electromagnet and research on magnetic materials gained momentum as powerful fields could be produced by using the electromagnet than by using loadstone.

1.6.2. Types of magnetism

1.6.2.1 Diamagnetism

Materials having negative magnetic susceptibility (χ= -1) are called diamagnetic one. These materials are not having net magnetic moment and react in a peculiar manner with respect to the applied field. In elemental form these materials are having completely filled electronic shells. Langevin theoretically explained with classical theory on origin of diamagentism [Langevin; 1905]. Electric charges in diamagnetic materials are partially shielded by the interior of the body from the magnetic field and hence produce small negative susceptibility [Kannan; 2016]. Electronic orbits precess around the direction of the applied magnetic field and precession direction is opposite to the external field resulting in susceptibility small and negative. Semiconductors with strong covalent bonding, ionic solids, rare gases like He, Ne, Ar , poly atomic gases like H_2, N_2, C (diamond), Si, Ge etc. and some of the superconducting materials belongs to this group of materials [Cullity *et al*; 2009].

1.6.2.2. Paramagnetism

The magnetic susceptibility of these materials is usually small and it shows positive values. If there is no interaction between magnetic moments in a material at ambient conditions, these moments may be randomly oriented. This phenomenon generally occurs in materials since thermal energy is higher than the magnetic energy required for aligning the moments in a particular direction. In the absence of external magnetic field, magnetic moments may be randomly aligned in all direction consequently its net magnetic moment M is zero. The peculiar property of paramagnetic substance is that when an external field is applied then some of the atomic moments will be aligning in the direction of that external field and net magnetization M increases with respect to applied field giving positive susceptibility. More and more atomic moments will align in the field direction when the field strength is increased and total magnetization M is proportional to the external field. On increasing the temperature of the materials by keeping the external field constant then magnetization decreases, as magnetic moments align in random direction. Hence the magnetic susceptibility χ is inversely proportional to the applied temperature on materials. This can be mathematically expressed as $\chi \alpha 1/T$, Curie's law of paramagnetism, $\chi = C/T$ where C is called Curie's constant. The curie's law can be more generally written as $\chi = C/T-\theta$ and is called Curie-Weiss's law [Cullity *et al*; 2009] where θ has the dimension of temperature.

1.6.2.3 Ferromagnetism

These materials are different from diamagnetic and paramagnetic materials since these materials are having inherent magnetic domain even in

the absence of external applied field. Weiss in the year 1906 proposed molecular field theory for explaining ferromagnetism [Weiss; 1906]. Each atom has net magnetic moments as a result there exists strong, short range interaction between the magnetic moments which leads to the alignment of magnetic moments in a particular direction in ferromagnetic materials. Quantum physics can be effectively used to explain this type of interaction which is called exchange interaction. Magnetic domains are exists in ferromagnets, because atoms with magnetic moments are spontaneously magnetized. Interestingly, in a particular domain all magnetic moments are aligned in the same direction, these domains may be aligned in different direction and any two domains are separated with domain wall. Some of these materials in bulk form posses zero magnetic moment. The magnetic behavior of ferromagnets will be different under external magnetic field (H) when compared to diamagnets and paramagnets. These materials are having non-linear relationship between magnetization (M) and externally applied magnetic field (H). If the direction of external field is reversed the magnetization M would not retrace in the same direction with respect to initial behavior, magnetic hysteresis which is an important characteristics of ferromagnets. The maximum value of magnetization which is produced by applying large external field is called saturation magnetization M_s. The magnetization of a ferromagnetic material cannot grow beyond M_s. With increase in the temperature, the behavior of hysteresis retained but value of magnetization will be less. As the thermal energy is increased and enough to overcome the strong interaction between magnetic moments ferromagnet changes into paramagnet. The temperature at which such transition occurs is called critical temperature and M_s become zero at this temperature. At the

temperature T> T_C materials turn to paramagnets and obeys Curie-Weiss law of ferromagnets $\chi = C/T-T_C$ [Kittel; 1949].

1.6.2.4 Antiferromagnetism

The materials with small positive susceptibility at all temperatures falls in the category of antiferromagnets and susceptibilities vary with change in temperature. Neel explained theory of antiferromagnetism based on molecular field theory proposed by Weiss [Neel; 1932]. Temperature dependent magnetic properties of these materials are interesting as physics point of view. Magnetic susceptibility χ increases with the temperature up to a particular temperature initially (Neel temperature - T_N) beyond which, χ decreases as is the case with all other paramagnetic substance. These type of materials show antiferromagnetic behaviour only below T_N (below the room temperature) and above that is paramagnetic. Low temperature measurement is required in order to confirm whether the material is antiferromagnet or not. Ionic compounds like oxides, sulfides and chlorides mostly belong to antiferromagnets. The plot of $1/\chi$ vs T is a straight line above T_N and this line is extrapolated to negative temperature at $1/\chi = 0$.

$$1/\chi = T+\theta/C$$

or

$\chi = C/T+ \theta = C/ T- (-\theta)$ and hence the material obey Curie-Weiss law with negative value of θ.

There exists antiparallel arrangement of magnetic ions in these materials. There is a strong tendency to align in an antiparallel way below the critical temperature T_N, even in the absence of an applied field. Below the Neel temperature, thermal energy is too low so that it could not

randomize the magnetic moments to become the material paramagnet. Theoretically one can consider that the lattice of the antiferromagnetic materials are made of two sub lattices, magnetic moments of one lattice aligned in a particular direction, the magnetic moments of the other one aligned in the opposite direction.

1.6.2.5. Ferrimagnetism

Commercial importance of ferrimagneitc materials came in to picture only during 1933-1945 when Snoek and his collaborates developed ferrites in the Philips research laboratory in Netherlands [Smit *et al*; 1959]. Ferrimagnetic substances are like ferromagnetic one, as they have spontaneous magnetization. These materials are having magnetically saturated domains consequently magnetic saturation and hysteresis. At temperature less than Curie temperature (T_C) these materials posses spontaneous magnetization and above T_C they behave like paramagnets.

The magnetic ferrites are mainly classified into two

1. Cubic: Materials with common formula $MO\text{-}Fe_2O_3$ in which M is a divalent ion such as Fe, Mn, Ni, Mg, Co etc..[Cullity *et al*; 2009] and among these, cobalt ferries are magnetically hard and others are magnetically soft.
2. Hexagonal: some of the examples for this class of materials are strontium ferrites and barium ferrites and they are magnetically hard.

Ferrites have two crystallographic positions termed as A and B sites. The magnetic exchange force acting between an ion on A site and an ion on B site is negative as is in antiferromagnets. Interestingly, magnetic moment associated with ion in lattice site A is in one direction and B is in the opposite of the magnetic moment of ion in the lattice site A . However, in

ferrimagnets substances, the magnitudes of magnetic moments are not equal, hence there exist magnetization. Ferrimagnetism can there for be considered as imperfect or incomplete antiferromagnetism. Ferrimagnets were not considered as special class of materials but has wide applications just like ferromagnetic materials in industries.

1.6.2.6 Superparamagnetism

Superparamagnetism is a different type of magnetism exhibited by small ferromagnetic or ferrimagnetic nanoparticles with critical size mostly below 10 nm. When the size of nanoparticles is reduced near to quantum size, particle become single domain structures and shows superparamagnetic behaviour. In superparamagnetic nanoparticles, magnetic moments of individual atoms aggregate into one single domain with one giant magnetic moment. These materials are having hysteresis curve below its blocking temperature, and above this temperature the material behaves like the paramagnet. In the case of superparamagnetic materials in the absence of external field the net magnetization is zero. As the external magnetic field is applied nanoparticles behaves like paramagnet with one difference is that their magnetization susceptibility is much large hence they are called superparamagnetic.

1.7. Field dependent magnetization (M-H plot) of ferromagnetic materials

Ferromagnetic materials naturally having the magnetic domains which are divided into Wiess domains separated by domain wall called Bloch walls [Kittel C; 1949]. In particular Wiess domain magnetic moment posses uniform direction but adjacent domains are aligned in different

direction. When an external magnetic field is applied, the Bloch walls move and cause the magnetic domain align in the same direction as the external field. Domains which are already in the direction of external magnetic field expand more than the other domains. In the absence of the external magnetic field (H), different domains have different direction and the net magnetization is zero. As soon as the magnetic field is applied magnetic moment aligns in the direction of applied magnetic field and reaches its maximum value of magnetization. This magnetization is called saturation magnetization (M_S) and at this time all the domains grows and point in the direction which is same as that of external magnetic field. If the intensity of field is reduced magnetic moments starts to decrease. When the external magnetic field reaches its value to zero, ferromagnetic substance does not lose its magnetization. This magnetization is called remanant magnetization (M_r). This magnetization arises due to the presence of domain structure [Frenkel *et al*; 1930]. In order to demagnetize the material extra magnetic field must be applied in opposite direction. This magnetic field is called coercivity (H_c). If the application of magnetic field in opposite direction is continued then the magnetization (M) grows to its minimum value ($-M_S$). However, a large value of field is needed to demagnetize the material under investigation. The final curve represents the hysteresis loop which is characteristic of ferromagnetic material. Saturation magnetization is not related to material size and is influenced by chemical composition where as coercivity and remanant magnetization depends on the nature and size of the material. Magnetic susceptibility is fundamental magnetic property which gives the extent of ability of material to be magnetized by the external magnetic field (H). It is the ratio of magnetization (M) to the external field (H)

$$M = \chi H$$

$$\chi = M/H$$

1.8. Temperature dependent magnetization (M-T plot)

There are two types of M-T plots, Field cooling (FC) and Zero field cooling (ZFC). In field cooling process sample is cooled along with the presence of external magnetic field and magnetization measurement is done during heating the sample. In zero fields cooling samples are cooled without the application of external magnetic field and measurement of magnetization is done during heating of the sample with applying external magnetic field.

1.9. Soft and hard magnetic materials

Ferromagnetic material can be broadly classified as soft and hard magnetic material, soft magnetic material is a material which has high permeability and low coercive field [Kannan; 2016]. The main applications of soft magnetic material are in transformer cores, inductors, magnetic shielding etc. An example of soft magnetic materials is a single crystal of iron showing highest permeability when external field is applied along (100) direction. The magnetic coercivity of the soft magnetic material is of the order of 12 Oe and is easy to magnetize and demagnetize.

A hard magnetic material is characterized with high coercive force and low permeability, even in the presence of strong demagnetization field hard magnetic material retains their magnetization. Hard magnetic materials are used in making permanent magnets and the typical values of coercivity of hard magnets are around 30 KOe. These values show that hard magnets are hard to magnetize and demagnetize [Cullity et *al*; 2009]

1.10. Nanomagnetism

Nanomagnetism is a subject which deals with the study of material at least one dimension in the nanoscale region of 1 to 100 nm. It includes the study of properties and applications of magnetism of dispersed nanoparticles, nanodots, nanowire, thin film, nano grains and multilayers in the nano regime. Main difference of nano structured magnetic material when compared to their bulk counter parts are, their dimensions are of the order of characteristic length such as limiting size of magnetic domains and broken translation symmetry which causes reduced coordination number with broken exchange bonds and frustration. Nano objects that are close contact with system such as substrate in case of thin films and multilayer leads to strong interaction with its immediate neighborhood. These material have application in geology, magnetic recording, ferrofluids [Odenbach; 2006], drug delivery and magnetic hyperthermia treatment etc.

1.11. Magnetic nanoparticles in matrix system

Recently there has been lot of interest in synthesis and characterisation of magnetic material in different matrix system due to its novel properties. The peculiarity of such systems is, one can take advantage of both the components i.e. material which is incorporated into matrix and properties of matrix itself. Magnetic nanoparticles in isolated form has been studied because of its different application such as catalyst support [Elazab *et al*; 2015], emulsion formation [Oliveira *et al*; 2010], photocatalyst [Shan *et al*; 2015] and waste water treatment [Teixeira *et al*; 2012]. New surface properties and functionalities can be achieved when magnetic nanoparticles are coated with protective layer of different materials [Rossi *et al*; 2012]. Magnetic properties of nanoparticles embedded in non-magnetic matrix

have got importance in ferromagnetic resonance studies and show matrix material dependent magnetic properties [Guskos *et al*; 2007]. Important materials that are widely studied and used as matrix are carbon, silicon, polymer, zeolite etc. Carbon is non magnetic element and can be used as protective system as it has peculiar properties such as chemical stability, biocompatibility and possibility of surface modification [Fernanda *et al*; 2015]. It is an attractive matrix system to encapsulate the ferromagnetic transition metals as it provides the control over the particle size distribution [Zhao *et al*; 1996].

Among the different form of carbon, graphite, graphene and carbon nano tube (CNT) are extensively studied due to its novel properties. With the invention of CNTs by Iijima S in 1991[Iijima; 1991] the material became popular among research community due to its unique electronic, mechanical and chemical properties also usefulness in dispersion and stabilization of metal and semiconductor nanoparticles [Georgakilas *et al*; 2007]. Recently, several researchers has tried the synthesis of nanostructured materials like nanowires, nanodots or nanoparticles because of its immense importance in magnetic data storage [Tanase *et al*; 2007], electronic devices [Wang *et al*; 2010] as well as in biomedicines [Roca *et al*; 2009]. Because of this nanoparticles got highest interest due to its large magnetization. But they are not stable in ambient conditions and prone to oxidation easily. This may lead to loss of their magnetization [Gubin; 2009]. Also it is very difficult to synthesis isolated magnetic nanoparticles due to its large surface to volume ratio and tendency to agglomerate [Granitzer *et al*; 2011]. To overcome this, particles can be capped by either using carbon structures, metal oxide [Wei *et al*; 2010], silica [Joo *et al*;

2009] or surfactant [Shukla *et al*; 2009]. This prevents the magnetic exchange interaction and allows only dipolar coupling that influences magnetic behavior [Granitzer *et al*; 2011]. Recently, mesoporous silicon matrix has been used as matrix system due its advantage that it not only incorporates magnetic nanoparticles but also allows tuning of its morphology.

1.12. Exchange anisotropy/bias

Exchange anisotropy or exchange bias is small-particle effect which was discovered by W.H. Meiklejohn and C.P. Bean in 1956 [Meiklejohn *et al*; 1957]. This has been studied with high interest because of their widespread uses in data-reading heads of hard disk drives. There are three requirements for the formation of exchange anisotropy (1) in a material system, field cooling through $T_{N,}$ (2) intimate contact between FM and AFM and (3) strong crystalline anisotropy in FM. Field cooling is performed so that specimen as a whole is in a single magnetic easy direction. It is a physical phenomenon involving the exchange interaction at the interface between AFM and FM materials. It is usually observed in single-domain particles system contains a ferromagnetic and an antiferromagnetic system like in the case of cobalt and its oxide layer (Co-CoO). In this system Co is ferromagnetic and CoO is antiferromagnetic. In these types of materials the hysteresis loop is not symmetric at the origin and shifted to left. Recently, this phenomenon was observed in diverse systems, containing not only FM/AFM interface but also system containing interfaces that involve ferrimagnet or spin glass. Ferrimagnet and spin glass can perform as either FM or AFM [Kannan; 2016]. The combination of FM/AFM bilayers or heterostructures became important due to their wide applications in spintronics, sensors and high density data storage etc.

1.13. Surface Plasmon Resonance (SPR)

Surface plasmon resonance (SPR) is one of the important optical properties of metallic nanoparticles attributed to collective oscillation of conduction electrons induced by the electromagnetic field of light. Light interacts with metal nanoparticles thereby giving collective oscillation of free electrons in resonance with electric field of light [Jain *et al*; 2007]. Optical phenomenon of surface plasmon appears in a material when the size of the metallic nanoparticles is reduced to nanoscale. In the nano regime surface plasmon becomes important tool for optical probes as it enhances the amplification, concentration and manipulation of light [Gracia; 2011]. Gustav Mie theoretically explained surface plasmon assisted optical properties of metallic colloids. During the time of early civilization, at the end of bronze age (1000-1200 BC) glasses from northern Italy were coloured attributed to metallic Cu nanoparticles embedded in the glassy materials. Surface Plasmon resonance is a product of interaction of matter with electromagnetic radiation. When the metallic nanoparticles are illuminated by light, electrons are pushed to the surface of the nanoparticles as light exerts force on it. This creates electric dipole as negatively charged electrons and positively charged ion cores and are separated. The presence of this electric dipole inside the nanoparticles forms the electric field that is opposite to that of light. This makes the electron oscillates inside the nanoparticles with certain resonant frequency called plasmon frequency.

1.14. Combustion synthesis

Self propagating High temperature synthesis (SHS) or simply combustion method is a cost effective method for synthesizing wide variety of nano materials [Aruna *et al*; 2008]. Depending the physical nature and initial reactant used for the combustion method this method is classified in to three.

1. If the initial reactants are solid state it is called conventional SHS.
2. If the initial reaction medium is aqueous solution it called Solution combustion synthesis (SCS)
3. If the initial reaction medium is gas it is called gas phase combustion or flame reaction

1.14.1. Solution combustion synthesis (SCS)

Wide variety of nano size materials can be synthesized effectively by solution combustion synthesis (SCS) which is simple to carry out [Aruna *et al*; 2008]. SCS is unique method and occurs in a self sustained reaction of homogenous solution of oxidizer and fuel. In this method if we want the metal oxides then the precursors must be corresponding metal ion containing compound. It is usually called oxidizer. The fuel can be of different types. Examples for fuels are urea, glycine hydrazine, citric acid etc. SCS became popular as the method can be used to obtain nano-sized metal particles [Fu et *al*; 2003]. The importance of SCS gained momentum because, it is short process and various gas formed during the process can control the particle size growth. The fundamental principle of SCS is from the thermo- chemical reactions which occur in the field of propellants and explosives [Aruna *et al*: 2008]. If the element's valences are balanced within short period of time large amount of heat energy is released along

with different gas such as N_2 ,H_2O, and CO_2 [Sharma *et al*; 2011]. There are several factors which controls the maximum temperature occurred in combustion reaction. They are fuel to oxidizer ratio, initial furnace temperature, nature of fuel and quantity of initial precursor [Sharma *et al*; 2011]. In SCS method doping of other elements is easy as these elements can be merely poured during combustion process. In our SCS method fuel is taken as citric acid and oxidizer is nickel acetate.

1.15. Review of earlier works.

1.15.1 Nickel in nano form

Metallic nanoparticles in powder form have attracted the interest of the research community recently due to the novel electric, optical and magnetic properties. The physical, optical, thermal, mechanical and chemical properties of the metal nanoparticles are strongly dependent on their size and shape. From both theoretical and technological point of view, metal nanoparticles especially magnetic nanoparticles have gained much attention. Magnetic nanoparticles have potential applications for making ferrofluids, magnetic refrigeration systems, as a contrast agent in magnetic resonance imaging, catalysis and magnetic carrier for drug targeting [Park *et al*; 2005]. Finely powdered nickel is an important constituent of conducting paints, rechargeable batteries, chemical catalyst, microwave absorbing materials and magnetic recording media [Bai *et al* 2008]. As substitute for noble metal such as Pd, nickel is gaining importance in the development of base- metal-electrode multilayer ceramic capacitor [Bai *et al* 2008].

1.15.2. Synthesis of Nickel nanoparticles

Solution based synthesis routes are mostly reported for the synthesis of nickel nanoparticles. Bai *et al* synthesized nickel nanoparticles with uniform size, using the modified hydrazine reduction route [Bai *et al*; 2008]. Modified polyol process is used for the synthesis of nickel nanoparticles [Couto *et al*; 2007]. Reduction of nickel chloride with hydrazine with cationic water in oil microemulsion of water/CTAB/n hexnol is used for the synthesis of nickel nanoparticles [Chen *et al*; 2000]. Chen *et al* prepared nickel nanoparticles via thermal decomposition of nickel organometallic precursor in alkylamines [Chen *et al*; 2007]. Chemical reduction of nickel chloride with hydrazine gives nickel nanoparticles [Wu *et al*; 2010]. Derez synthesized nickel nanoparticles using solution combustion method using nickel nitrate-glycene-ammonium nitrate system [Derez; 2012]. Chandra *et al* synthesized nickel nanoparticles through solution reduction process [Chandra *et al*; 2014]. Wu *et al* prepared nickel nanoparticles by hydrazine reduction of nickel chloride in ethylene glycol at 60^{o}C [Wu *et al*; 2003]. Nickel nanoparticles with fcc and hcp structures were synthesized using nickel nitrate, vegetable oil, sucrose [Joseph *et al*; 2011]. Chemical reduction method gives nickel nanoparticles with crystalline size around 30 nm using the precursors nickel salt and hydrazine hydrate [Chaudhary *et al*; 2015].

1.15.3. Synthesis of NiO nano structures

Several synthesis routes are found in the literature for synthesizing NiO nanoparticles. Li *et al* in 2001 synthesized nanocrystalline nickel oxide by thermal decomposition of the of $NiC_2O_4.2H_2O$ obtained through the reaction between $Ni(NO_3).6H_2O$ and $H_2C_2O_4.2H_2O$ where solvent used was

ethanol [Li *et al* ; 2001]. El-Kemary *et al* prepared nickel oxide nanoparticles by the reaction of nickel chloride with hydrazine and then thermal decomposition of nickel hydroxide ($Ni(OH_2)$ nanoparticles [El-Kemary *et al*; 2013]. NiO nanoparticles were successfully synthesized through thermal decomposition of the (2,9-dimethyl-1,10-phenanthroline) $NiCl_2$ complex precursor at 400 °C. Uniform spherical NiO nanoparticles in the range of 10-20 nm were obtained using above method [Barakat *et al*; 2013]. Nanosized NiO was synthesized by co-precipitation method with nickel chloride hexahydrate and sodium hydroxide as precursors. From their XRD studies they found that as prepared NiO nanoparticles are cubic fcc structure with average size of 26 nm [Rahdar *et al*; 2015]. Dharmaraj *et al* synthesized NiO nanoparticles using nickel acetate and poly (vinyl acetate) precursor and obtained cubic nickel oxide nanoparticles with an average size of around 40-50 nm [Dharmaraj *et al*; 2006]. Pure and nano sized NiO particles with an average particle size of 15 nm can be synthesized through thermal decomposition of the $Ni(en)_3](NO_3)_2$ complex as a precursor. This method ensures the formation of uniform and spherical NiO nanoparticles with weak agglomeration and narrow size distribution [Farhadi *et al*; 2011]. Saghatforoush *et al* obtained initially $Ni(OH)_2$ nanostructures using hydrothermal route and then calcined $Ni(OH)_2$ to obtain NiO nanoparticles [Saghatforoush *et al*; 2012]. Zorkipli *et al* synthesized NiO nanoparticles through sol-gel method and obtained average diameter of NiO nanoparticles of approximately 32.9 nm [Zorkipli *et al*; 2016]. Using nickel acetate and sodium hydroxide as precursors mesoporous β-$(Ni(OH)_2$ is obtained by sonochemical synthesis in ionic liquid, then calcinated β-$(Ni(OH)_2$ at 285-425 ^oC for 4 hours for getting

NiO [Alammar *et al*; 2012]. Nandapure *et al* prepared (NiO) nanoparticles by coprecipitation method using nickel carbonate as precursor. [Nandapure *et al*; 2013]

1.15.4. Ni-NiO systems

Composite based nanomaterials have been attracted the research community due to its additional properties compared to single individual materials. Such composites may find their uses in a wide range of application over many fields. Among these, metal/metal oxides nanostructures either in the form of core-shell or simple composites has been studied over the past decade, due to its intriguing properties. Recently magnetic metal/metal oxide nanoparticles have gained importance, due to their biomedical applications [Hao *et al*; 2010]. Especially ferro magnetic/antiferromagneitic core-shell nanoparticles have attracted particular interest owing to their ability to overcome superparamagnetic limit for ultra high density recording [Skumryev *et al*; 2003]. Metal/metal oxide systems such as Ni/NiO, Fe/FeO and Co/CoO are so far studied because of their interesting applications and are good model systems for research and its effects in nano regime [Kremenovic *et al*; 2012]. One of the important effects studied in Co/CoO system was exchange bias (EB) by Meiklejohn and Bean [Meiklejohn *et al*; 1956].The phenomenon exchange bias is related to exchange anisotropy created at the interface between antiferromagnetic (AFM) and ferromagnetic (FM) materials [Nogues *et al*; 1999]. When FM and AFM interfaces are cooled through Neel temperature (T_N) of AFM, exchange bias is induced in FM [Meiklejohn; 1962].The condition to obtain this is Curie temperature T_C of FM must be larger than T_N. The effect of exchange interaction is the shift in the hysteresis loop

along the field axis and increase in coercivity [Nogués *et al*; 1999]. The T_C of the metals like Fe, Co and Ni is 1043, 1403 and 631 K respectively while their monoxides which are AFM in nature have T_N 198, 291, and 532 K respectively. For EB studies, Ni-NiO systems are good candidate as NiO has high T_N and it is possible to get EB at room temperature [Yao *et al* ; 2014]. Also compared to other FM metals described above Ni is less likely to get oxidized [Yao *et al*; 2014]. Recently there has been growing interest in magnetic properties of Ni-NiO systems in the form of nanocomposites such as exchange bias [Del Bianco *et al*; 2011, Kremenovic *et al*; 2012, Sharma *et al*; 2010]. Wen *et al* successfully demonstrated dye absorption capability of Ni/NiO nanocomposites and shown that this material could find use in lithium storage [Wen *et al*; 2011]. Ni-NiO in the form of core-shell structures has received considerable attention during the last decades. Nanostructured Ni-NiO has successfully shown that it can be used for selective binding and magnetic separation of histidine-tagged proteins [Lee *et al*; 2006]. Ni-NiO is also used in catalyzing the reduction of CO_2, anode material for Li-ion batteries, electrochemical energy storage and electrocatalyst for hydrogen evolution reaction [Tsai *et al*; 2011, Huang *et al*; 2015, Huang *et al*; 2006, Yan *et al*; 2013, Yan *et al*; 2015]. Also Ni/NiO is important material which finds application in microwave absorption [Liu *et al*; 2016]

1.15.5. Synthesis of Ni/NiO nanostructures/ nanocomposites

Several routes are found in the literature in order to synthesize the Ni-NiO nanostructure/ nanocomposites. Sakiyama *et al* fabricated mono-dispersed, Ni-NiO core-shell nanoparticles through pulsed laser ablation technique [Sakiyama *et al*; 2004]. Recently Chopra *et al* developed new

synthetic methodology using chemical synthesis followed by microwave irradiation for the synthesis of Ni/NiO core-shell nanoparticles with size in the range 6-40 nm [Chopra *et al*; 2010]. Zhou et al fabricated Ni–NiO core-shell nanoclusters with cubic shape, by magnetron-plasma-based cluster beam deposition (CBD) system. When the Ni clusters flew through the intermediate chamber with constant oxygen feeding, Ni–NiO core-shell structure was developed [Zhou *et al*; 2007]. Ni-NiO core-shell nanoparticles were obtained with ligand stabilized Ni nanoparticles initially prepared by solution chemistry and then followed by solution-phase oxidation [Johnston-Peck *et al*; 2009]. Partial mechanochemical reduction of NiO gives Ni-NiO nanocomposites [Nogues *et al*; 2008]. Initially, mechanical milling method from NiO coarse grained powder, and thereafter through reduction in H_2 gives Ni-NiO [Del Bianco *et al*; 2011]. Fraune *et al* made Ni/NiO wire from Ni/NiO bilayer using electron beam lithography, further processing through ion milling of ion beam sputtered thin films [Fraune *et al*; 2000]. In 2014 Yung *et al* prepared Ni-NiO nanoparticles on poly (diallyldimethyle ammonium chloride- modified graphene sheets using hydrothermal method at 90^o C with time duration of 24 hours [Yung *et al*; 2014].

1.15.6. Magnetic properties of Nickel nanoparticles

Ni nanoparticles with size ranging from 4 to 10 nm was synthesized and observed that magnetic behaviour is superparamagnetic at room temperature [Estournes *et al*;1997]. In 2000 Chen *et al* observed that nickel nanoparticles with average diameter 4.6 nm show superparamagnetic behavior. They also found that magnetic parameters such as saturation magnetization, remnant magnetization and coercivity to be 26.2 emu/g, 0.67

emu/g and 7.5 Oe respectively [Chen *et al*; 2000]. Fonseca *et al* studied Ni nanoparticles embedded in SiO_2 amorphous matrix and concluded that Ni nanoparticles are superparamagnetic above blocking temperature (T_B) <40 K. They also found that these nanoparticles does not exhibit exchange bias [Fonseca *et al*; 2002]. Nickel nanoparticles with a mean diameter of 12 nm gives saturation magnetization 32 emu/g , remanant magnetization 5 emu/g and coercivity 40 Oe respectively [Chen *et al* ; 2002]. Monodispersive nickel nanoparticles prepared through monosurfactant system showed superparamagnetic behaviour above blocking temperature 12 K [Hou *et al*; 2003]. Yoon *et al* synthesized an assembly of Ni nanoparticles in polymer film. They observed that particle size obtained is 1.5-3 nm and from magnetic measurement they found blocking temperature to be 9 K. As prepared Ni nanoparticles in polymer film shows superparamagnetic behaviour above T_B [Yoon *et al*; 2005]. From the temperature dependent magnetization it is observed that the blocking temperature of Ni nanoparticles of size 3, 11 nm was 12 and 80 K respectively and from the M-H studies coercivity of 3 nm size particles at 5 K is found to be 200 Oe [Hou *et al*; 2005]. Monodispersed nickel nanoparticles of hcp and fcc structure showed magnetic properties of hcp nickel which is different from fcc nickel nanoparticles [Chen *et al*; 2007]. Chang *et al* studied nickel nanoparticles distributed in dielectric liquid. Interestingly, they found that when external magnetic field is applied nickel nanoparticles move towards the direction of applied magnetic field. As the magnetic field is removed the particles again suspended in dielectric liquid [Chang *et al*; 2008]. Ni nano particles synthesized through solution combustion synthesis shows saturation magnetization 60emu/g, remanant magnetization 10.93 emu/g

and coercivity 68.11 Oe [Derez; 2012]. Single phase spherical Ni nanoparticles were prepared by He *et al* and found that Curie temperature, saturation magnetization, remnant magnetization increased with increase of particle size [He *et al*; 2013]. Electron beam irradiation can be used for the synthesis of Ni nanoparticles and found that as the electron beam dose is increased the saturation magnetization (M_S) and coercivity also increases [Lee *et al*; 2015]. In 2016 Ishizaki *et al* synthesised Ni nanoparticles from the precursors nickel acetonate, oleylamine, and troctylphosphine (TOP) etc. They observed that increase in TOP/Ni ratio decrease particle size and nickel nanoparticles become superparamagnetic at critical ratio of TOP/Ni as 0.8 [Ishizaki *et al*; 2016].

1.15.7. Magnetic properties of NiO nanoparticles

Bulk NiO is found to be antiferromagnetic in nature and its magnetic properties depends on particle size. In nano regime NiO nanoparticles are found to be showing anomalous magnetic behavior. NiO nanoparticles show superparamagnetic property and found that increase in magnetization with decrease of particles size. It is also observed that the blocking temperature (T_B) of NiO nanoparticles increases with increase in particle size [Gosh *et al*; 2006]. Tiwari *et al* in 2006 prepared NiO nanoparticles with different sizes. They found that NiO nanoparticles were having antiferromagnetic alignment at core and spin glass behaviour at the surface [Tiwari *et al*; 2005]. Anandan *et al* synthesized NiO nanoparticles with and without surfactant and found that both NiO nanoparticles show superparamagnetic behaviour [Anandan *et al*; 2012]. NiO nanoparticles with sizes in the range 3.5-12.4 nm showed feature one due to uncompensated magnetic spin of core and other due to freezing of

disordered surface spins of shells. [Duan *et al*; 2012]. Magnetic studies reveals that as prepared NiO nanosheets has ferromagnetic behavior with saturation magnetization (M_S) and coercivity field (H_C) of 1.38 emu/g and 117 Oe respectively [Alammar *et al*; 2012]. Fe doping in to the NiO contributed to increase in blocking temperature (T_B) which is shifted from 17 to 57 K. Also the coercivity is increased from 0.8 to 1.5 KOe as the Fe concentrations were increased [Kurokawa *et al*; 2013]. Bora *et al* studied magnetic properties of PANI/ NiO composite using alternating gradient magnetometer at 80 K temperature. They found that NiO nanoparticles exhibit ferromagnetic like behavior with coercivity $5x10^{-2}$ T and remanant magnetization (M_r) as $3.5x\ 10^{-4}$ emu/g [Bora *et al*; 2014]. Baran *et al* synthesized NiO nanoparticles by thermal decomposition of nickel hydroxide and magnetic behavior reveal that hysteresis loop was obtained for sample with annealing temperature up to 600^oC. Also it is found that remanence and coercivity decreased with increase of decomposition temperature T_d [Baran *et al*; 2014]. Pure and Mn doped NiO with average size 20 nm were synthesized by Layek *et al* in 2016 and their magnetic properties were studied. Pure NiO show weak ferromagnetism at room temperature whereas magnetic property increased with Mn doping. The net magnetization is highest for 2 % of Mn doping and decreases on further doping. The ferromagnetic curie temperature of 2 % Mn doped sample was found to be 623 K [Layek *et al*; 2016]. Magnetization measured at room temperature with different particles sizes shows increase of magnetization with decrease of particle size. It was also observed that magnetic measurement performed on 6 nm NiO nanoparticles show superparamagnetic behavior [Kalaie *et al*; 2016]. Liu *et al* investigated size

dependent magnetic properties of branch like nickel oxide and found that particle size below 12.8 nm show very weak ferromagnetism. NiO nanoparticles with branch like morphology have higher remanant magnetization and coercivity when compared to spherical like morphology [Liu *et al*; 2017].

1.15.8. Photocatalytic activity of Nickel Oxide (NiO)

Recently semiconductor heterojunction were used in photocatalysis. Among the different heterojunction photocatalysts, nickel oxide is proved to be an efficient photocatalyst . Hayat *et al* studied on photodegradation of phenol using nano nickel oxide, synthesized by the sol-gel method [Hayat *et al*; 2011]. In their communication they investigated the effect of laser UV radiation, amount of catalyst, pH, initial phenol concentration etc. Hameed *et al* used NiO as photocatalytic material for splitting of water. They found that the photon flux and particle density, stirring rate and laser beam diameter affected the production yield [Hameed *et al*; 2004]. Gondal *et al* compared the photocatalytic activity of NiO with other transition metal oxides and found that NiO gives maximum hydrogen production while its oxygen production was low [Gondal *et al*; 2004]. Photocatalytic activity of NiO depends on its morphology and its hierarchical structures showed high photocatalytic activity in decomposing acid red 1 and can be recycled using external magnetic field [Song *et al*; 2008]. In their study they found that NiO rod showed lower activity of 15 % after 200 min, while NiO microsphere showed significant activity of 93 % in the degradation of acid red 1 pollutant. Qamar *et al* studied the complete and efficient photocatalytic reduction Cr (VI) in the presence of nanostructured NiO, without the use of any additive. [Qamar *et al*; 2011]. Neda *et al* synthesized

degradation of cephalexin under Hg lamp irradiation [Neda *et al*; 2015]. Peng *et al* synthesized NiO/ZnO nanoparticles embedded in mesoporous SBA15 using two solvent method and they showed enhanced photodegradation of methyl orange [Peng *et al*; 2016]. NiO synthesised through template assisted process shows excellent photocatalytic activity against Congo red, in comparison with bulk NiO [Faezeh *et al*; 2012].

1.16. Motivation of the thesis and statement of research problem

As described previously, Ni is ferromagnetic metal and NiO is antiferromagnetic semiconductor several physical phenomena such as exchange bias could be expected from the combinations of these materials. The occurrence of exchange bias causes the increase in coercivity of the material which in turn increases the magnetic storage capacity. Contamination of water with industrial dyes is a serious problem faced by the flora and fauna of the ecosystem. Such problems have to be addressed using novel technology available to the scientific community. Photocatalysis can be used as one of the effective methods to remove the dyes present in the waste water from textile industries. Interestingly NiO is a p type semiconductor electron-hole pairs will be produced from it on interaction with light. These photogenerated electrons and holes play an important role in the photodegradation process of the industrial dyes. Further Ni/NiO nanocomposites show ferromagnetic properties and can be efficiently used for the photocatalytic degradation of the dyes present in the contaminated water. As conductivity of the material is related to the photocatalytic process, studies on *d.c* conducting nature of the Ni/NiO is interesting one in fundamental science point of view. Ni is known for its oxidization properties which undergo oxidation to form NiO at ambient

conditions. Uchikoshi *et al* has studied oxidation process of Ni particles and found that oxide layer formed on the Ni particles are of 2 nm which provides good thermal stability to fine Ni particles [Uchikoshi *et al*; 1994]. Recently, Karmhag *et al* has studied oxidation kinetics of Ni nanoparticles using thermo-gravimetric technique and their observation revealed that particles has thin initial oxide shell [Karmhag *et al*; 2001]. The structure of Ni nanoparticles could be varied by the effect of oxidation [Rellinghaus *et al*; 2001]. Further oxidation rate of pure Nickel can be accelerated by applying external stress [Zhou *et al;* 2010]. Functional performance of Ni nanoparticles are greatly influenced by the oxidation process, degradation occurs to these nanoparticles, which will affect its catalytic and ferromagnetic properties [Song *et al*; 2008]. Ni nanoparticles can be suitably protected with non magnetic environment like silica, carbon etc. which will also provide mechanical strength. Carbon is one of the best materials which can be used as a protective matrix for the Ni/NiO nanoparticles. Interestingly, precursor salts used for the solution combustion method itself provides the amorphous carbon in the as synthesised samples. It is also interesting to study the magnetic, conducting and photocatalytic behaviour of Ni/NiO nanoparticles embedded in carbonaceous materials like graphite, graphene, multiwalled carbon nanotube (MWCNT) etc. A multifunctional material having conducting, photocatalytic and magnetic properties is a best option for treating waste water containing industrial dyes, since the ferromagnetic photocatalytic material can be separated from the treated solution by applying external magnetic field. Semiconducting material which can initiate photocatalytic process in the presence of sunlight is better suited because it is a cost effective simple method for water treatment. As stated previously these

metallic semiconducting combination of materials have to be protected properly from its surroundings. In this context, present work is focussed on the synthesis of nanocomposites of Ni/NiO in amorphous carbon/graphite/graphene /MWCNT matrix using fast, cheap solution combustion method and to study its conducting, magnetic and photocatalytic properties in the presence of sunlight.

1.17 Objectives of the thesis

- To study the effect of nitric acid on the combustion synthesis of Ni/NiO nanocomposites.
- To optimise the experimental condition for the synthesis of NiO rich Ni/NiO nanocomposites.
- To investigate the conducting, photocatalytic and magnetic properties of nickel rich Ni/NiO and NiO rich Ni/NiO in amorphous carbon matrix obtained through combustion method.
- To synthesise Ni/NiO nanocomposites in graphite and graphene matrix using precursor salts of Ni/NiO and graphite/graphene with combustion method.
- To study the effect of graphite and graphene matrix on conducting, photocatalytic ad magnetic properties of Ni/Ni Onanocomposites.
- To synthesise Ni/NiO in MWCNT using precursor salts of Ni/NiO and MWCNT with combustion method.

- To study the role of MWCNT in conducting photocatalytic and magnetic properties of Ni/NiO nanocomposites.

- Correlation and interpretation of the results.

Chapter-2

Characterization tools

Contents

2.1 X-ray diffraction (XRD)

X-Ray diffraction is one of the important techniques used for the study of the materials basically its crystal structure and atomic spacing. Peculiarity of X-ray diffraction technique is that it is fast and non-destructive and requires feeble quantity of the sample [Cullity *et al*; 2001, Buerger; 1962]. The working principle behind the X-ray diffraction is the constructive interference, which occurs when monochromatic X-ray falls on the crystalline sample. This happens because the dimension of crystal system is same as the wavelength of X-rays. The typical energies of the X – rays are of the order of 3-8 keV.

Constructive interference produced due to the interaction of the incident rays with the sample is represented by $n\lambda = 2\ d \sin\theta$ where λ is the wavelength of X-Rays used; n is the integer; d is the inter-planar spacing and θ is the diffraction angle.

X-ray diffraction can be used for the identification of different phases present in crystalline materials. Some of the materials may undergo phase transition with respect to the application of temperature. The temperature dependent phase transition in materials can be studied by using this versatile non destructive technique. The important parts of X–ray diffractometer are X-Ray tube, a sample holder and X-ray detector.

Cathode ray tube basically consists of an electron source. The electrons are generated by heating the filament which is made of tungsten of the cathode ray tube. Electrons generated from the cathode ray tube are accelerated by the application of accelerating voltage towards a target material made of copper or molybdenum etc. Electrons with sufficient energy can eject the inner shell electrons of the target materials, the inner shell transition of electrons in the target material produces characteristic X-rays. Usually the characteristic X-ray spectrum consists of X-rays of different wavelength mostly K_α and K_β. K_α contains two parts $K_{\alpha1}$ and $K_{\alpha2}$, these wavelengths are separated with the aid of suitable monochromator for X-ray diffraction experiments. Further $K_{\alpha1}$ has shorter wavelength when compared to $K_{\alpha2}$ and has twice the intensity that of $K_{\alpha2}$. So $K_{\alpha1}$ is mostly used one. Cu, Fe, Mo, Cr are the commonly used target materials, and these target materials will be selected based on desirability of X-ray wavelength. Copper is the most commonly used target material which gives CuKα radiation with a wavelength of 1.5418 Å.

These x-rays are made into parallel beam by the collimator and collimated towards the sample fixed on sample holder. Intensity of the diffracted x-rays from the sample is recorded simultaneously by rotating the

sample and detector. The constructive interference attributed to interference of diffracted beams coming out from the crystalline sample gives the diffraction pattern which obeys Bragg's diffraction law [Bunaciu *et al*; 2015]. These peaks are detected by the detector which converts the signal into count rate, and is fed to output device such as printer or computer monitor. By scanning the sample through different 2θ range it is possible to get all the diffraction direction due to the random orientation of the powdered materials. A complete diffraction path of a crystal is unique in nature for particular materials, and is considered as finger print of the crystalline materials.

The average crystallite size of the sample can be calculated from the XRD data using Scherrer's [Cullity; 1976] formula

$d = 0.9 \lambda/\beta \cos \theta$

λ- wavelength of X- ray

β full width at half maximum (FWHM) intensity in radians

θ angle with respect to β is calculated.

Usually diffraction peaks are converted into d-spacing which identifies the compound because each compound has a set of unique d-spacing. The obtained X-Ray diffraction patterns are compared with standard files reported by joint committee on powder diffraction standards (JCPDS). The structure of amorphous material cannot be identified with that of X-ray diffractometer it is the one of the major limitation of this technique.

The present X-ray diffraction measurements of the samples were carried out with Rigku D max X-ray diffractometer using Cu Kα radiation

(λ = 1.5418 Å) and PANALYTICAL XPERT-PRO X-ray diffractometer with CuKα radiation (1.5404 Å) [Figure 2.1]

Fig.2.1 *(a) Rigku D max X ray diffractometer using Cu Kα radiation (λ = 1.5418 A^0) (b) PANALYTICAL XPERT-PRO X-ray diffractometer with CuKα radiation (1.5404 A^o) used for the analysis of the samples.*

2.2 Fourier Transform Infra red (FTIR) spectroscopy

It is an important vibrational spectroscopy technique used for the structural determination of materials. This technique is used for the identification of functional groups in crystalline as well as amorphous materials. Infrared (IR) radiation is the part of the electromagnetic spectrum, and is divided into three regions. These are far IR, mid IR and near IR region. Spectrum originated from molecular vibrations is in the mid IR region. It could be used for effective analysis of the both organic and inorganic samples under investigation. One important use of FTIR spectrometer is that it is possible to get the spectral information over a wide spectral range. FTIR techniques has improvised IR region by decreasing the time required to collect the data. The fundamental principle behind the IR

spectroscopy is that, when the IR radiation is passed through the sample, the sample absorbs IR radiation. The sample gives out IR spectrum corresponds to the fundamental vibration of the molecule present in material. The peculiarity of the IR spectroscopy is that, it is a unique technique gives out finger print of the functional groups.

Absorption or transmission peaks are obtained in an IR spectrum that represents the frequencies of vibration between the bonds of the atoms constituting the materials. From these distinct peaks, one can able to identify the different functional groups present in the materials (Banwell *et al*; 1994). In the FTIR apparatus, initially a collimated beam of radiation is directed towards interferometer from the source. The different parts of interferometer are composed of beam splitter B and two mirrors M_1 and M_2 similar to that of Michelson interferometer. In FTIR the infra red beam splitter is made of potassium bromide. This makes the beam splitter to reflect half of the radiation falling on it. Thus half of the radiation goes to M_1 and another half to M_2. The radiation from the mirrors returns along the same path and then recombines to single beam at the beam splitter.

If radiation is a monochromatic, recombined beam leaving B gives constructive or destructive interference that depends on the relative path lengths of B to M_1 and B to M_2. These interference patterns are recorded by the spectrometer in the absence of sample in the beam and kept as background. Then the measurement is repeated with sample in the beam. The final spectrum will be obtained by subtracting the background spectrum with aid of softwares and computer system [Banwell *et al*; 1994]. In FTIR spectrometer interference pattern produced by the IR rays coming

from the sample is collected simultaneously. The individual frequency from the spectrum is separated by means of Fourier transform. In our study we have used SHIMADZU IR Affinity -1 8400S FTIR spectrophotometer with KBr pellet technique (resolution of 4 cm^{-1}) to get the FTIR of the samples [Figure 2.2]

Fig.2.2 *SHIMADZU IR Affinity -1 FTIR spectrophotometer using KBr pellet technique with resolution of 4 cm-1 to get the FTIR used for sample analysis*

2.3 Fourier Transform Raman Spectroscopy (FT-Raman)

The basic principle of Raman spectroscopy which was discovered by C.V Raman in the year 1928. Sir C.V. Raman received Nobel prize in physics for this discovery known as Raman effect. When monochromatic radiation of a very narrow frequency is made to fall over the materials, the radiation will be scattered. The energy of the scattered radiation consist of incident radiation (Rayleigh scattering) and Raman scattering. Raman scattering contains discrete frequencies above and below incident radiation and are referred to as stokes and antistokes lines (Banwell *et al*; 1994).

Raman spectroscopy gives the information about functional group, molecular symmetry, nature of chemical bonds etc. in non destructive way. The physical origin of Raman spectra is attributed to vibration of molecules. The amplitude of the inherent vibration of the molecules will increase when a molecule interacts with monochromatic electromagnetic radiation corresponds to its vibrational or rotational frequencies. By exploiting the vibrational and rotational motion of molecules, Raman spectroscopy can detect the presence of organic and inorganic species in the sample. The energy difference between the excitation source and the scattered light from the sample is recorded. The difference in energy corresponds to vibrational or rotational transition in the molecule, specifically vibration which leads to the change in the polarizability of the molecules due to the interaction of electric field components from the electromagnetic radiation. When the energy of incident light loses to the material the emerging radiation will have lower energy and is termed as stokes Raman line. Otherwise we get antistokes Raman scattering in which molecule giving some energy to emerging radiation from the sample.

Lasers are mostly used for Raman spectroscopy measurement as an excitation source. In 1964 using Michelson interferometer Chantry *et al* demonstrated that near infra red source can be used as excitation source in recording Raman spectra [Chantry *et al*; 1964]. Good quality of FT Raman spectra was obtained only after the invention of laser, interferometer, detector and computer technology. The main advantage of combining interferrometry and Fourier transform methods is that it is possible to record the Raman spectra of the samples within a short period of time with high efficiency. The processing of high resolution Raman spectra could be

possible by means of FT-Raman technique similar to FTIR. FT Raman spectroscopy uses the near IR (Nd:YAG laser source with 1064 nm, this IR source will reduce the possible fluorescence from the sample. Further, the major advantage of above laser source is which limits the photolytic decomposition of sample. Also FT- Raman spectroscopy offers superior spectral resolution, frequency accuracy and relatively high output compared with a dispersion based spectrometer [Xue; 1997]. For practical purpose stokes Raman scattering are used since it has higher intensity than antistokes.

With advent of laser Raman spectroscopy becomes more precise and accurate measurement are possible. Instrumentation of Raman system consists of four major components. They are Excitation source usually laser, sample illumination system, light collection optics, filters and detector usually CCD or PMT is used.

In the present studies, a Horiba Jobin Yuon LabRAM HR system with a resolution in the order of 3 cm^{-1} equipped with He-Ne laser (632.8 nm) was used to record the Raman spectrum of the samples[Figure 2.3].

Fig.2.3 *Horiba Jobin Yuon LabRAM HR system with a resolution in the order of 3 cm^{-1} equipped with He-Ne laser (632.8 nm)*

2.4 Scanning Electron Microscope (SEM)

Scanning electron microscopy (SEM) is similar to light microscopy, with the difference that electrons are used in the place of photons and the techniques of image formation are different [Schroder; 1998]. Large magnified image of the sample can be obtained from an electron microscope. This is the main advantage of electron microscope over optical microscope. SEM is the device used to get the fine details about the surface nature, morphology, shape, size porosity etc of the material. It is the electronic equivalent of metallurgical or reflected light microscope [Watt; 1997].

The fundamental science of electron microscope is related to theory proposed by the De Broglie in the year 1923. He proposed that particles can have wave nature and hence electron can show both particle as well as wave nature. The wavelength of electron depends on the velocity of electron or accelerating voltage V given by

$$\lambda_e = \frac{1.22}{\sqrt{V}} \text{ (nm)} .$$

The interaction of electrons with matter can produce different effects i.e. they can be absorbed, emitted, reflected or transmitted. During the interaction of electron beam with the sample, mainly three types emission of electrons occur. They are secondary electron, backscattered electrons and Auger electrons. Electrons can be focused, deflected and accelerated by the application of electric field with desired strength. Back scattered and secondary electron can be detected by using suitable detectors and can be counted. It is possible to measure the energies of electrons.

The electron microscope consists of electron gun which can produce a stream of high energy electrons that scans through the sample surface in raster scan mode. Number of signals produced in SEM is detected by the detector and images are formed on the screen of CRT or television picture. Usually secondary electron mode is chosen to know the morphology of the sample since these electrons are about 1 nm less from the sample surface.

The other components of SEM include electron gun, a lens system, scanning coils, an electrons collector and cathode ray display tube (CRT). Typical electron energies of 10-30 K eV are used for imaging purpose for most of the samples. But if the sample is found to be insulator, the energy used becomes as low as several hundreds of eV. Usually imaging of conducting samples is possible in SEM. Non conducting samples can be made to conducting by pasting carbon tape over it. Tungsten hair pin filaments are used for the generation of electrons in SEM.

In the present study microstructure and morphology of the samples were examined by using JEOL JSM-6390 LV Model Scanning Electron Microscope (SEM) and Carl Zeiss, sigma HV model Field emission scanning electron microscopy (FE-SEM) [Figure 2.4].

Fig.2.4 *JEOL JSM-6390 LV Model Scanning Electron Microscope (SEM) and Carl Zeiss, sigma HV model Field emission scanning electron microscopy (FE-SEM) used for sample analysis*

2.5 Transmission electron microscopy (TEM)

Max Knoll and Ernst Ruska first invented Transmission electron microscopy (TEM) in 1931 [Egerton; 2005]. Transmission electron microscopy (TEM) is a microscopic technique for viewing highly magnified images of very small objects. Its working principle is similar to that of scanning electron microscope. The imaging is done mostly with the help of transmitted electrons from the sample. When the electron beam is transmitted through the sample, electrons scattered by this interaction, forms interference pattern, which again forms images of the sample. The signals responsible images can be detected with suitable electron detectors, the ultimate image could be formed on fluorescent screen or sensors such as CCD camera.

The expression for the relation between wavelength of the incident electron and accelerating voltage is given in the scanning electron microscopy section. Typical accelerating voltage for illumination of the sample is in the range 100 to 400 KV. Electron gun is used for the generation of electrons similar to that of SEM and is accelerated by applying the accelerating potentials. These electron beams are focused on the sample by electromagnetic condenser lens system. Diffraction patterns in the back focal plane and a magnified image in the image plane is formed by the transmitted and forward scattered electrons [Schroder; 1998]. Diffraction pattern formed by the interaction of electron beam and sample could be fed to the electronic recording devices.

TEM can be used to get bright field, dark field images from the sample [Schroder; 1998]. Transmitted electrons form the sample gives bright field images whereas diffracted beam of electrons give dark field images. TEM in diffraction mode gives electron diffraction pattern similar to that of the X-ray diffraction pattern.

During the past decades High Resolution Transmission Electron Microscopy (HRTEM) became popular and the images from these systems will give structural details at a spatial resolution of 0.2 nm [Smith; 1997]. Large diameter objective lens of HRTEM passes transmitted as well as diffraction beam. These two beams are combined on a single point gives the image.

Pure samples are required for TEM measurements, different steps are involved in sample preparation. First the given samples are

ultrasonicated in any fast evaporating organic solvent. Then sample is placed on the copper grid of a few mm in diameter and sample with copper grid is dried using a heater. In some cases carbon grids are used for sample handling.

In the present study A JEOL JEM 2100 model advanced analytical High Resolution Transmission Electron Microscope (HRTEM) operated at 200 KeV attached with EDAX set up was used for the TEM and HRTEM measurements [Figure 2.5].

Fig.2.5 *A JEOL JEM 2100 model advanced analytical High Resolution Transmission Electron Microscope (HRTEM) operated at 200 KeV attached with EDAX set up used for sample analysis in the present study.*

2.6 Selected Area Electron Diffraction (SAED)

Selected Area Electron Diffraction (SAED) is used for characterization of nano materials, it is a diffraction technique used with short wave length electron beams. This detector system is attached with TEM. This diffraction pattern from the sample is very useful to understand the crystal structure very small crystalline materials which cannot be detected with conventional X-ray diffraction method. In the case of single crystalline materials, a spot pattern can be obtained on the screen. If sample is polycrystalline or nano crystalline one can get ring like pattern from the sample. A series of diffuse patterns are formed for the sample with amorphous nature. From the rings "d" spacing can be calculated by unitary method i.e. initially finding the length of scale of pattern and then finding the diameter of the rings. The relation between wavelength λ, diameter D, d-spacing d and effective camera length L is given by $Dd = L \lambda$ [Flewitt *et al*; 2015].

2.7 UV-Vis-NIR Spectroscopy

UV-Vis-NIR spectroscopy is acronym of the Ultra Violet-Visible Near Infra Red spectroscopy. It is used to analyze the absorption or reflectance of the powdered samples and thin film samples. Absorption of photons by the sample depends on the nature of functional groups as well as nature of constituents present in the sample. The optical absorption coefficient α, direct and indirect band gap energy and the density of states samples can be determined by using this instrument. UV-Visible radiation from source is focused on to the sample. The incident beam is either absorbed, or reflected, some the rays will be transmitted. Transmitted light

after interacting with the samples is mostly collected using a detector and analyzed. The main components of the spectrometer are UV-VIS-NIR light source, sample holder, detector, allied optics and software. UV-VIS spectrometer can be configured to measure absorption of the powdered sample taking $BaSO_4$ as the reference. Light interacts with the sample and compares the intensity of light after absorption with the initial intensity. The absorbed intensity versus wavelength is recorded by the instrument.

UV-VIS spectrometer can also be used to find the concentration of absorbing materials in the sample. The absorbance of the material is related to its concentration according to the equation.

$A = \log (I_0/I) = \varepsilon C L$ where ε absorptivity of the material, C concentration of the absorbing material and L is path length.

The ε is material dependent and L is cuvette dependent properties, hence A is proportional to concentration C. In the present study the remanant methelyne blue solution obtained after treating with photocatalyst in presence of sunlight is taken in the sample cuvette and another bare cuvette is placed as reference. Then the absorption spectrum of methelyne blue solution is taken using UV-VIS-NIR spectroscopy from 800 to 200 nm.

In the present study JASCO V 570 UV-Vis NIR spectrometer is used for the analysis of the samples. It consists of deuterium lamp (190-350 nm) and a halogen lamp (330-2500 nm) and uses a single monochromator. The spectrometer has a resolution of 0.1nm in UV-Vis and 0.5nm in NIR [Figure 2.6].

Fig.2.6 *JASCO V 570 UV-Vis NIR spectrometer used for sample analysis*

2.8 Energy Dispersive X-ray (EDAX) spectroscopy

It is one of the analytical tool used to understand the elemental composition of the sample. This device is connected to SEM /TEM setup, this analysis requires high vacuum condition [Flewitt *et al*; 2015, Schroder *et al*; 1998]. When the electron beam is made to fall on the sample, the electrons expel the electron present in the inner shell of the atom comprising the sample. This process leaves a hole in the inner shell, an electron from the higher energy shell fills this hole emitting characteristic X-rays from the sample under investigation. The energy of the X-rays depends on the difference between the inner shell where the hole is created and outer shell from which electron is filled. By measuring the energy of the X-rays emitted by the specimen or sample can be used to identify the elements present in the sample. An X-ray detector, a pulse processor and a computer are additional requirements in a SEM for detecting the X-rays emitted from the sample due to the irradiation of electron beam on the sample.

2.9 CHNS Analysis

CHNS elemental analysor is used to quantitative detection of elements like carbon, hydrogen, nitrogen and sulphur in organic matrices and in other materials. Solids, liquids, volatile and viscous samples can be analysed with this instrument. CHNS analysis based on combustion of these elements which gives out In the combustion is converted Carbon dioxide by carbon; hydrogen to water, nitrogen to nitrogen gas/oxides of nitrogen and sulphur to sulphur dioxide. This measurement system requires high temperature combustion in an oxygen rich environment. After the combustion is completed combustion products are taken out from the combustion chamber by helium gas. Highly purified copper is used over which the combustion products are passed. Copper removes the oxygen and converts nitrogen to nitrogen gas. Detection of the gases are carried out by using gas chromatograph separation method. In order to quantify the amount of carbon, hydrogen, nitrogen and sulfur thermal conductivity detector is also used.

2.10 Thermogravimetric Ananlyis (TGA)

Thermal analysis system is an important instrument which can be used to study the temperature induced changes in a sample, properties of materials which changes with temperature. Thermal analysis measures the chemical and physical properties of a material with respect to heating of the sample or as a function of time. While doing the thermal analysis as function of time temperature of the system will be kept constant. From this test method, mass evolution of milligram-scale of the sample is possible. Different physical properties measured under TGA are enthalpy, thermal capacity and coefficient of heat expansion. It is possible to study reaction in

solid state, thermal degradation reactions, phase transitions ad phase diagrams. In TGA measuring, weight loss curve could give changes in sample composition, Thermal stability, and kinetic parameter for chemical reaction in the sample. In TGA mass change can occur physically as well as chemically. For example physical changes that happen during thermal analysis are gas adsorption, gas desorption, vaporization and sublimation whereas chemical changes occur are decomposition, break down reaction, gas reaction, chemisorptions. In some cases TGA is used to know the material purity and determine humidity. This versatile technique can also be used to study corrosion, gasification process and kinetic processes. Practically, materials under study are heated to degradation in controlled atmosphere and loss of weight in terms of temperature is recorded. The speed or extent of degradation depends on the material used and some of them can degrade faster or slower.

In thermal analysis system weight of the sample measured by means of balance is important parameter. It basically consists of a highly sensitive recording balance made of platinum, controlled by balance control system. Recording balance is attached with sample holder, in which experimental sample is taken. The sample holder system is integrated with a heating furnace. The pan of the balance along with sample is kept within the furnace where it is heated. Using thermocouple the temperature growth is measured. The heating rate of the sample is controlled by means of a temperature programming. Usually inert atmosphere sometimes in air or nitrogen atmosphere is preferred in order to confirm no oxidation reaction is occurring [Paul; 2008]. In the present study Perkin Elemer model TG/DTA measurement set up is used.

2.11 X-ray photoelectron spectroscopy (XPS)

X-ray photoelectron spectroscopic technique is basically worked on photoelectric effect proposed by Einstein. The oxidation state of atoms in material will be analysed based on the electron coming out from the sample while irradiating with highly energetic photon from the X-ray source. Generally electron spectroscopy is related to low energy electron ie. 20-2000 eV. Core level electrons can be ejected in XPS using X-ray photon of energy hυ. These ejected electron energy is then analysed by electron spectrometer. The kinetic energy E_K of electron is not an intrinsic material property as it depends on photon energy of X-rays employed [Jeffrey; 2013]. Hence binding energy of the electron is measured and analyzed. It gives information regarding the parent element and atomic energy level. The relationship between the parameter involved in the XPS experiment is $E_B = h\upsilon - E_K - W$ where hυ is incident photon energy, E_K is kinetic energy of electron, W spectrometer work function. These parameters are measurable and hence we can calculate binding energy E_B. The characteristic peaks in spectrum are the result of electron escaping without loses of energy.

XPS system basically consist of a high energetic x-ray source, an ultra high vacuum sample chamber, sample holder and electron detection system. These three components are kept in vacuum chamber usually ultra high vacuum regime. Primary source in XPS is mainly soft X-rays generally AlKα or MgKα. A data processing system will be connected in the above system in order to analyze the data and further processing. Using control electronics associated with the spectrometer one can select the binding energy. Energy of the electron ejected from the sample is analysed, which will give information about the oxidation state, binding energy etc.

In spectroscopist's notation the ejected electron is described by its quantum number. The scheme used for the transition of electrons is given by nlj. Here n represents principal quantum number with integer value like, 1,2,3 .. etc.. l shows the orbital angular momentum quantum number . This can also take values of 0, 1, 2, 3 etc, J represent l+s total angular quantum number. XPS is an electron based detection system, so it requires ultra high vacuum of the order of 10^{-7} Pa is required. In our XPS analysis, samples are examined using Kratos Axis Ultra with Alkα radiation.

2.12 Vibrating Sample Magnetometer (VSM)

Vibrating sample magnetometer (VSM) is used for the magnetic characterization of the magnetic specimens. It was first invented by S. Foner [Foner; 1959], later this instrument was modified and improvised [Krishnan *et al*; 1999)]. Using this instrument magnetic property of the material such as saturation magnetization (M_s) coercivity (H_c) remanence magnetization (M_r) and squarness ratio (M_r/M_s) can be measured.

Vibrating sample is working on the principle of electromagnetic induction invented by Faraday. This instrument is a versatile instrument for the investigation of magnetic properties of the solid materials. The first model of this instrument is developed by S. Foner in the year 1955 [Foner; 1959]. According to the Faraday principle the induced emf E is given by $E = -N\, d(BA \cos\theta)/ dt$ where N is the number of turns in the coil, A area of cross section, θ is the angle between field and direction normal to the coil.

The system consists of a sample holder, in which the sample can be loaded. The sample holder along with sample is allowed to kept in between powerful magnets, which is of the order of 1 to 7 Tesla in most cases. This generates magnetic dipole moment in the sample called a magnetic stray field. Further this magnetic specimen is vibrated or moved up and down with certain frequency and amplitude. On vibrating the sample within the magnetic field, the stray magnetic field within the sample will be fluctuated. Based on Faraday's law of induction this change in magnetic flux will induce an electric field in the pick-up coils proportionately thereby generating a current. These signals will be detected with a set of pick up coils and measured using lock in amplifier. These electronic components are configured with personal computer. Using the suitable software it could be understood that how much the sample is magnetized and how magnetization depends on the strength of the constant magnetic field. The current generated in the coil will depend only on the magnetic strength of the sample, which is independent of external magnetic field strength. Greater the magnetization of the sample, larger will be the induced current. If we set the particular field strength correspondingly signal is received by the probe and converted into a value of magnetic moment of the sample. By changing this constant field over a wide range a plot of magnetization versus magnetic field (M-H) could be obtained.

2.13 *d.c* electrical conductivity

d.c electrical conductivity of the samples are done with four probe method, it is a popular method to measure the *d.c* conductivity of the samples. A four probe set up consist of four equally spaced probes. These probes are made in contact with samples of unknown resistance. Current to

the specimen is supplied through the outer probes and the voltage is measured from the two inner probes. A Keithley 2400 source meter is used for the supplying current to the measurement system. Multimeter, computer and LabVIEW softwares are attached with *d.c* conductivity measurement system. Resistance of material can be easily deduced using Ohm's law given by V = IR.

The resistivity of the material can be written as $\rho = R\ l/a$ where "l" is the thickness of the pelletised sample "a" is the area of cross section. Since the conductivity of material is reciprocal its resistivity it can be calculated from resistivity. The conductivity is measured by changing the temperature from 303 to 403 K, using the local heating arrangement kept in vacuum. From the data obtained by varying the temperature, Arrhenius plots and conductivity verses temperature plots can be drawn. Activation energy can be calculated by the slope of the Arrhenius plot.

Chapter-3

Contents

Electrical, photocatalytic and magnetic properties of Nickel rich Ni/NiOnano composites synthesized by one step solution combustion method

3.1. Introduction

Nickel based nanostructures received increased attention because of their use in the fields of catalysis, fuel cell electrodes, gas sensors, supercapacitors, spintronic devices etc. [Wu *et al*; 2003, Murai *et al*; 1996, Hotovy *et al*; 2001, Nelson *et al*; 2003, Suzuki *et al*; 2013, Johll *et al*; 2014]. Among these, Ni/NiO is a good combination of materials in which Ni is a conducting ferromagnetic (FM) metal whereas NiO is a p-type semiconductor which has antiferromagnetic (AFM) behaviour. NiO posses high Neel temperature (T_N) for high temperature magnetic stabilization of metallic nanoparticles like cobalt [Toro *et al*; 2015].

Interestingly, FM and AFM combination of materials with core-shell, layered film, nanogranular and nanocomposite form have been investigated by researchers to know the physics of magnetic exchange bias (EB) phenomenon [Yuan ; 2010, Sharma *et al*; 2010, Nogues *et al*; 2008, Del Bianco *et al*; 2011,Yao *et al*; 2014, Sort *et al*; 1999]. The exchange

coupling in Ni/NiO system can be realized by field cooling the material from the temperature which is above the Neel temperature (T_N) of NiO, consequently material will show shift in hysteresis loop as well as increase in coercivity (H_c) of Ni. Varying Ni or NiO content in Ni/NiO system will modify the exchange interactions between Ni and NiO which results change in magnetic characteristics like exchange field (H_E) and coercivity (H_c) [Sharma *et al*; 2010, Yao *et al*; 2014]. Such tuning of magnetic properties of FM/AFM coupled materials makes it useful for fabricating magnetic recording devices and other magnetic based devices [Skumryev *et al*; 2003, Liu *et al* ; 2007]. Pollution from industries especially dyes from textile industries is a major concern, a vast variety of dyes are deposited in the environment as industrial effluents. These dyes can be treated with photocatalystic materials. In this scenario a material with conducting, photocatalytic and magnetic properties may be useful as one can exploit these properties according to the demand of the situation.

Synthesis methods have strong influence on quality, size distribution of grown crystals, microstructure and consequently the magnetic properties of materials. For the synthesis of Ni/NiO systems, different methods are found in the literature with special reference to tuning parameters of EB and H_c of Ni/NiO systems. Ni/NiO core-shell nanoparticles obtained by pulsed laser deposition technique have H_c of 316 Oe attributed to exchange coupling [Yuan; 2010]. Ni/NiO nanocomposites synthesized with thermal decomposition of nickel acetate have H_E and H_c of 890 Oe and 400 Oe respectively [Kremenovic *et al*; 2012]. Compared to previously mentioned growth methods, solution combustion synthesis (SCS) is relatively cost effective method for the synthesis of Ni/NiO nanocomposites [Wen *et al*;

2011, Deraz; 2012, Kang *et al*; 2015, Manukyan *et al*; 2013, Jung *et al*; 2005]. In the present chapter, we are discussing the synthesis of nickel rich Ni/NiO nanocomposites by solution combustion method using nickel acetate as oxidizer and citric acid as fuel with fuel to oxidizer ratio 2:1. This chapter focuses on electric, photocatalytic and magnetic properties of as synthesized Ni rich Ni/NiO. A special attention is paid to understand the role of HNO_3 in determining the Ni or NiO content in the as synthesized material.

3.2. Experimental

3.2.1 Synthesis

Ni/NiO samples were synthesized by the solution combustion method. Nickel acetate (6 g) and citric acid (12 g) (fuel to oxidizer ratio 2:1) were dissolved in 20 ml of deionized water separately and mixed together. The volume of HNO_3 (15.44 M) added to the above solution mixture was optimized to 30 ml in order to get maximum quantity of Ni in the sample. The pH of the solution was maintained at 7 by adding ammonia solution to the above precursor solution. The resulting solution was heated on a hot plate about one hour to form gel like matter. On further heating, the gel undergoes combustion and gives ash-like powder sample (Ni-NiO-1). The synthesis was repeated by using above mentioned reactants with same experimental conditions, but 45 ml of HNO_3 were used instead of 30 ml of HNO_3 (Ni-NiO-2).

3.2.2 Characterization

The structural characterization of the samples were done with Rigaku X-ray diffractometer using Cu K_α radiation (λ =1.5414 Å). A Horiba JobinYvon Lab RAM HR system (resolution of the order of 3 cm^{-1}) equipped with He-Ne laser (632.8 nm) was used in order to measure the Raman spectra of the samples. Using KBr pellet method, Fourier Transform Infra Red spectroscopy (FTIR) of the samples was done using IRAffinity-1-8400S. A JEOL JEM 2100 Model High Resolution Transmission Electron Microscope (HRTEM) operated at 200 KeV attached with EDAX set up was used for the TEM measurements. The microstructure of the samples was examined by using JEOL JSM-6390 LV Model Scanning Electron Microscope (SEM). Carbon, hydrogen, nitrogen (CHN) analysis of the samples was performed using ElementarVario EL III C-H-N Analyser. UV-Vis absorption spectrum was measured using JASCO-V-570 UV-VIS-NIR spectrometer. X-ray photoelectron spectroscopy (XPS) of the samples was done by Kratos AXIS Ultra spectrometer. Keithley model 2400 source meter automated with Lab-VIEW software were used to measure the *d.c* electrical conductivity of the samples. The magnetic properties of the samples were measured with a Lakeshore make Model 7403 and 7410 Vibrating Sample Magnetometers (VSM).

3.2.3 Photodegradation studies

Photodegradation properties of Ni-NiO-1 and Ni-NiO-2 were done on Methylene Blue (MB) as model solution. 5 ml volume capacity borosil bottles were used for the experiment in which Ni-NiO-1 and Ni-NiO-2 were taken with 5 g/L as catalyst loading. Initially MB solution was prepared at 0.125 mM and poured in the bottles. Photocatalyst were added in these

bottles and placed under sunlight. Photodegradation of the sample was studied by taking absorbance of remaining MB solution using UV-VIS-NIR spectrometer after each one hour duration. The experiment is repeated for 0.05 and 0.025 mM of MB.

3.3. Results and discussion

Experiments for the synthesis of Ni/NiO nanocomposites are designed so as to get Ni rich Ni/NiO by keeping fuel to oxidizer ratio constant and changing the concentration of HNO_3 used for the combustion reaction. As described in the experimental section combustion reaction is carried out by taking 20, 30, 40, 45, 50, 60 ml of HNO_3 in each experiment. X- ray diffraction patterns of samples obtained as a results of these experiments are shown in Fig 3.1.One can see from the diffraction pattern, sample obtained with 30 ml of HNO_3 (Ni-NiO-1) gives relatively higher content of Ni in it when compared to other samples. Sample prepared with 45 ml of HNO_3 contain both Ni and prominent NiO peaks (N-NiO-2).

The XRD pattern of Ni-NiO-1 has distinct diffraction peaks at 2θ values 44.5^0 (111), 51.8^0 (200) and 76.5^0 (220) show a face centred cubic (fcc) structure very similar to standard data of nickel (JCPDS Card No 04-0850) with lattice parameter 3.523 Å (Fig. 3.1). The diffraction pattern of Ni-NiO-2 has peaks similar to that of Ni-NiO-1 with additional peaks at 37.4^0 (111), 43.5^0 (200), 62.9^0 (220) and 75.5^0 (311) which corresponds to the standard data of cubic NiO (JCPDS Card no 04-0835). Average grain size of Ni-NiO-1 was estimated using Scherrer's formula [Cullity; 1976] from the strongest peak of Ni ($2\theta = 44.5^0$) and is found to be 38 nm (table

3.1). For Ni-NiO-2 (45 ml HNO_3) average grain sizes of Ni and NiO are 40 and 36 nm respectively.

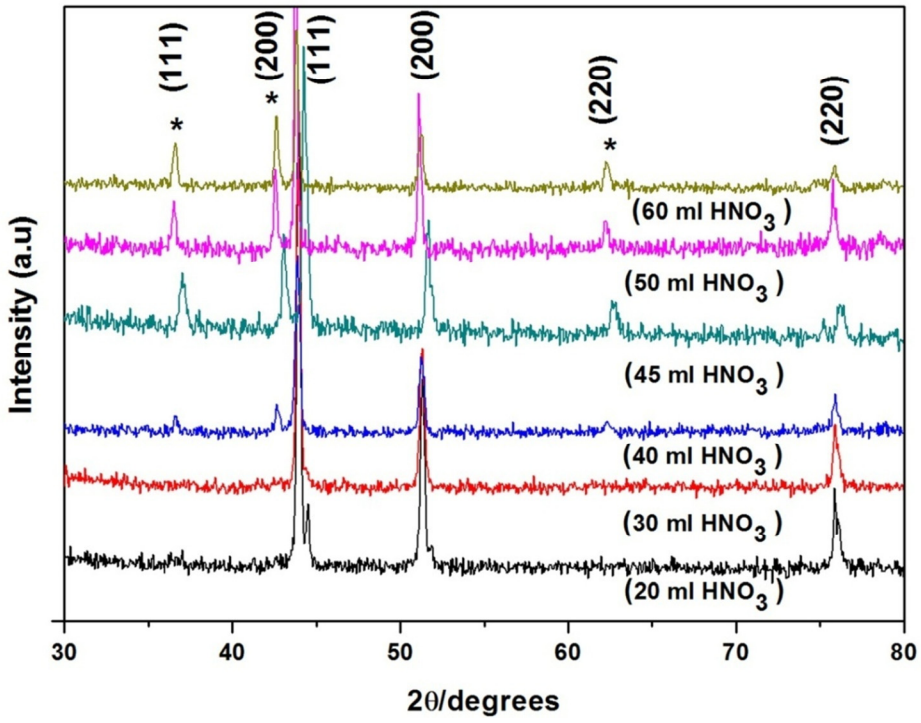

Fig. 3.1 *X-ray diffraction patterns of samples prepared with 20, 30, 40,45,50,60 ml of HNO_3 synthesized by solution combustion method ('*' indicates peaks of NiO).*

Table 3.1 *Grain size, weight percentage of Ni and NiO, and magnetic properties of Ni/NiO nanocomposites synthesized by solution combustion method using 30 ml HNO_3 (Ni-NiO-1) and 45 ml HNO_3 (Ni-NiO-2).*

Sample	Size (nm)		Wt. Percentage using XRD data		Wt. Percentage using Magnetic data		300 K M_s (emu/g)	300 K M_r (emu/g)	300 K H_c (Oe)	20 K M_s (emu/g)	20 K M_r (emu/g)	20 K H_c (Oe)
	Ni	NiO	Ni	NiO	Ni	NiO						
Ni-NiO-1	38	-	-	-	98	2	54	6	82	47	15	414
Ni-NiO-2	40	36	59	41	62	38	34	3	80	44	13	413

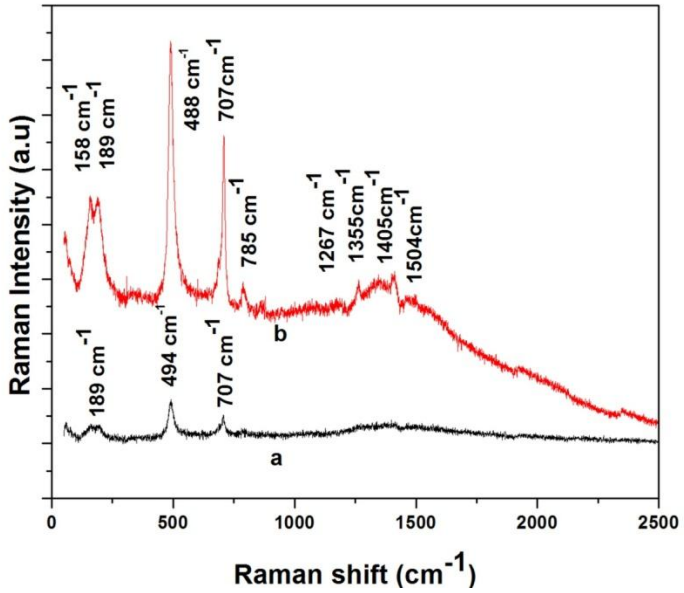

Fig. 3.2*.Raman spectra of Ni/NiO nanocomposites synthesized by solution combustion method using (a) 30 ml HNO_3 (Ni-NiO-1) (b) 45 ml HNO_3 (Ni-NiO-2).*

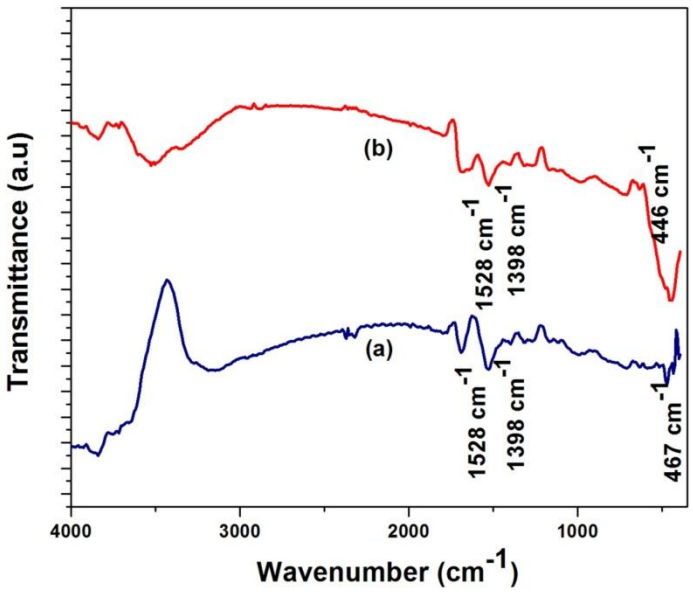

Fig. 3.3*. FTIR spectra of Ni/NiO nanocomposites synthesized by solution combustion method using (a) 30 ml HNO_3 (Ni-NiO-1) (b) 45 ml HNO_3 (Ni-NiO-2).*

Table 3.2 *Raman shift (cm^{-1}) of Ni/NiO nanocomposites synthesized by solution combustion method.*

N-NiO-1	N-NiO-2	Assignments
	158 ms	Lattice modes
189 vw	189 m s	Lattice modes
494 w	488 vs	1 LO - NiO
707 vw	707 s	2 TO- NiO
	1267 w	
	1355 w	D band
	1405w	
	1504 vw	G band

vw: very weak , w : weak , s : strong, vs : very strong, ms: medium strong

Figure 3.2 and 3.3 shows the Raman and FTIR spectra of Ni-NiO-1 and Ni-NiO-2 respectively synthesized by solution combustion method and details of the observed bands are given table 3.2. The D and G bands in the Raman and IR spectra of Ni-NiO-1 and Ni-NiO-2 grown with fuel to oxidizer ratio 2:1 are relatively weak. In the case of Ni-NiO-2 weak D band is seen around 1355 cm^{-1} followed by a very weak G band around 1504

cm^{-1}. Ni-NiO-1 does not give D and G bands in Raman spectra. The sample Ni-NiO-2 gives I_D/I_G ratio based on Raman spectra is around 1.28 and in the case of Ni-NiO-1, I_D/I_G ratio could not calculated. This observation indicates the presence of amorphous carbon in Ni-NiO-2. In the IR spectra of Ni-NiO-1 and Ni-NiO-2 the D band is seen around 1398 cm^{-1} and G band at 1528 cm^{-1}. Enhancement of low frequency Raman bands of Ni-NiO-2 compound is probably due to the collective oscillations of electrons of metallic nickel nanoparticles. Raman spectrum of NiO nanoparticles shows Raman bands at 518 cm^{-1} due to symmetric O-Ni-O vibrations of face centred cubic NiO (1LO mode vibration) [Alagiri *et al*; 2012]. In the case of Ni-NiO-1 and Ni-NiO-2 weak band is observed at 494 cm^{-1} and very strong band at 488 cm^{-1} respectively attributed to the O-Ni-O vibrations. The IR spectrum of Ni-NiO-1 and Ni-NiO-2 gives O-Ni-O vibrations at 467 cm^{-1} and 446 cm^{-1} respectively. A Raman band at 707 cm^{-1} (strong) in Ni-NiO-2 and weak one in Ni-NiO-1 is attributed to two phonon modes of transverse optical modes (2TO) of NiO [Wang *et al*; 2002]. Medium strong Raman bands at 158 and 189 cm^{-1} in Ni-NiO-2 and very weak band at 189 cm^{-1} in Ni-NiO-1 indicates the existence of lattice mode vibrations in the samples.

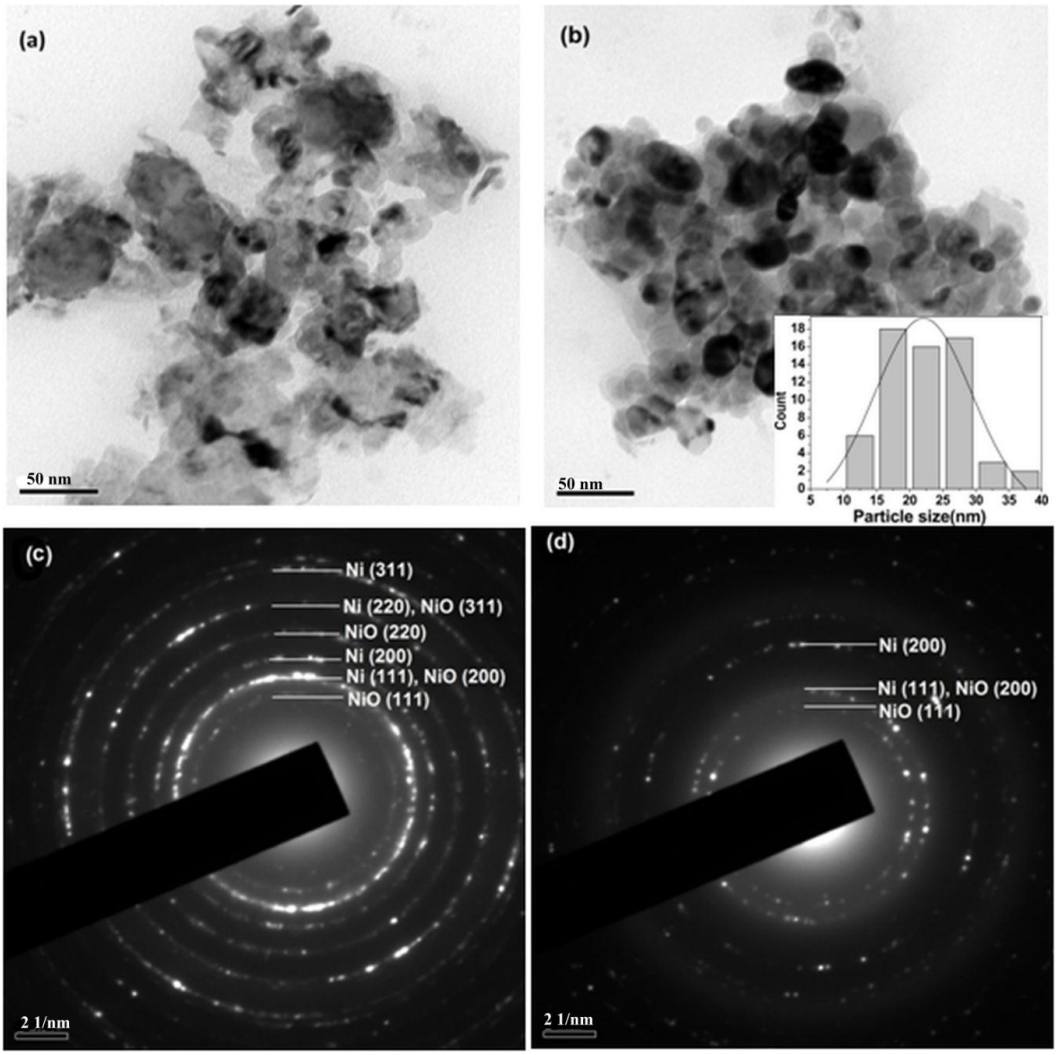

Fig. 3.4.*TEM images of Ni/NiO nanocomposites synthesized by solution combustion method using (a) 30 ml HNO_3 (Ni-NiO-1) (b) 45 ml HNO_3 (Ni-NiO-2) (c) and (d) are SAED patterns of Ni-NiO-1 and Ni-NiO-2 respectively.*

Figure 3.4 (a) and (b) show the transmission electron microscopy (TEM) images of Ni-NiO-1 and Ni-NiO-2. TEM image of Ni-NiO-1 shows agglomerate nature of nanoparticles, whereas relatively less agglomerate is found in Ni-NiO-2. The agglomeration of nanoparticles in these samples may be attributed to local sintering behavior that occurs due to the instantaneous high reaction temperature of solution during combustion process [Deraz; 2012]. The average particle size of nanoparticles of Ni-NiO-1 is 36 nm from the TEM image which is in consistent with the value calculated using the XRD data discussed previously. But nanoparticles of Ni-NiO-2 show inhomogeneous size distribution (Fig. 3.4b) and their particle sizes are in the range of 10-40 nm with an average size of 23 nm. The selected area electron diffraction (SAED) pattern of Ni-NiO-1 shows diffraction rings from the planes (111), (200), (220), (311) and they are comparable with standard data of fcc Ni (Fig. 3.4c). A few diffraction rings that corresponds to planes (111), (200), (220), (311) of cubic NiO (JCPDS Card File no 04-0835) is also seen in Ni-NiO-1 which suggest that the sample is a composite of Ni as well as NiO. However NiO is not detected significantly in XRD measurement, and the detection of it in SAED is probably due to higher sensitivity of electron diffraction. Diffraction rings of Ni-NiO-2 (Fig. 3.4d) shows presence of both Ni and NiO phase which is in consistent with XRD result of Ni-NiO-2. The SAED diffraction rings, second and fifth one seen from the centre in Ni-NiO-1 and second one from the centre in Ni-NiO-2 is match with both Ni and NiO phases. The unambiguous assignment of Ni and NiO is limited due to the small difference in their interplanar spacing (d) values.

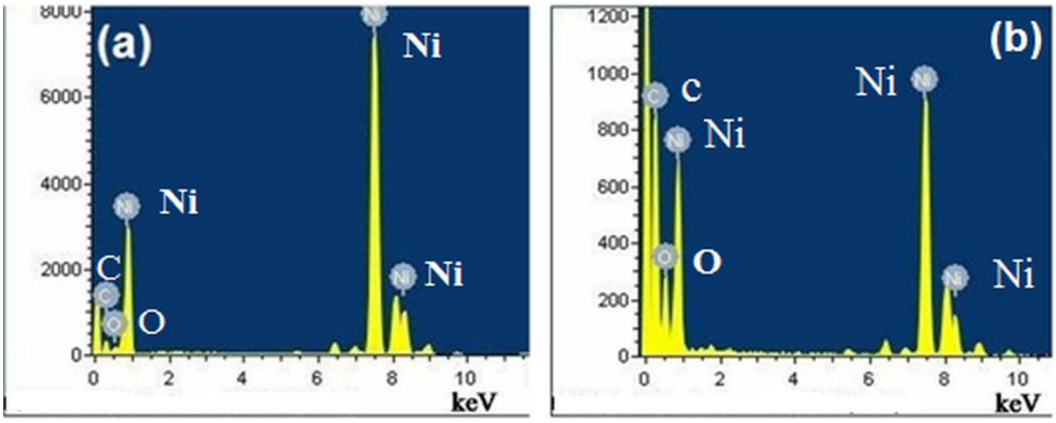

Fig. 3.5. *EDAX spectra of Ni/NiO nanocomposites synthesized by solution combustion method using (a) 30 ml HNO_3 (Ni-NiO-1) (b) 45 ml HNO_3 (Ni-NiO-2).*

Higher weight percentage of nickel is found in Ni-NiO-1 with traces of carbon and oxygen as one can see from the EDAX spectra (Fig. 3.5). However, the quantity of oxygen is more in Ni-NiO-2 indicating the formation of comparatively larger amount of NiO. These results are consistent with previously discussed XRD, SAED results. C-H-N analysis is also performed in order to know the carbon content in the samples and the carbon presence is found to be 0.07 % in Ni-NiO-1 and 7.12 % in Ni-NiO-2.

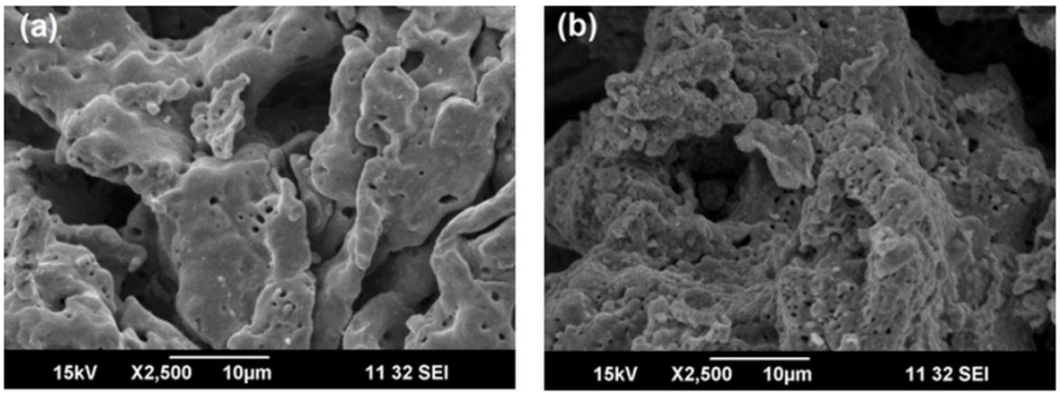

Fig. 3.6. *SEM images of Ni/NiO nanocomposites synthesized by solution combustion method using (a) 30 ml HNO_3 (Ni-NiO-1) (b) 45 ml HNO_3 (Ni-NiO-2).*

Figure 3.6(a) and (b) show the SEM images of Ni-NiO-1 and Ni-NiO-2, the porous nature of the samples contributed to the evolution of gases during the combustion process which is one of the peculiarities of SCS [Deraz; 2012, Kang *et al*; 2015, Manukyan *et al*; 2013]. It can be seen from the figure that the nature of the sample varies in terms of pore size as well as in number of pores. Pore size of Ni- NiO-1 is of the order of ~1 μm and that of Ni-NiO-2 about ~ 0.5 μm.

Chemical composition and microstructure of combustion products are mainly governed by the fuel to oxidizer ratio, amount of oxidizer, type of fuel and the acidity of precursor medium used in the combustion reaction [Deraz; 2012, Kang *et al*; 2015, Manukyan *et al*; 2013, Jung *et al*; 2005, Aruna *et al*; 2004,Peng *et al*; 2006]. In the present synthesis process, nickel acetate is used as oxidizer and citric acid as fuel. The neutralization of HNO_3 with NH_3 may give NH_4NO_3 which is also an oxidizer [Manukyan *et al*; 2014] in addition to nickel acetate. Aqueous solution of initial reactants are preheated to the boiling point of water results in viscous gel formation [Manukyan *et al*; 2014]. Initial gels are probably amorphous in nature which may have NiO/Ni phases as reported previously [Manukyan *et al*; 2013]. The formation of Ni may be attributed to reduction of NiO by NH_3 in the reaction system. The extent of reduction of NiO may decrease with increase in the quantity of HNO_3 and results in retention of comparatively higher percentage of NiO in N-NiO-2. On the other way, higher volume of HNO_3 may produce higher quantity of NH_4NO_3 which will decrease the fuel to oxidizer ratio which leads to the formation excess NiO component in Ni-NiO-2. The difference in the pore sizes of Ni-NiO-1 (1 μm) and Ni-

NiO-2 (0.5 μm) from the SEM image shows the dependence of pore size on fuel to oxidizer ratio [Manukyan *et al*; 2013] and comparatively less pore size observed in Ni-NiO-2 with respect to Ni-NiO-1 is due to low value of fuel to oxidizer ratio used for the synthesis of Ni-NiO-2.

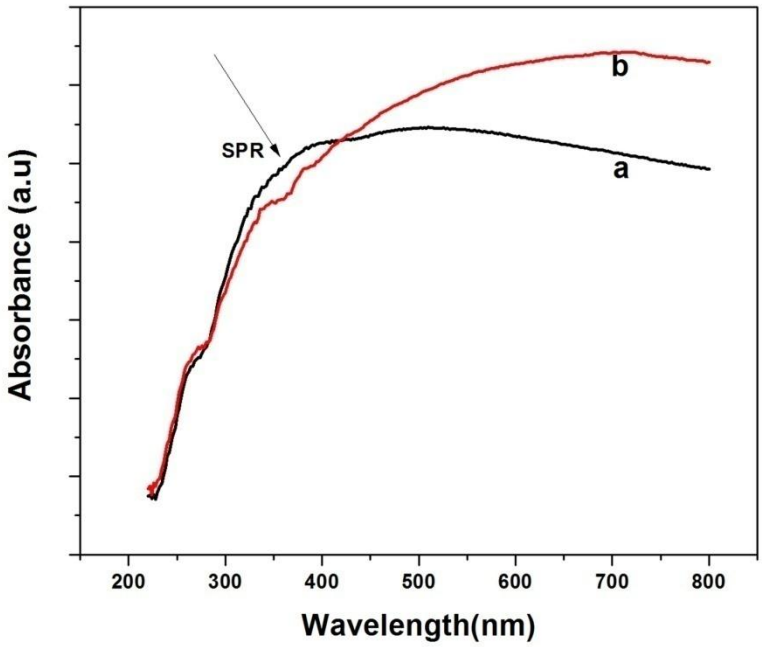

Fig. 3.7*.UV/Vis absorption spectra of Ni/NiO nanocomposites synthesized by solution combustion method (a) 30 ml HNO_3 (Ni-NiO-1) (b) 45 ml HNO_3 (Ni-NiO-2).*

The absorption spectrum of Ni-NiO-1 is broad which extends from 355 nm to 788 nm (Fig 3.7). But in the case of Ni-NiO-2 very feeble peaks are seen at 347 nm and 382 nm. Weak absorption band around 382 nm is probably attributed to surface plasmon resonance (SPR) as SPR band is previously reported in metallic Ni at 400 nm [Xiang *et al*; 2004].

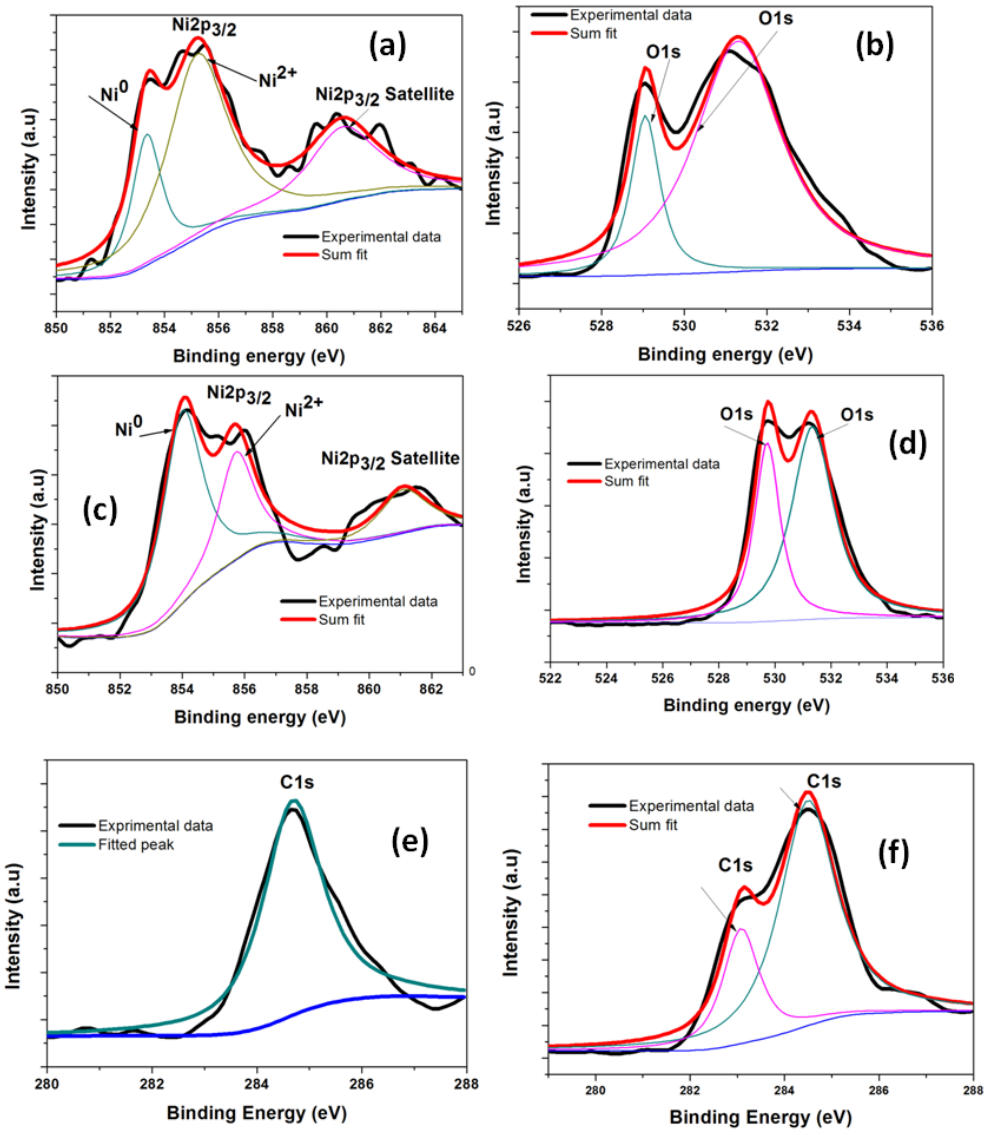

Fig. 3.8. *XPS spectrum of Ni/NiO nanocomposites synthesized by solution combustion method: (a) Ni 2p of Ni-NiO-1 (b) O 1s of Ni-NiO-1 (c) Ni 2p of Ni-NiO-2 (d) O 1s of Ni-NiO-2 (e) and (f) are C1s peaks of Ni-NiO-1 and Ni-NiO-2 respectively.*

Figure 3.8 shows the XPS spectra of Ni-NiO-1 and Ni-NiO-2 respectively. For Ni-NiO-1 $Ni2p_{3/2}$ contains two main peak and one satellite peak. The main peak observed at 855.25 eV corresponds to Ni^{2+} oxidation state whereas the peak observed at 853.35 eV is attributed to Ni^0. $Ni2p_{3/2}$satallite peak is found at 860.79 eV. In the case of Ni-NiO-2, Ni^{2+} and Ni^0 are observed at 855.76 and 854.07 eV respectively. Its satellite peak is observed at 861.17eV. O1s peak contain two peaks at 529.71 and 531.32 eV for Ni-NiO-1. For Ni-NiO-2, these peaks are found at 529.71 and 531.38 eV which confirms the formation of NiO. Presence of the carbon in both the sample is evidenced by the observations of C1s peaks in the samples. In the case of Ni-NiO-1 C1s peaks are found at 284.72 eV, for Ni-NiO-2 there are two peaks of C1s observed at 284.78 and 283.09 eV respectively. Atomic concentration of Ni, O, C in Ni-NiO-1 is 16.02, 38.79 and 45.20 % respectively where as these values for Ni-NiO-2 are 12.62, 35.01, and 52.37 %. The above observation shows that carbon percentage in Ni-NiO-2 is more than Ni-NiO-1 which is in conformity with CHN analysis done on these samples.

3.3.1 Electrical properties

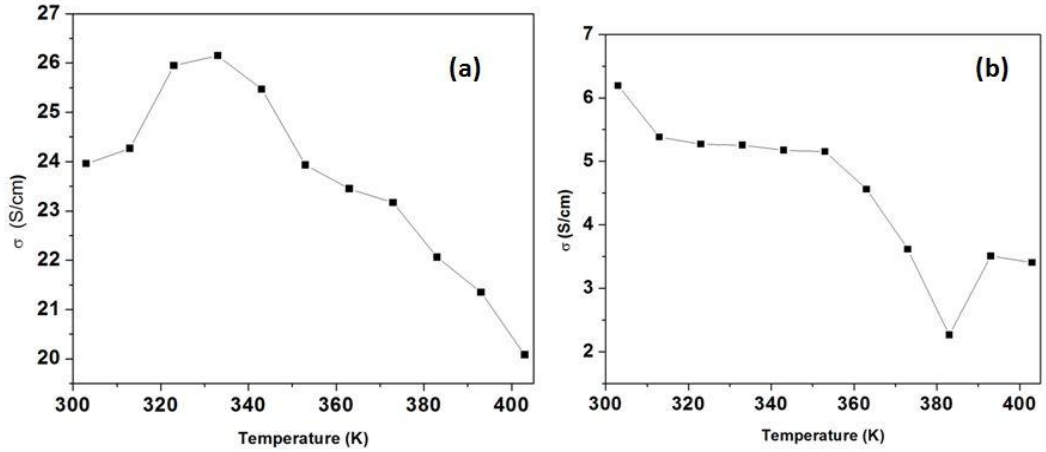

Fig. 3.9*.d.c conductivity plots of Ni/NiO nanocomposites synthesized by solution combustion method (a) 30 ml HNO_3 (Ni-NiO-1) (b) 45 ml HNO_3 (Ni-NiO-2).*

From the Fig. 3.9 one can see that the conductivity increases with the temperature up to 333 K and thereafter it decreases with respect to temperature in Ni-NiO-1. But in the case of Ni-NiO-2, conductivity decreases initially up to 383 K and thereafter it increases with respect to increase of temperature. Among the samples, Ni-NiO-1 is having more amount of nickel with higher order conductivity. In the case of Ni-NiO-1, number of electrons available for conduction is more and percolation takes place forming a conducting path in the sample. This may be the reason for the higher order conductivity observed in Ni-NiO-1.

3.3.2 Photocatalytic properties

Table 3.3 *Results of photodegradation efficiencies of Ni/NiO nanocomposites synthesized by solution combustion method*

Molarity (mM)	**Photodegradation efficiency in %**	
	Ni-NiO-1	Ni-NiO-2
0.125	58	55
0.05	95	92
0.025	99	96

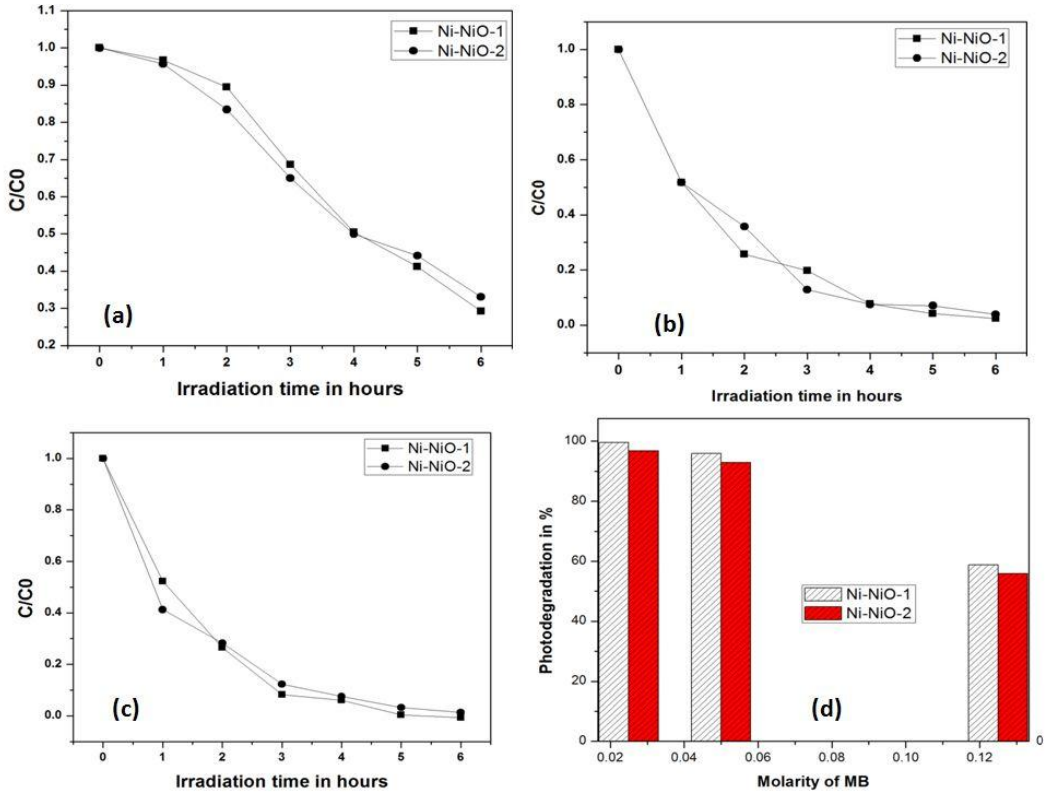

Fig. 3.10*.Photodegradation characteristics of Ni-NiO-1 and Ni-NiO-2 nanocomposites synthesized by solution combustion method at different molarities of MB solution under sun light exposure (a) 0.125 mM (b) 0.05 mM (c) 0.025 mM (d) Histogram showing photodegradation efficiency of Ni-NiO-1 and Ni-NiO-2 at 0.125, 0.05, 0.025 mM of MB.*

Figure 3.10 shows the results of photodegradation studies of Ni-NiO-1, Ni-NiO-2 under molar conditions of MB 0.125 mM, 0.05 mM and 0.025 mM respectively on exposure to sun light. Photodegradation efficiency of samples are calculated using the equation $(1-C_t/C_0)$ x100 % [Hayat *et al*; 2011] and the obtained results are shown in table 3.3. Ni rich sample Ni-NiO-1 shows better photo degradation efficiency when compared to relatively less nickel content sample Ni-NiO-2 (table 3.3). It is observed that decrease of molarity of MB increases photodegradation

efficiency of samples. Also increase of NiO content in the sample Ni-NiO-2 decreases the photodegradation efficiency. The photodegradation efficiency of Ni-NiO-1 and Ni-NiO-2 are 58 % and 55% respectively with 0.125 mM of MB. The photodegradation efficiency increases to 99 % for Ni-NiO-1, 96 % for Ni-NiO-2 when the molarity is decreased to 0.025 mM of MB. But dye removal from contaminated water with semiconductors like NiO, TiO_2, ZnO, SnO_2 etc. is mainly by photodegradation process which is usually accompanied by non radiative transition of electrons excited from the valance band to conduction band [Hayat *et al*; 2011,Gondal *et al*; 2007, Samadi *et al*; 2016, Shajira *et al*; 2015]. Semiconductor like TiO_2/PANI composite polymers exhibit better photocatalytic activities for the degradation of methelyne blue [Reddy *et al*; 2016]. The fact of comparatively larger nickel presence in Ni-NiO-1 is shown in our XRD. Photodegradation property of metallic nanoparticles like gold and silver are assisted by surface plasmon resonance (SPR) of metallic nanoparticles [Zhu *et al*; 2009, Chen *et al*; 2010]. Transition metal nickel shows a broad and weak peak around 381 nm in the absorption spectrum which is probably attributed to SPR as stated previously (Fig.3.7). Nickel present in Ni-NiO-1 may have been subjected to rapid heating while absorbing photons from incident radiation, which might generate electrons. These electrons combine with O_2 that are adsorbed on the photocatalyst, leading to the formation of O_2^- species. Radicals like $OH^\cdot$ or $HO_2^\cdot$ will be produced as a result of reaction between O_2^- and H^+ ions [Zhu *et al*; 2009]. Finally, the reaction of $OH^\cdot$ radical with that of dye molecules will lead to the degradation of the dye molecules. NiO is a wide band gap semiconductor and it may also involve in photodegradation process of dyes. As there is nickel in the

samples, SPR may be one of the major contributor for the degradation of the dye. In the present case, photodegradation process of dye (MB) is contributed by the combined effect of SPR and $OH^{\cdot}$ radicals generated by the semiconducting NiO.

3.3.3 Magnetic properties

3.3.3.1 Field dependent magnetization (M-H)

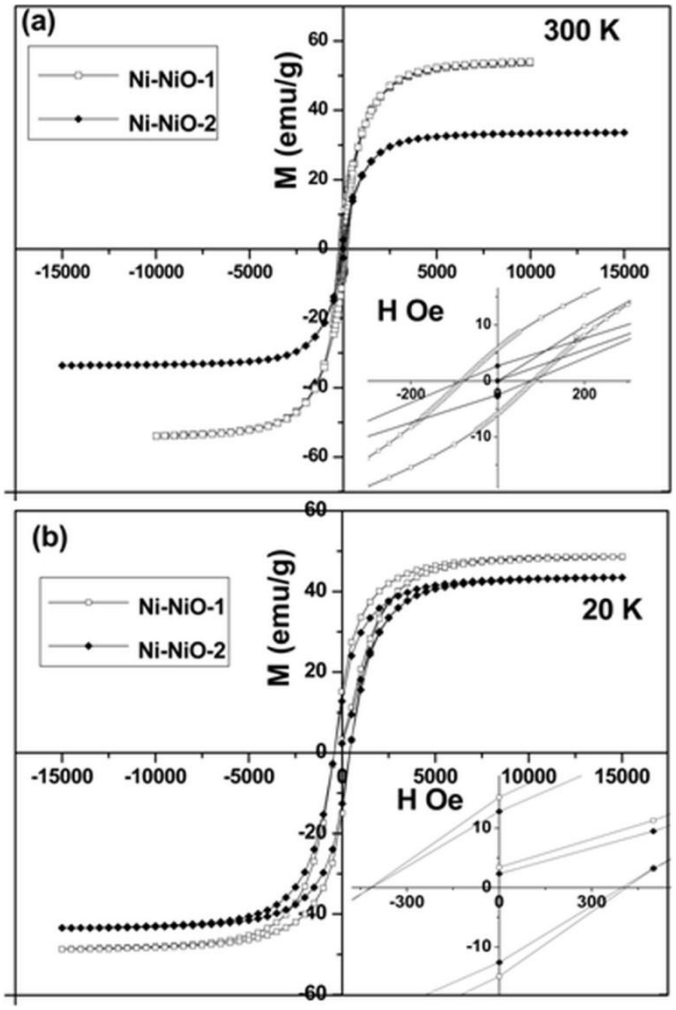

Fig. 3.11.*Hysteresis curves (M-H) of Ni/NiO nanocomposites synthesized by solution combustion method using 30 ml HNO_3 (Ni-NiO-1) and 45 ml HNO_3 (Ni-NiO-2) at (a) 300 K (b) 20 K. Inset shows the enlarged portion of the central region of M-H curve.*

The hysteresis curves of Ni-NiO-1 and Ni-NiO-2 at temperatures of 300 and 20 K are shown in Fig. 3.11, the details of obtained saturation magnetizations (M_s), coercivities (H_c), remanant magnetizations (M_r) are given in table 3.1. The M_s, M_r, H_c values of Ni-NiO-1 at 300 K are 54, 6 emu/g, 82 Oe respectively and are comparable to the corresponding values of bulk nickel reported in the literature [Hwang *et al*; 1997]. For Ni-NiO-2, M_s and M_r values are less than that of Ni-NiO-1 and almost same H_c values are obtained for both Ni-NiO-1and Ni-NiO-2. The weight percentages of Ni and NiO are calculated from magnetic data (M_s at 300 K) using the equation $\frac{N_{Ni}}{N_{Ni}+N_{NiO}} = \frac{M_{s,measured}}{M_{s,bulk}}$ where N_{Ni} is average number of unoxidized Ni atoms and N_{NiO} is average number of Ni atoms in NiO [Yao *et al*; 2014]. The calculations using above formula shows that NiO weight percentage in Ni-NiO-1 is negligibly small compared to Ni (table 3.1). In Ni-NiO-2, NiO weight percentage is increased to ~ 40 in comparison with Ni-NiO-1. Weight percentages of Ni and NiO in the samples can also be calculated using reference intensity ratio (RIR) method [Hubbard *et al*; 1988] from the XRD data and the values so obtained are given in table 3.1. NiO is antiferromagnetic and the increase of NiO content in the sample may decrease the value of M_s in Ni-NiO-2. An exchange field (H_E) of the order of 7 Oe at 20 K is found in Ni-NiO-2 which indicates that there exists a low exchange coupling between FM Ni atoms and AFM NiO in the composite. Exchange bias is not observed in Ni-NiO-1 due to negligible presence of NiO. The value of H_E, hence H_c in FM/AFM system depends on factors such as anisotropy of AFM material and its thickness [Lund *et al*; 2002, Nogues *et al*; 1999]. Since NiO is found to be material with low anisotropy

[Schron *et al*; 2012, Nogues *et al*; 2005] it would require large NiO thickness to observe the loop shift. Also in a system, composing of Ni and NiO weight percentage of Ni should be very small compared to NiO for the effective interaction between Ni and NiO [Yao *et al*; 2014]. Combustion method using organic precursors can supply carbon as additive/support element in the prepared samples [Jayalakshmi *et al*; 2008]. Presence of this unintentionally incorporated non magnetic carbon (amorphous form) in the system could act as layer and can suppress exchange coupling between FM and AFM particles. In turn, this would reduce the effective NiO thickness due to suppressed connectivity effects leading to low H_E and H_c [Nogues *et al*; 2006, Margaris *et al*; 2012]. The presence of carbon in both the samples is identified with EDAX, CHN, and XPS analysis discussed previously. Interestingly, H_c values in both samples are same, indicates that presence of carbon in the samples which isolates FM moments of Ni atoms leads to increase of H_c at low temperature. The value of H_c obtained for the samples is ~413 Oe at 20 K and are enhanced, compared to similar reports in Ni/NiO nanoparticles [Yuan ; 2010, Ahmadvand *et al*; 2010].

3.3.4.2 Temperature dependent magnetization (M-T)

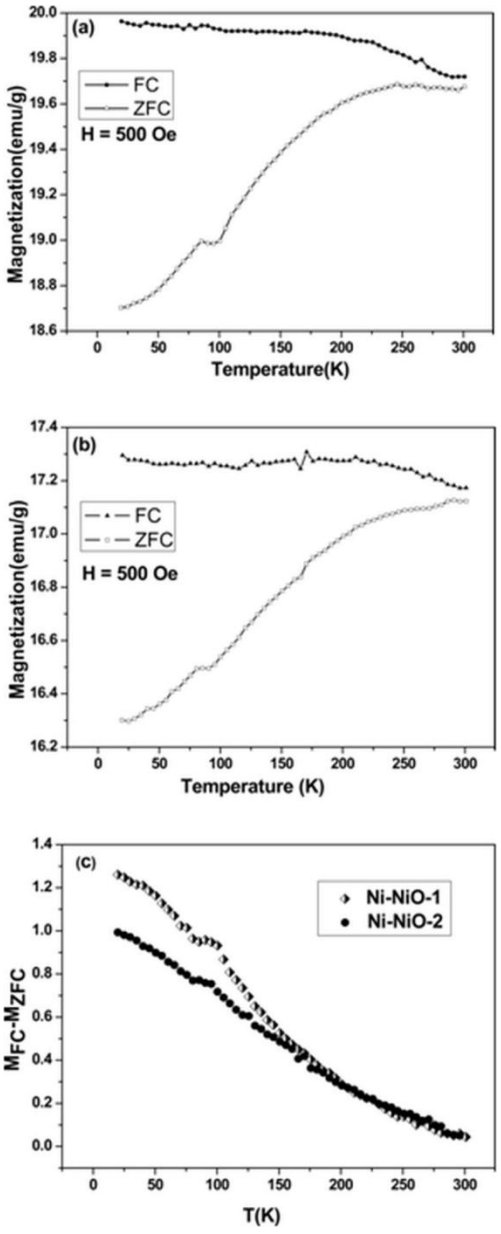

Fig. 3.12. *FC and ZFC curves (at an applied field of 500 Oe) of Ni/NiO nanocomposites synthesized by solution combustion method using (a) 30 ml HNO_3 (Ni-NiO-1) (b) 45 ml HNO_3 (Ni-NiO-2) (c) Plot of Magnetic irreversibility ($M_{irr} = M_{FC} - M_{ZFC}$) with temperature for Ni-NiO-1 and Ni-NiO-2.*

In the Fig. 3.12 (a) & (b) shows the field cooling (FC) and zero field cooling (ZFC) plots of samples Ni-NiO-1 and Ni-NiO-2 respectively. Although the shape and nature of both the plots looks similar they differ in FC and ZFC magnetization and hence in magnetic irreversibility (M_{irr}= M_{FC}-M_{ZFC}). At 20 K, FC magnetization and ZFC magnetization of Ni-NiO-1 are about ~ 20 and 18.7 emu/g whereas for Ni-NiO-2 these magnetization values are ~17.3, 16.3 emu/g respectively. Lower FC and ZFC magnetization of Ni-NiO-2 when compared to Ni-NiO-1 can be attributed to the presence of larger weight percentage of NiO in Ni-NiO-2. It has been reported that coexistence of ferromagnetic and antiferromagnetic phases leads to spin glass behaviour in NiO system [Tiwari *et al*; 2005] and can decrease the magnetization at low temperature in Ni/NiO system. Magnetically irreversible nature of samples can be well understood if one draws the plot between magnetic irreversibility M_{irr} with temperature (Fig. 3.10c). It is evident from the figure that M_{irr} for Ni-NiO-1(1.3 emu/g) is higher than Ni-NiO-2 (1.0 emu/g).

Bifurcation between FC- ZFC and the maxima in the ZFC plot could not be observed in the magnetic measurement, for a range of temperature from 20 to 300 K indicates that irreversibility temperature (T_{irr}) of both the samples is close to room temperature. From the M -T curve of the Ni-NiO-1 and Ni-NiO-2 one can see higher T_B which is around 300 K. This could arise probably due to the larger average size of the Ni particles and increased anisotropy due to the FM-AFM coupling in Ni/NiO system [Skumryev *et al*; 2003]. Using the grain size given in the Table 3.1 a rough estimate of blocking temperature (T_B) of both samples are calculated with the equation $T_B = k\ V/\ 25k_B$ [Morrish; 1965] (k is anisotropy constant of

bulk Ni), it is found to be ~ 416 K. The difference in the calculated and observed values may be due to factors such as reduced anisotropy, broad particle size distribution and dipolar effects seen in the nanoparticles [Knobel *et al*; 2008].

3.4. Conclusions

The amount of NiO in Ni/NiO nanocomposites synthesized using solution combustion method can be controlled by varying the volume of HNO_3 precursor used in the reaction. Raman data shows the presence of amorphous carbon in the samples. XPS analysis shows that nickel exits in both Ni^0 and Ni^{2+} oxidation states. *d.c* electrical conductivity of the Ni rich Ni/NiO nanocomposites, decreases with respect to temperature suggesting the metallic behavior of the nanocomposites. Photocatalytic efficiency of the samples increase with respect to nickel content present in the sample. Photodegradation process of methylene blue in the presence of sun light is assisted by the surface plasmon resonance of Ni in Ni-NiO composite system. Saturation magnetization (M_s) of Ni rich Ni/NiO decreases with increase in the volume of HNO_3 used for its synthesis, due to the presence of higher content of antiferromagnetic NiO in Ni/NiO samples. Unintentionally incorporated carbon might have reduced the exchange interactions between Ni and NiO and reduced the magnitude of EB and H_c. Ni/NiO nanocomposites having magnetic coercivity of H_c~ 413 Oe could find use in magnetic recording devices.

.....ൠ.....

Chapter-4

Contents

Photocatalytic and ferromagnetic properties of electrically conducting multifunctional NiO rich Ni/NiO nanocomposites in amorphous carbon matrix

4.1. Introduction

Ni/NiO nanocomposites system is subject of research recently because of its variety of applications in the field of catalysis, magnetic recording devices, dye absorption, lithium storage, bioseparations etc. [Yuan *et al*; 2013, Skumryev *et al*; 2003, Liu *et al*; 2007, Wen *et al*; 2011, Lee *et al*; 2006]. Ni is ferromagnetic (FM) and NiO is antiferromagnetic (AFM), the interaction between FM-AFM would give rise to exchange bias (H_E) [Yuan; 2010, Sharma *et al*; 2010, Nogues *et al*; 2008]. There has been great demand for the photocatalytic materials, which can degrade the toxic organic wastes as well as textile dyes. The drawback in the usage of photocatalysts was that, it could not be easily removed after the photocatalytic reaction. On the other hand magnetic composites based photo catalysts can be magnetically separated after its use [Nguyen *et al*; 2015, Behrad *et al*; 2015, Dewi *et al*; 2016]. However, some of the presently available magnetic nanoparticles are prone to oxidation and hence, its magnetic property may get reduced after repeated use. A protective matrix, layer or coating may be best suited to protect these materials from the surrounding environment. It is reported that, polymer

like polyaniline can be used as protective covering for iron based nanoparticles which shows modified physical properties with respect to pristine polymers [Reddy *et al*; 2007, Reddy *et al*; 2008]. Carbon is one of the best non-toxic materials which can be used as a protective and supporting system for nanocrystalline multifunctional materials. Metal or metal oxide composites with carbonaceous or polymeric material may have applications such as catalyst, sensors, nanoelectronics, photocatalyst, electric and electrode materials [Reddy *et al*; 2008, Reddy *et al*; 2014, Reddy *et al*; 2015, Zhang *et al*; 2007, Cakici *et al*; 2017]. NiO based materials have been previously studied as a typical photocatalysts for the degradation of organic dyes/molecules [Wan *et al*; 2013, Kianfar *et al*; 2016, Harraz *et al*; 2010, Motahari *et al*; 2014]. Interestingly, the combination of metal and semiconductor can vary the photo catalytic properties of materials by modifying the surface properties of the semiconductor [Pozio *et al*; 2016].

Ni/NiO nanocomposites is an ideal, compatible metal and semiconductor combination system, and it can be synthesized by pulsed laser deposition, reactive ball milling of NiO, partial mechanochemical reduction of NiO, thermal decomposition of nickel acetate and solution combustion synthesis [Yuan ; 2010, Doppiu *et al*; 2004, Nogues *et al*; 2008, Kremenovic *et al*; 2012, Deraz ; 2012] etc. Among these methods, solution combustion synthesis (SCS) is a simple, fast and versatile method, for the synthesis of Ni/NiO [Deraz; 2012, Kang *et al*; 2015, Jung *et al*; 2005]. In our previous chapter, we have presented the synthesis of nickel rich Ni/NiO using SCS and their detailed electric, photocatalytic and magnetic properties. The present chapter focuses on the synthesis of NiO

rich Ni/NiO composite system, by changing the fuel to oxidizer ratio used for the synthesis, keeping the volume of HNO_3 as fixed. Electric, photocatalytic and magnetic properties of Ni/NiO nanocomposites is also investigated.

4.2. Experimental

4.2.1 Synthesis

All the chemicals used for the synthesis were of AR grade (SpectrochemPvt Ltd. Mumbai, India). Ni/NiO nanocomposites used in the present investigation were synthesized by the solution combustion method (Chapter 3). 4 gm of nickel acetate (fuel) and citric acid (oxidizer) were dissolved in 20 ml of deionized water separately and mixed together (fuel to oxidizer ratio 1:1). In the above solution mixture, 30 ml HNO_3 (15.44 M) was added and the pH of the solution was adjusted to 7 by adding ammonia solution. The precursor solution was heated on a hot plate (one hour) to get the experimental sample (Ni-NiO-3). Synthesis of Ni-NiO-4 was done with the above mentioned reactants with the same procedure by keeping the fuel to oxidizer ratio as 1:2 (2 gm citric acid and 4 gm nickel acetate). Analytical characterization of the materials was done using the equipments described in the experimental section of chapter 3.

4.2.2 Photodegradation studies

Photodegradation properties of the samples were investigated by taking Methylene Blue (MB) as the model solution under direct sunlight exposure. 0.125 mM MB solution was prepared initially, which was poured into 5 ml borosil bottles with 5 g/L catalyst loading. After each one hour of exposure to solar radiation, optical absorption measurements of remnant

MB solution were performed with UV-VIS-NIR spectrometer (JASCO-V-570). The experiment was repeated for 0.05 mM and 0.025 mM of MB with the above described protocol.

4.3. Results and Discussion

4.3.1. X-ray diffraction analysis

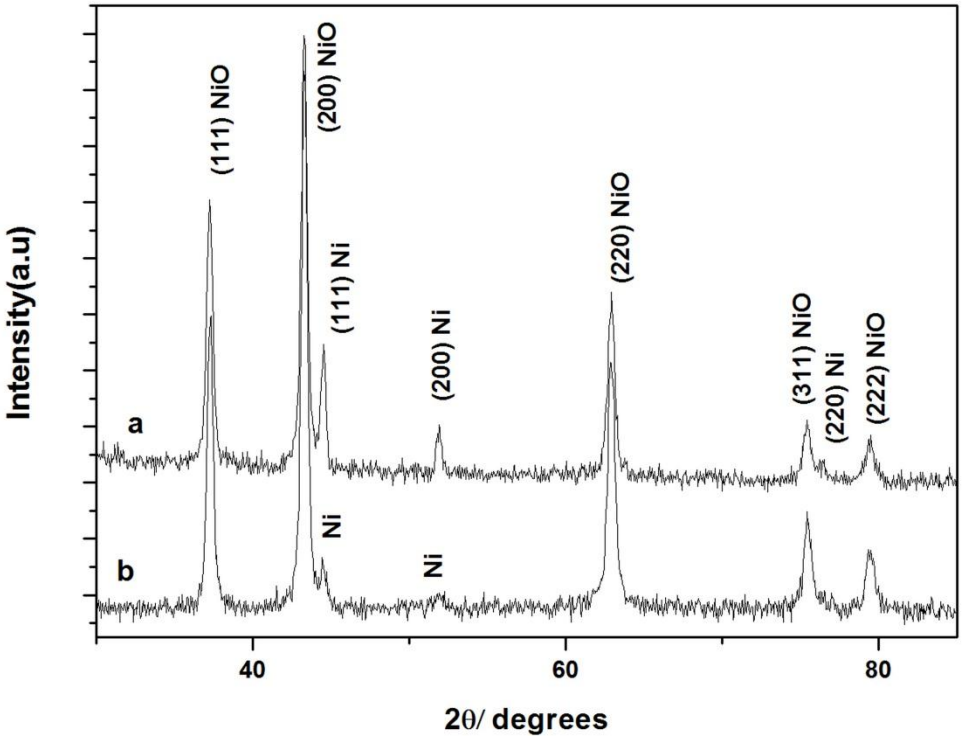

Fig. 4.1. *X-ray diffraction patterns of Ni/NiO nanocomposites synthesized by solution combustion method using (a) 30 ml HNO_3 with fuel to oxidizer ratio of 1:1(Ni-NiO-3) (b) 30 ml HNO_3 with fuel to oxidizer ratio of 1:2 (Ni-NiO-4).*

XRD pattern of Ni-NiO-3 has diffraction peaks at 2θ values of 37.23 (111), 43.30 (200), 44.50 (111), 51.93 (200), 62.97 (220), 75.44 (311), 76.33 (220) and 79.56 (222) (Fig.4.1). Among these, diffraction peaks at 2θ, 37.23, 43.30, 62.97 and 75.44 are corresponding to that of cubic phase of NiO (JCPDS card No. 04-0835). The diffraction peaks at 44.50 (111), 51.93 (200) and 76.33 (220) are related to face centered cubic Ni (JCPDS card No. 04-0850). XRD pattern of Ni-NiO-4 shows diffraction peaks at 2θ values of 37.2 (111), 43.3 (200), 44.50 (111), 51.93 (200), 62.97 (220), 75.60 (311) and 79.51(222). Among these 37.2 (111), 43.3 (200), 62.97 (220), 75.60 (311) and 79.51(222) match with cubic NiO (JCPDS card No. 04-0835). The weak diffraction peaks in Ni-NiO-4 at 2θ values 44.50 (111), 51.93 (200) matches with metallic Nickel phase (JCPDS card No. 04-0850). This indicates that both the samples are Ni/NiO nanocomposites with difference in Ni:NiO ratio. Average grain size of Ni and NiO in Ni-NiO-3 is obtained based on strongest peaks at 44.50 and 43.30 with Scherrer's formula [Cullity; 1976] which gives a value of ~36 nm. Average grain size of NiO in Ni-NiO-4 is about ~21 nm and for Ni phase is ~44 nm. Ni/NiO nanocomposites synthesized with 30 ml HNO_3 (Ni-NiO-1) and 45 ml HNO_3 (Ni-NiO-2) both having fuel to oxidizer ratio of 2:1 gives Ni rich composition as discussed in the previous chapter.

4.3.2. Raman and Fourier transform infrared spectral analysis

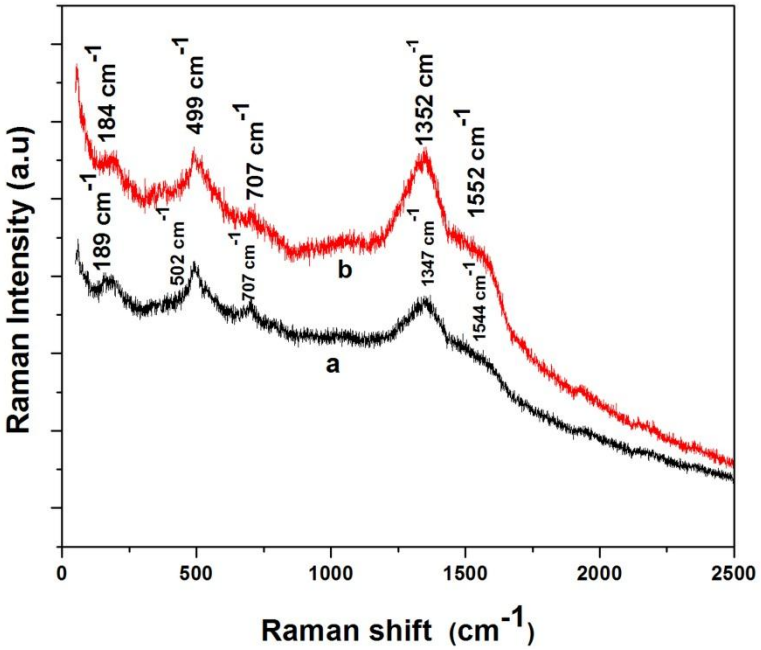

Fig. 4.2. *Raman spectra of Ni/NiO nanocomposites synthesized by solution combustion method using (a) 30 ml HNO_3 with fuel to oxidizer ratio of 1:1(Ni-NiO-3) (b) 30 ml HNO_3 with fuel to oxidizer ratio of 1:2 (Ni-NiO-4).*

Table 4.1 Raman *shift (cm^{-1}) of Ni/NiO nanocomposites synthesized by solution combustion method with different fuel to oxidizer ratios.*

Ni-NiO-3	Ni-NiO-4	Assignments
189 vw	184 vw	Lattice modes
502w	499 w	1 LO - NiO
707 vw	707 vw	2 TO- NiO
1347 s	1352 s	D band
1544 sh	1552 sh	G band

vw: very weak , w : weak , s :strong, , sh : shoulder

Raman shift of the Ni/NiO nanocomposites compounds under investigation are shown in table 4.1. Strong and broad Raman band centred around 1347 cm^{-1} is observed in Ni-NiO-3 and 1352 cm^{-1} in Ni-NiO-4 (Fig.4.2). This band is related to D band of amorphous carbon, since no crystalline carbonaceous phase, like graphene and graphite is detected in the XRD. Raman band seen adjacent to D band around 1552 cm^{-1} as a shoulder in Ni-NiO-4 and 1544 cm^{-1} in Ni-NiO-3 corresponds to G band (Fig.4.2). Intensity of D band is relatively higher than that of G band in Ni-NiO-3 and Ni-NiO-4, which is similar to that of sp^2 bonded carbon reported previously [Cao *et al*; 2015, Yan *et al*; 2010]. The intensity ratio (I_D/I_G) from the Raman spectra is a measure of crystallinity of carbon, it is found to be 1.32 in Ni-NiO-3 and 1.26 in Ni-NiO-4. I_D/I_G ratio is more than 1 in Ni-NiO-3, Ni-NiO-4 which indicates the existence of amorphous carbon matrix. IR spectra of Ni-NiO-4 give D band at 1383 and G band at 1534 cm^{-1} (Fig.4.3). But in the IR spectra of Ni-NiO-3, the intensity of D band is relatively weak with respect to G band, which are seen around 1398 and 1580 cm^{-1} respectively.

Raman spectrum of NiO nanoparticles gives strong Raman bands at 518 cm^{-1} [Alagiri *et al*; 2012]. In the present case strong Raman bands are seen at 499 and 502 cm^{-1} in the samples attributed to symmetric O-Ni-O vibrations of octahedral NiO_6 group, as in face centred cubic NiO (1LO mode vibration). IR bands are absent in this region which clearly indicates that the origin of these bands are due to the symmetric stretching vibrations O-Ni-O as reported previously [Farhadi *et al*; 2011]. A weak Raman band is seen at 707 cm^{-1} in the samples which is attributed to two phonon modes of transverse optical modes (2TO) of NiO[Wang *et al*; 2002]. Moderately

intense Raman band seen at 184 and 189 cm^{-1} in the samples is contributed to lattice vibrations of NiO. C-H-N analysis of Ni-NiO-3 and Ni-NiO-4 shows 0.75% carbon which indicates that Ni/NiO nanocomposites are in carbon matrix.

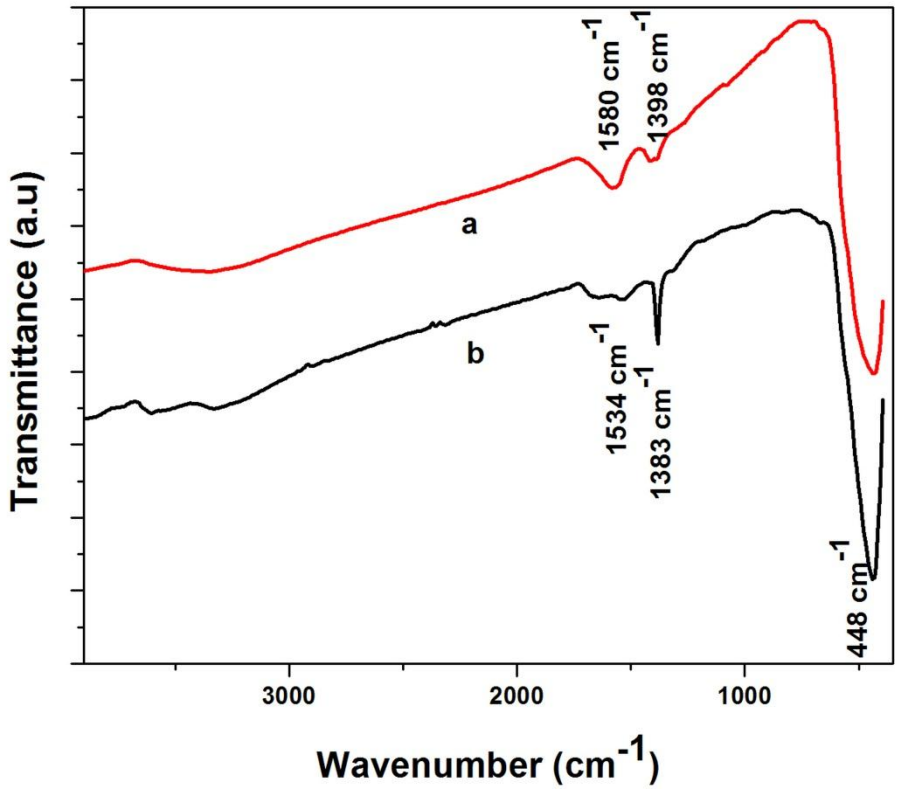

Fig. 4.3. *FTIR spectra of Ni/NiO nanocomposites synthesized by solution combustion method using (a) 30 ml HNO_3 with fuel to oxidizer ratio of 1:1 (Ni-NiO-3) (b) 30 ml HNO_3 with fuel to oxidizer ratio of 1:2 (Ni-NiO-4).*

4.3.3. Scanning electron microscopy analysis

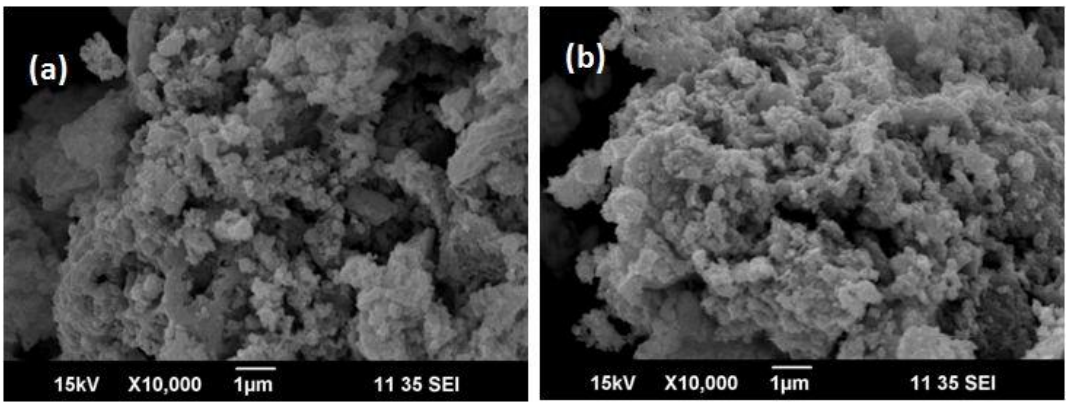

Fig.4.4. *SEM images of Ni/NiO samples synthesized by solution combustion method using (a) 30 ml HNO_3 with fuel to oxidizer ratio of 1:1 (Ni-NiO-3) (b) 30 ml HNO_3 with fuel to oxidizer ratio of 1:2 (Ni-NiO-4).*

Agglomerated nanoparticles without much spacing between individual nanoparticles are seen in both Ni-NiO-3 and Ni-NiO-4 from the SEM images (Fig.4.4). The amount of space between individual nanoparticles is more in Ni-NiO-1 with respect to Ni-NiO-2 as discussed in the previous chapter. This may be due to slightly higher value of fuel to oxidizer ratio (2:1) used for the synthesis of Ni-NiO-1. The observed agglomeration of Ni-NiO-3 and Ni-NiO-4 can probably attributed to the smaller fuel to oxidizer ratio used for the synthesis of these samples compared to Ni-NiO-1 and Ni-NiO-2. HNO_3 (30 ml) is used for the synthesis for NiO rich Ni/NiO with different fuel to oxidizer ratio hence the amount of intermediate compound NH_4NO_3 may be the same in both cases. Fuel to oxidizer ratio may be one of the parameters which determine the formation of NiO rich Ni/NiO. If the fuel to oxidizer ratio (1:2) is less as in the case of Ni-NiO-4, there will be more probability of oxidation than reduction and gives NiO rich Ni/NiO nanocomposites.

4.3.4. Absorption analysis

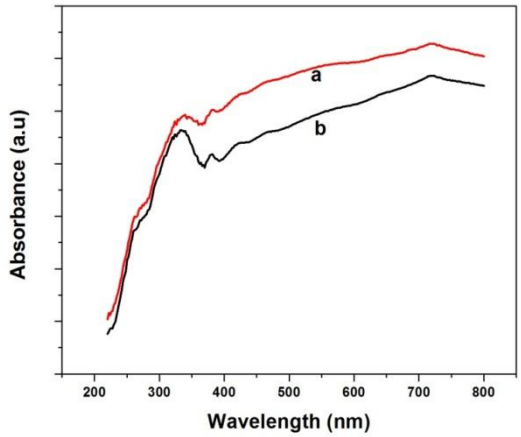

Fig. 4.5*.UV/Vis absorption spectra of Ni/NiO nanocomposites synthesized by solution combustion method with different fuel to oxidizer ratio.*

In Ni-NiO-3, weak peaks are observed at 336 nm and 380 nm in the optical absorption spectra. For Ni-NiO-4 also weak absorption peaks are present at 339 nm and 381 nm (Fig.4.5). Weak absorption band around 381 nm is probably due to surface plasmon resonance (SPR) since SPR band is previously reported in metallic Ni at 400 nm [Xiang *et al*; 2004].

In the XPS spectra Ni $2p_{3/2}$ peak is observed at 853.6 eV which corresponds to Ni^0 (metallic nickel) and 855.42 eV to Ni^{2+} in Ni-NiO-3 (Fig 4.6(a)). In Ni-NiO-4, Ni $2p_{3/2}$ peak is found at 853.64 eV (Ni^0) and Ni^{2+} oxidation state is found at 855.45 eV (Fig 4.6(c)). The O 1s peak is observed at 529.31eV and 531.61eV in Ni-NiO-3 and Ni-NiO-4 respectively which confirms the formation of NiO and amorphous natured nickel based compound (Fig 4.6 (b) and (d)). Figure 4.6 (e) and (f) correspond to C1s peaks of carbon. Atomic concentration of carbon (1s) is about 30.48 %, oxygen (1s) 40.84 %, nickel (2p) 28.68 % in Ni-NiO-3. But the atomic concentration of nickel, oxygen and carbon in Ni-NiO-4 is slightly different from that of Ni-NiO-3 in which carbon (1s) is 11.13 %, oxygen (1s) is 46.68 % and nickel (2p) is 42.19 %.

4.3.5. X-ray photoelectron spectroscopy (XPS) analysis

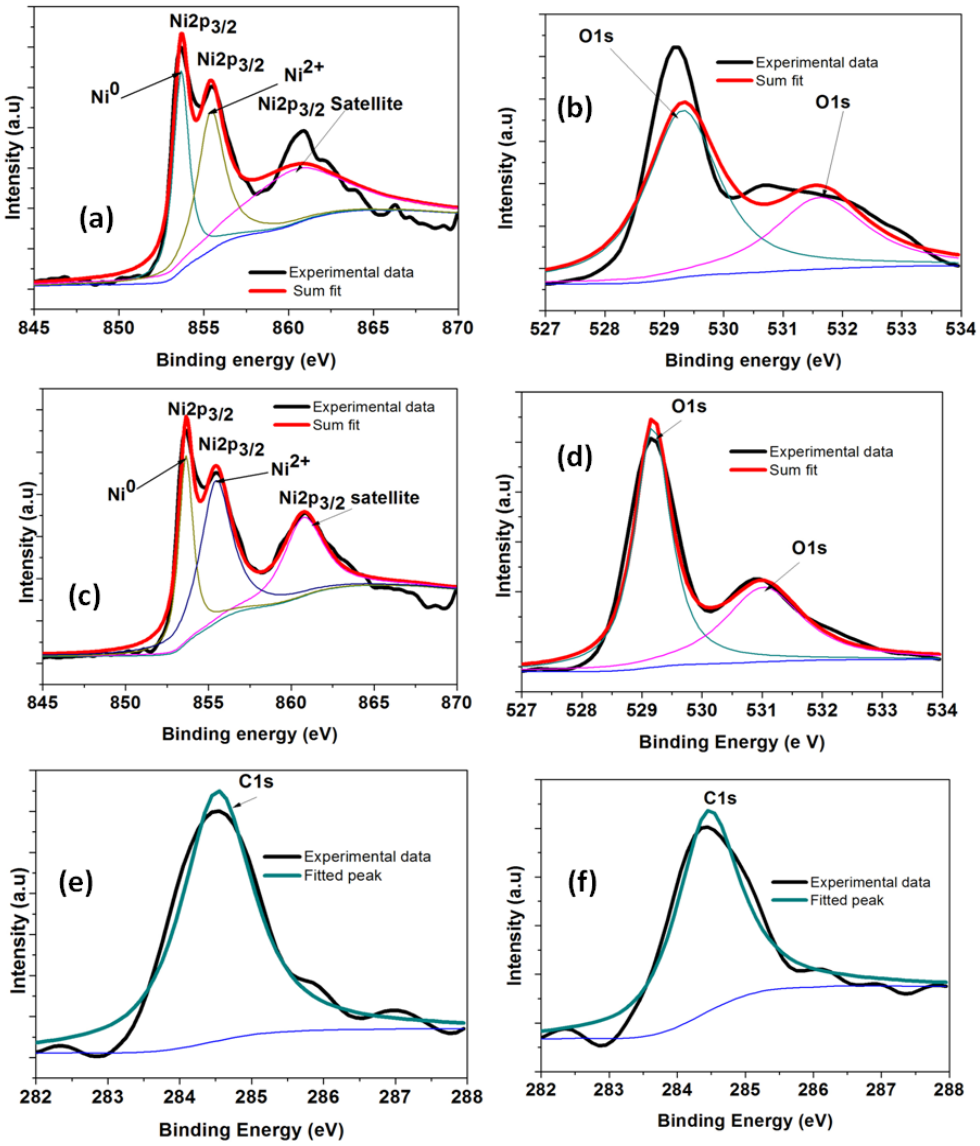

Fig.4.6*. XPS spectrum of Ni/NiO nanocomposites synthesized by solution combustion method : (a) Ni 2p of Ni-NiO-3 (b) O 1s of Ni-NiO-3 (c) Ni 2p of Ni-NiO-4 (d) O 1s of Ni-NiO-4 (e) and (f) are C1s peaks of Ni-NiO-3 and Ni-NiO-4 respectively.*

4.3.6. Transmission electron microscopy analysis

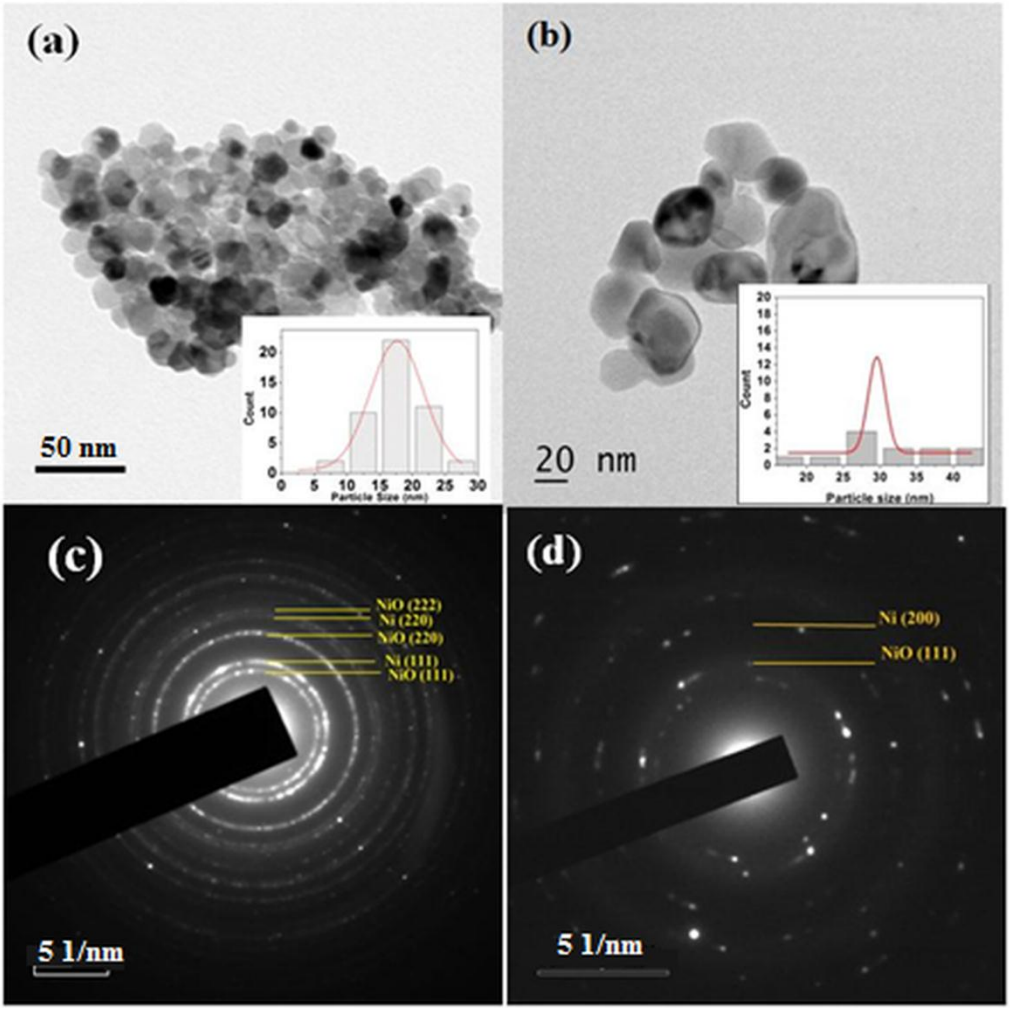

Fig. 4.7. *TEM images of Ni/NiO nanocomposites synthesized by solution combustion using (a) 30 ml HNO_3 with fuel to oxidizer ratio of 1:1 (Ni-NiO-3) (b) 30 ml HNO_3 with fuel to oxidizer ratio of 1:2 (Ni-NiO-4) (c) and (d) are SAED patterns of Ni-NiO-3 and Ni-NiO-4 respectively.*

Figure 4.7 (a) and (b) presents the transmission electron microscopy (TEM) images of Ni-NiO-3 and Ni-NiO-4. TEM images give an average particle size of 18 nm in Ni-NiO-3 and 29 nm in Ni-NiO-4. The selected area electron diffraction (SAED) pattern of Ni-NiO-3 and Ni-NiO-4 shows diffraction rings from the planes (111), (220), (222) of NiO and (200), (220), (111) of Ni (Fig .4.6 c & d).

4.3.7. Electrical properties

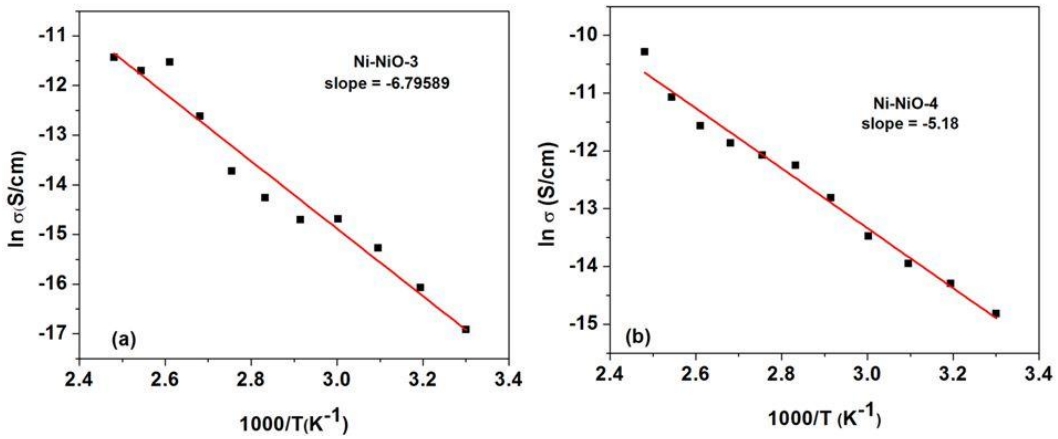

Fig.4.8. *Arrhenius plot of Ni/NiO nanocomposites synthesized by solution combustion method using (a) 30 ml of HNO_3 with fuel to oxidizer ratio of 1:1 (Ni-NiO-3) (b) 30 ml of HNO_3 with fuel to oxidizer ratio of 1:2 (Ni-NiO-4).*

Figure 4.8 present the Arrhenius plots of Ni-NiO-3 and Ni-NiO-4. The *d.c* conductivity of Ni-NiO-3 and Ni-NiO-4 samples is lower than that of Ni-NiO-1 and Ni-NiO-2 samples. As nickel concentration is relatively small in NiO rich Ni-NiO-3 and Ni-NiO-4, metallic Ni particles may be electrically isolated in it. This may be the reason for the lower conductivity in these samples when compared to nickel rich samples. Activation energy is calculated using the equation E_a = slope x 0.08625 eV [Hassan; 2014] for

Ni-NiO-3 and Ni-NiO-4 and the values obtained are 0.6 eV for Ni-NiO-3 and 0.4 eV for Ni-NiO-4. Higher order activation energy of Ni-NiO-3 indicates that its relatively low conductivity with respect to Ni-NiO-4.

4.3.8. Photocatalysis studies

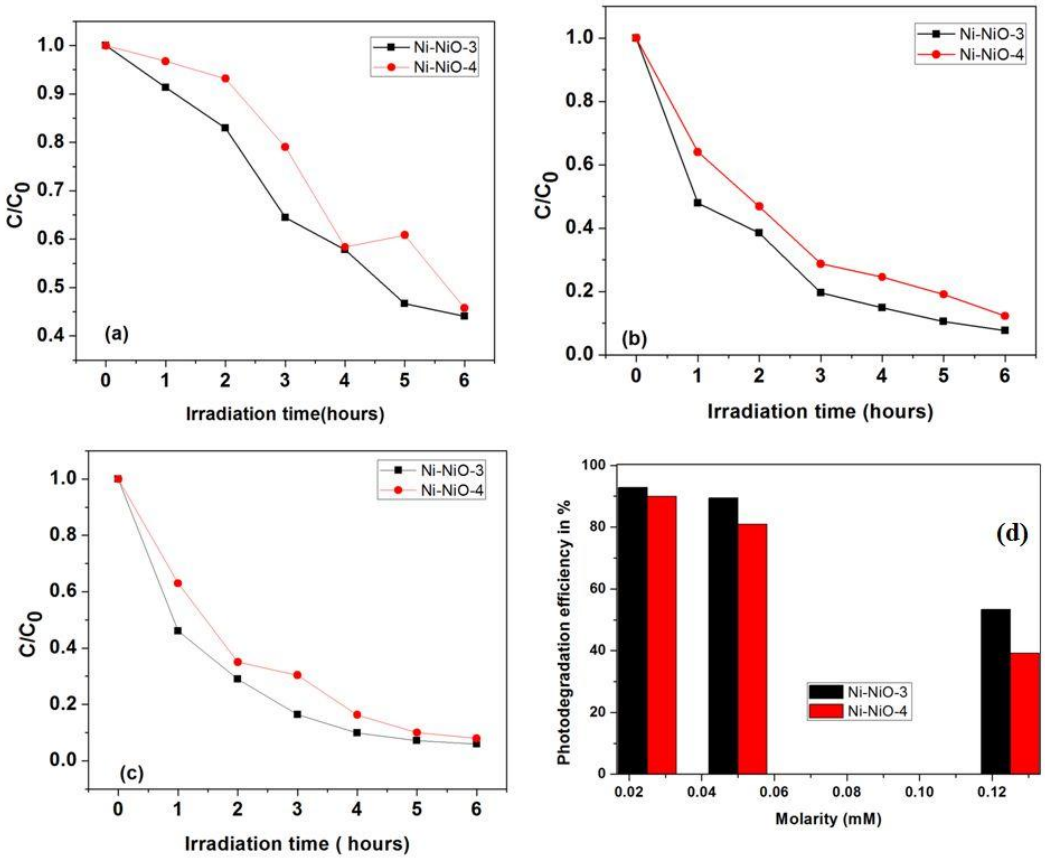

***Fig.4.9**. Photodegradation characteristics of Ni/NiO nanocomposites Ni-NiO-3, Ni-NiO-4 synthesized by solution combustion method at different molarities of MB solution under sun light exposure (a) 0.125 mM (b) 0.05 mM (c) 0.025 mM (d) histogram showing photodegradation efficiency of samples at 0.125, 0.05, 0.025 mM of MB.*

Table 4.2 *Photodegradation efficiency of Ni/NiO nanocomposites synthesized by solution combustion method.*

Molarity (mM)	Photodegradation efficiency in %	
	Ni-NiO-3	**Ni-NiO-4**
0.125	53	39
0.05	89	80
0.025	92	89

Figure 4.9 shows the results of photodegradation studies of Ni-NiO-3 and Ni-NiO-4 under different molar conditions of MB (0.125 mM, 0.05 mM and 0.025 mM) on exposure to sun light. Photodegradation efficiency of samples is calculated using the equation $(1-C_t/C_0)$ x100 % [Hayat *et al*; 2011] and the results of the samples under investigations on sunlight exposure is shown in table 4.2. Ni rich Ni-NiO-3 sample show better photo degradation efficiency with respect to Ni-NiO-4. The photodegradation efficiency of Ni-NiO-3 and Ni-NiO-4 are found to be 53 and 39 % with 0.125 mM of MB. Corresponding photodegradation efficiency at 0.025mM of MB these samples give the values of 92 and 89 %. This shows that photodegradation efficiency increases with decrease in molarity of MB. Heavy metal ions from contaminated water can be removed with porous materials like cellulose acetate nanofiber, amine functionalized MCM 41 by adsorption process [Chitpong *et al*; 2017, Showkat *et al*; 2007]. The explanation of photodegradation property of Ni-NiO-3 and Ni-NiO-4 is similar to that given in previous chapter.

4.3.9. Magnetic properties

4.3.9.1. Field dependent magnetization (M-H)

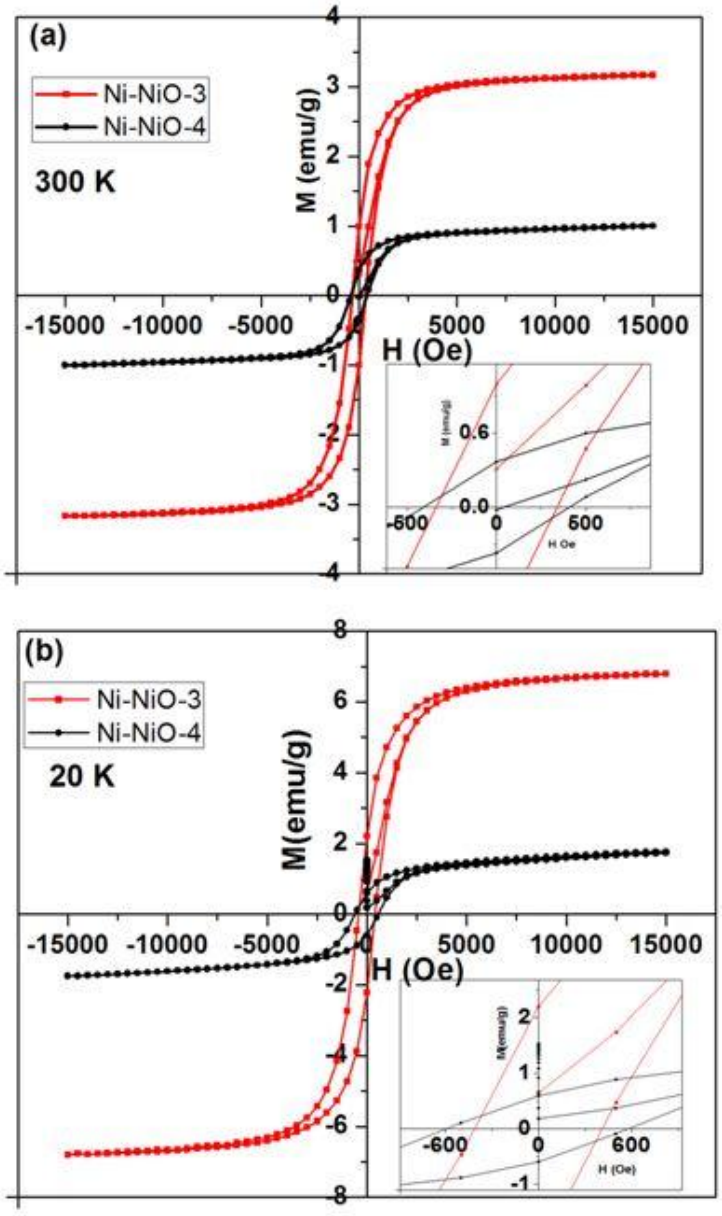

Fig.4.10. *Hysteresis curves (M-H) of Ni/NiO nanocomposites synthesized by solution combustion method using fuel to oxidizer ratio of 1:1(Ni-NiO-3) and fuel to oxidizer ratio of 1:2 (Ni-NiO-4) (a) 300 K (b) 20 K. Inset shows the enlarged portion of the central region of M-H curve.*

Saturation magnetization of the samples decreases with respect to increase in NiO content. The M_S of Ni-NiO-1 and Ni-NiO-2 is 54 emu/g and 34 emu/g respectively (chapter 3). Magnetic coercivity of these samples at room temperature is 80 Oe (Ni-NiO-1), 82 Oe (Ni-NiO-2) as reported previously by our group (chapter 3). But magnetic saturation value (M_S) of NiO rich Ni-NiO-3, Ni-NiO-4 is decreased (table 4.3) as compared to that of (Ni-NiO-1) and (Ni-NiO-2). Ni-NiO-3 give coercivity (H_C) value of 342 Oe and is having saturation magnetization (M_S) 3.2 emu/g at room temperature (table 4.3). H_C and M_S of this sample increases at 20 K which is about 409 Oe and 6.8 emu/g respectively (Fig.4.10). Interestingly, NiO rich sample N-NiO-4 shows higher order H_C (407 Oe) at room temperature as compared to Ni-NiO-3 at 300 K. Its coercivity is increased at 20 K and it gives a value of about 594 Oe. The average size of Ni rich Ni-NiO-1 and Ni-NiO-2 sample is 36 nm, 23 nm from the TEM images (chapter 3). But the TEM of NiO rich Ni-NiO-3 and Ni-NiO-4 has particle size 18 and 29 nm respectively. Interestingly, in NiO rich samples, decrease in Ni concentration implies that they are more isolated. The isolation of magnetic nickel particles from each other leads to reduction in magnetic interaction between nanoparticles which causes an increase in coercivity. Further, the size of Ni-NiO-4 is relatively larger than Ni-NiO-3, this may also contribute to the increase in coercivity of Ni-NiO-4.

Table 4.3 *Magnetic properties of Ni/NiO nanocomposites synthesized by solution combustion method by 30 ml HNO_3 and fuel to oxidizer ratio of 1:1 (Ni-NiO-3), 30 ml HNO_3 and fuel to oxidizer ratio of 1:2 (Ni-NiO-4).*

Sample	Crystallite size (nm) from XRD		300 K $M_s M_r H_c$			20 K $M_s M_r H_c$		
	Ni	NiO	(emu/g)	(emu/g)	(Oe)	(emu/g)	(emu/g)	(Oe)
Ni-NiO-3	36	36	3.2	1	342	6.8	2.2	409
Ni-NiO-4	44	21	0.99	0.37	407	1.8	0.6	594

Ferromagnetic Ni and antiferromagnetic NiO in a Ni-NiO system are expected to give higher order of exchange bias at low temperature. But we observed negligible exchange bias which is probably attributed to the amorphous carbon content that is evident from the presence of G and D bands in Raman and IR spectra (Table. 4.1).

Field cooling (FC) and zero field cooling (ZFC) curves of both the sample are shown in Fig. 4.11 (a) and (b). Magnetization slightly increases with the decrease of temperature under FC. However, ZFC magnetization almost linearly decreases with respect to the decrease of temperature. The FC and ZFC meet around 300 K in both the samples (Blocking temperature) which indicate the ferromagnetic nature of the sample at room temperature. Figure 4.11 (c) presents the plot of M_{FC}- M_{ZFC} (M_{irr}) versus temperature of Ni-NiO-3 and Ni-NiO-4. It can be seen from the figure that magnetic irreversibility (M_{irr}) for Ni-NiO-3 is 0.5 emu/g whereas that of Ni-NiO-4 is 0.183 emu/g.

4.3.9.2. Temperature dependent magnetization (M-T)

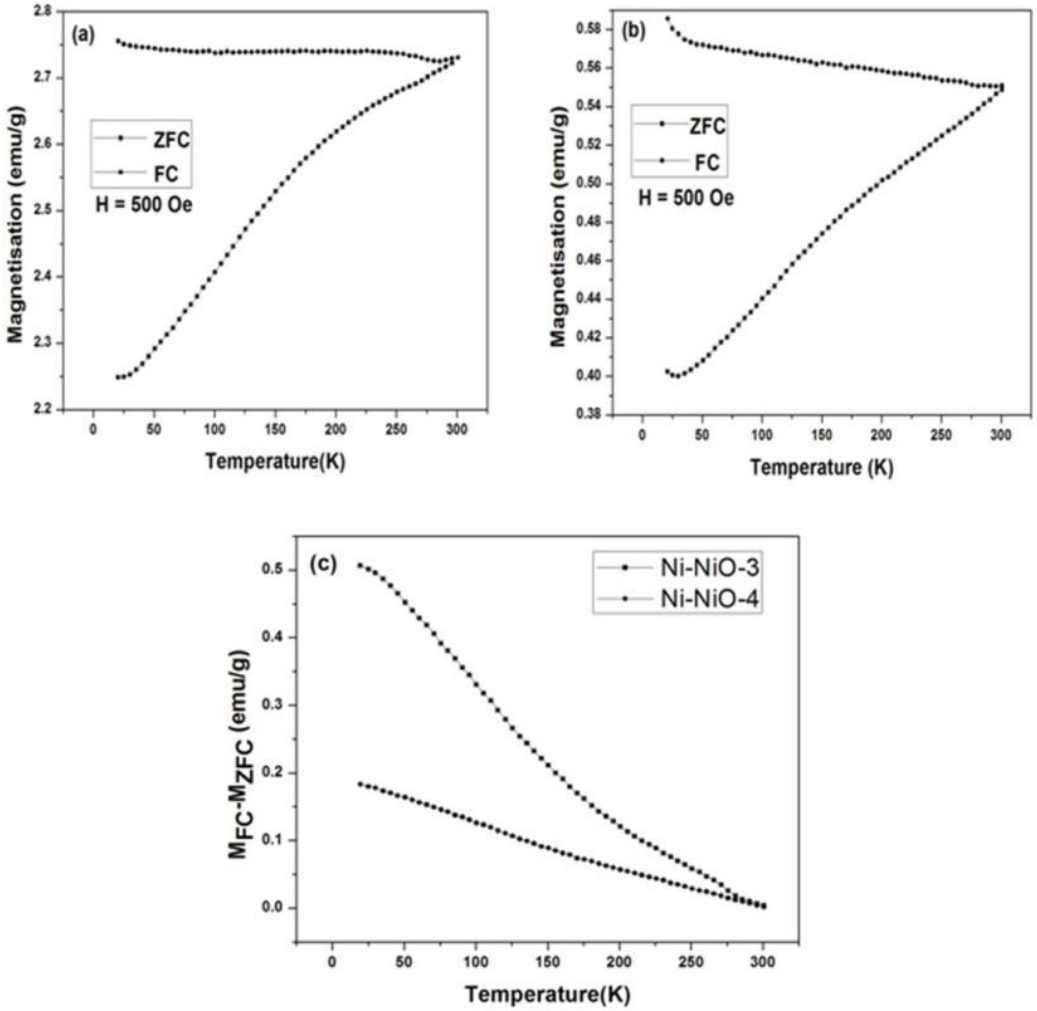

Fig 4.11. *FC and ZFC curves (at an applied field of 500 Oe) of Ni/NiO nanocomposites synthesized by solution combustion method using (a) fuel to oxidizer ratio of 1:1 (Ni-NiO-3) (b) fuel to oxidizer ratio of 1:2 (Ni-NiO-4) (c) plot between M_{FC}-M_{ZFC} (M_{irr}) versus temperature of Ni-NiO-3 and Ni-NiO-4.*

4.4. Conclusions

NiO content of Ni/NiO nanocomposites synthesized using solution combustion can be varied by changing fuel to oxidizer ratio used for the synthesis. Nickel in NiO exists in 2p oxidation state and oxygen is in 1s state, which was understood from XPS measurement. Amorphous carbon matrix exists in NiO rich Ni/NiO samples as evidenced from Raman data in which I_D/I_G ratio is more than 1. Increase in electrical conductivity with temperature for NiO rich Ni/NiO is due to the presence of antiferromagnetic semiconducting NiO. Thermal activation energy increased with respect to Ni content in NiO rich Ni/NiO nanocomposites. Sunlight assisted photodegradation process of methylene blue is contributed by the surface plasmon resonance of Ni in Ni-NiO composite system. The decrease in nickel content in NiO rich Ni/NiO nanocomposites may lead to the isolation of magnetic nickel nanoparticles with less magnetic interaction resulting in increase in magnetic coercivity. High coercivity values shown by the NiO rich Ni/NiO at room temperature are good for magnetic storage applications. Multifunctional Ni/NiO nanocomposites in amorphous matrix can be used for magnetic, electrical and photocatalytic applications.

Chapter-5

Contents

Photocatalytic and Magnetic Properties of Electrically Conducting Ni/NiO nanocomposites Embedded in Graphite and Graphene Matrix

5.1 Introduction

Carbon/metal/metal oxide nanostructures, especially carbon/ nickel/nickel oxide system brings considerable attention because of its unique properties and technological applications.Kahimbi*et al* synthesised NiO/reduced grapheneoxide by ball milling method which is suitable for supercapacitor applications [Kahimbi*et al*; 2017]. Carbon nanoparticles encapsulated in hollow nickel oxide shows better efficiency for supercapacitor applications [Fan*et al*; 2012]. Cobalt-nickeloxide/ C/Ni/CNTs nanocomposites is good for electrochemical capacitors as electrode materials [Kang *et al*; 2015], Ni-activated carbon nanocomposites is used as hydrogen storage materials [Figueroa-Torres *et al*; 2012], MWCNT/nickel nanocomposites shows electron transport and electrocatalytic properties [Adekunle*et al*; 2010], C/Ni@NiO/Al_2O_3 compositesis used as anode materials for Li-ion batteries [Liang *et al*; 2013] and nickel-graphene composites show good mechanical properties [Ren*et al*; 2015] etc. A very few reports are found in the literature in which

carbon based Ni/NiOnanocomposites show conducting, photocatalytic and magnetic properties. Some of the metallic-carbon materials are exhibiting catalytic properties in the presence of light. Fang *et al* reported photocatalytic hydrogen evolution properties of nickel nanoparticles coated with graphene layers [Fang *et al*; 2017]. Zirconium doped nickel cobalt ferrite-graphenenanocomposite is used as visible light based photocatalyst [Rasheed*et al*; 2016]. Nickel-ferrite-graphene, graphene/Ni/TiO_2/CNT composites are photocatalytic materials [Zhao *et al*; 2014,Hui *et al*; 2014]. Apart from this nickel based carbonaceous materials are showing morphology dependent magnetic properties. Ji *et al* synthesized reduced graphene oxide/Ni nanocomposites and studied its magnetic properties [Ji*et al*; 2012]. Thin film nanocomposites of nickel nanoparticles homogenously embedded in the amorphous carbon matrix shows superparamagnetic behavior and its blocking temperature is about ~13 K [Fonseca *et al*; 2005].

NiO/reduced graphene oxide nanocomposites can be synthesized by ball milling of bulk nickel and graphite [Kahimbi*et al*; 2017]. Carbon nanoparticles encapsulated in hollow nickel oxide were synthesized using hydrothermal method [Fan*et al*; 2012], Ni-activated carbon nanocomposites prepared through electroless deposition [Figueroa-Torres *et al*; 2012], nickel-graphene composites by electrochemical deposition [Ren *et al*; 2015], graphene/NiOnanorod composites using solvothermal method [Zahraei*et al*; 2015] and hybrid NiO/Ni/graphenenanocomposite prepared by an electrical wire explosion process [Lee*et al*; 2014] etc. Zhou *et al* prepared Ni/graphene composite from the precursorsgraphene oxide gel and nickel acetate [Zhou *et al*; 2016]. Mansour *et al* reported carbon/nickel nanocomposites prepared by sol-gel method [Mansour *et al*; 2015]. Outof

these methods, solution combustion method can give good yield and very simple procedure is required to carry out the synthesis. In this chapter we are describing this simple method for the synthesis of Ni rich Ni-NiOnanocomposites with graphite/graphene as matrix and its electric, photocatalytic and magnetic properties.

5.2. Experimental

5.2.1 Synthesis

All the reagents used for the synthesis were of AR grade and obtained from SpectrochemPvt Ltd. Mumbai, India. Graphite/Ni-NiOnanocomposites(Ni-NiO-GT) was prepared from precursor solutions made by dissolving 6 g of nickel acetate, 12 g of citric acid in 20 ml of water separately and then adding 0.9 g of graphite powder. All these reactants were transferred to a 1000 ml beaker and stirred well. To this, 30 ml of HNO_3 was poured, ammonia solution was added to the above solution to adjust the pH to 7. The beaker was then placed on a preheated hot plate, nearly for one hour to occur the combustion reaction. Ash like powder was obtained after the combustion process, collected samples were ultrasonicated using isopropanol for 3 hour and dried. Graphene added Ni-NiOnanocomposites (Ni-NiO-GE) was synthesized by adding graphene instead of graphite with above mentioned protocol.

5.2.2 Characterization

XRD analysis of the samples wereperformed using PANALYTICAL XPERT-PRO X-ray diffractometer with CuKα radiation (1.5404 Å). Fourier Transform Infra Redspectroscopy (FTIR) of the samples were done

with JASCO FTIR 4100 spectrometer with KBr pellet method in the range 400-4000 cm^{-1}. A Horiba JobinYvonLabRAM HR system (resolution of the order of $3cm^{-1}$) equipped with He-Ne laser (632.8 nm) were used for the Raman spectral recording. TEM and HRTEM measurements were performed with a JEOL JEM 2100 model High Resolution Transmission Electron Microscope (HRTEM) operated at 200 KeV equipped with EDAX and SAED detector. Morphology of the samples was examined by using Carl Zeiss, sigma HV model Field emission scanning electron microscope (FE-SEM). ElementarVario EL III C-H-N analyser was used to know the presence of carbon, hydrogen, nitrogen in the samples. Thermal analysis of the samples was carried out with Perkin Elmer, Diamond TGA.X-ray photoelectron spectroscopy (XPS) analysis of the samples were performed by using Kratos AXIS Ultra spectrometer with AlKα radiation. *d.c* electrical conductivity measurement of the samples under study was carried out using Keithley model 2400 source meter automated with Lab-VIEW software.Photocatalytic studies were carried out by measuring the absorbance of the methelyne blue (MB) dye using UV-VIS-NIR spectrometer (JASCO-V-570). Magnetic properties of the samples were taken with Lakeshore make Model 7410 Vibrating Sample Magnetometer (VSM).

5.2.3 Photodegradation studies

Photodegradation properties of the samples were measured by using MB as a test solution. 0.025 mM MB solution was prepared and taken into borosil bottles (5ml volume capacity). Catalyst loading was fixed to 5 g/L and the bottles were placed under direct sun light for the photocatalytic experiments. Absorption measurements of remnant MB solution were

performed with UV-VIS-NIR spectrometer after each one hour exposure to solar radiation.

5.3. Results and discussion

5.3.1. X-ray diffraction analysis

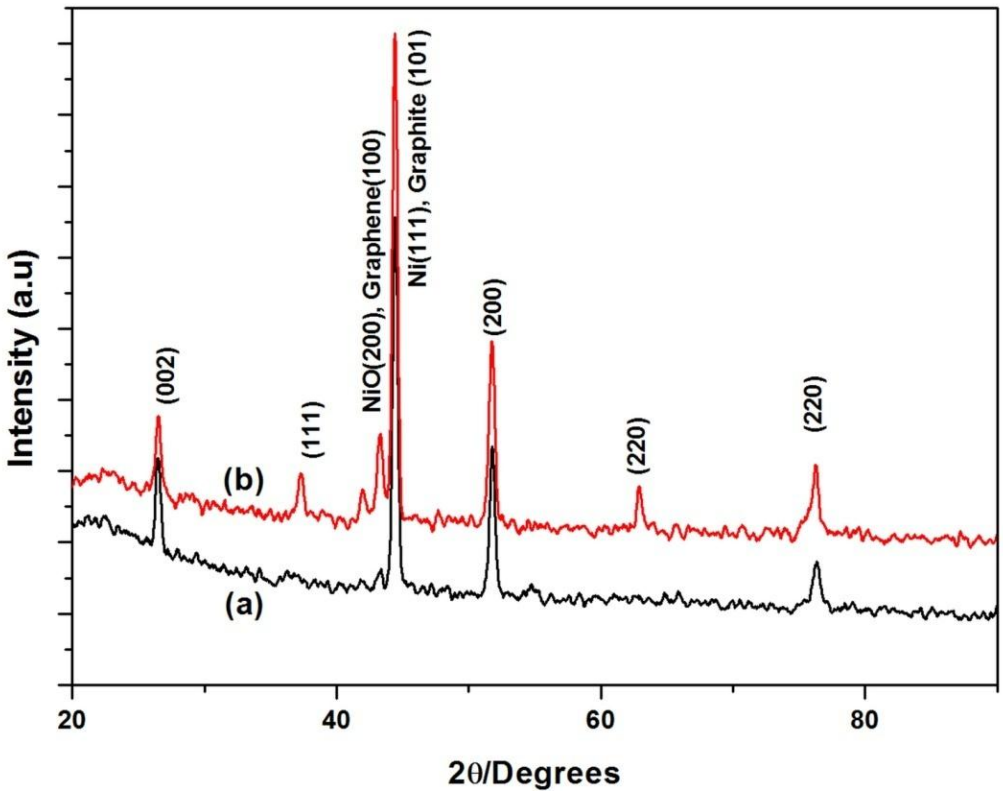

Fig. 5.1. *X-ray diffraction patterns of Ni-NiOnanocomposites synthesized with graphite, graphene and precursor salt of Ni/NiO (a) Ni-NiO-GT (b) Ni-NiO-GE.*

XRD pattern of Ni-NiO-GT has diffraction peaks almost similar to Ni rich Ni-NiOnano composite discussed previously (chapter 3). In addition to Ni diffraction peaks, a diffraction peak is seen at 2θ value of 26.5^0 assigned to graphite (002) (Fig.5.1). XRD pattern of Ni-NiO-GE is having diffraction peaks correspond to NiO at 2θ value 37.4^0 (111), 43.3^0 (200),

62.7^0 (220) and Ni at 2θ value of 44.5^0 (111), 51.8^0 (200), 76.5^0 (220) along with graphene at 26.5^0 (002). Unambiguous assignment of diffraction peaks at 44.4^0 and 43.3^0 of Ni-NiO-GT and Ni-NiO-GE respectively is limited since diffraction from planes (111) of Ni, (101) of graphite, (200) of NiO and (100) of graphene are expected in this position. Reference intensity ratio method (RIR) is used to calculate the weight percentages of Ni and NiO in both the samples [Hubbard*et al*; 1988]. In Ni-NiO- GT, the weight percentages of Ni and NiO are 64 and 36 % where as Ni-NiO-GE has 54 and 46 % of Ni and NiO respectively. From this one can conclude that NiO weight percentage is relatively higher in Ni-NiO-GE compared to Ni-NiO-GT. Average grain size of Ni in Ni-NiO-GT and Ni-NiO-GE calculated usingScherrer's formula [Cullity; 1956] based on the strongest diffraction peak of Ni at 2θ value of 44.4^0 is 23 and 22 nm . These values are less than the grain size obtained for Ni (38 nm) embedded in amorphous carbon matrix discussed previously (chapter 3). The presence of graphite and graphene in both crystal growth systems may hinder the agglomeration of Ni nanoparticles into relatively smaller one. This in turn contributes to reduction in size of Ni in Ni-NiO-GT and Ni-NiO-GE with respect to Ni in amorphous carbon matrix.

5.3.2. Fourier transform infrared (FTIR) and Raman vibrational spectroscopy analysis

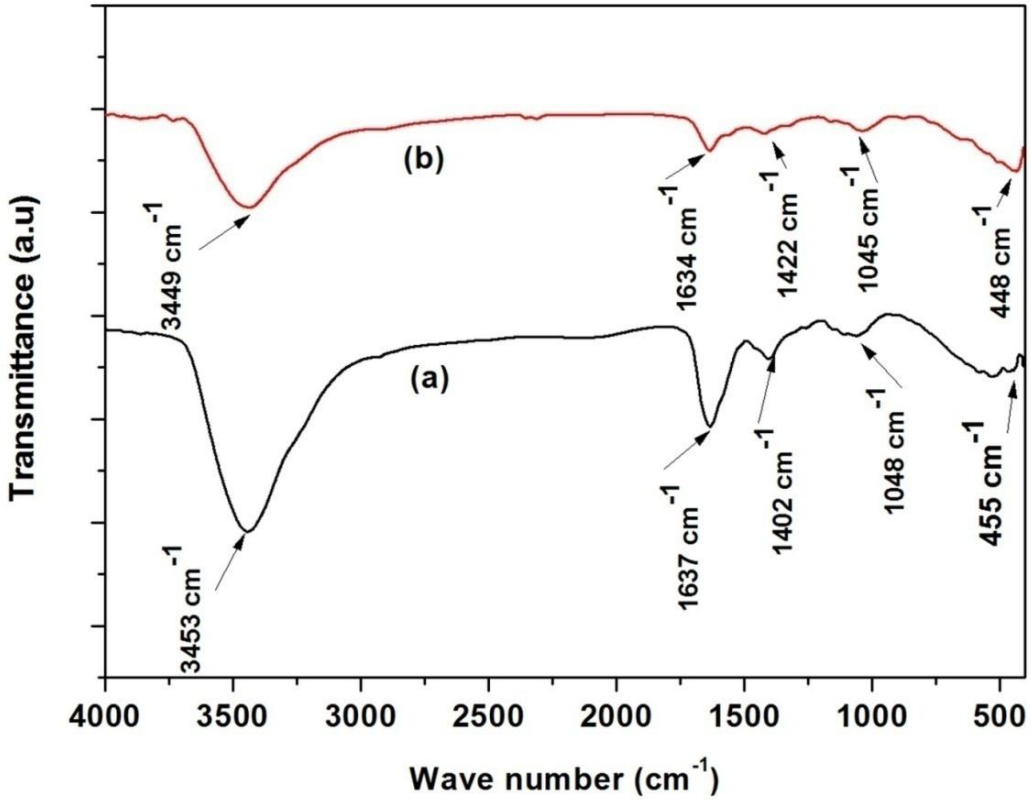

Fig. 5.2.*FTIR spectra of Ni-NiOnanocomposites synthesized with graphite, graphene and precursor salt of Ni/NiO (a) Ni-NiO-GT (b) Ni-NiO-GE.*

Table 5.1 gives the details of Raman and FTIR bands observed for Ni-NiO-GT and Ni-NiO-GE respectively. Ni-NiO-GT is having weak bands at 189 and 495 cm^{-1} in the Raman spectra contributed to NiO vibrations and the values are close to the previous report [Patange *et al*; 2015]. But in the IR spectra, a weak band is seen at 445 (Ni-NiO-GT) and 448 cm^{-1} (Ni-NiO-GE) are due O-Ni-O stretching vibrations in conformity with XRD of Ni-

NiO-GT and Ni-NiO-GE where diffraction peaks related to NiO is present (Fig. 5.2). The observed bands are close to the earlier reports [Rahdar*et al*; 2015, Yousefi *et al*; 2016]. The absence of Raman band related to NiO in Ni-NiO-GE is probably due to the presence of light absorbing graphene environment.

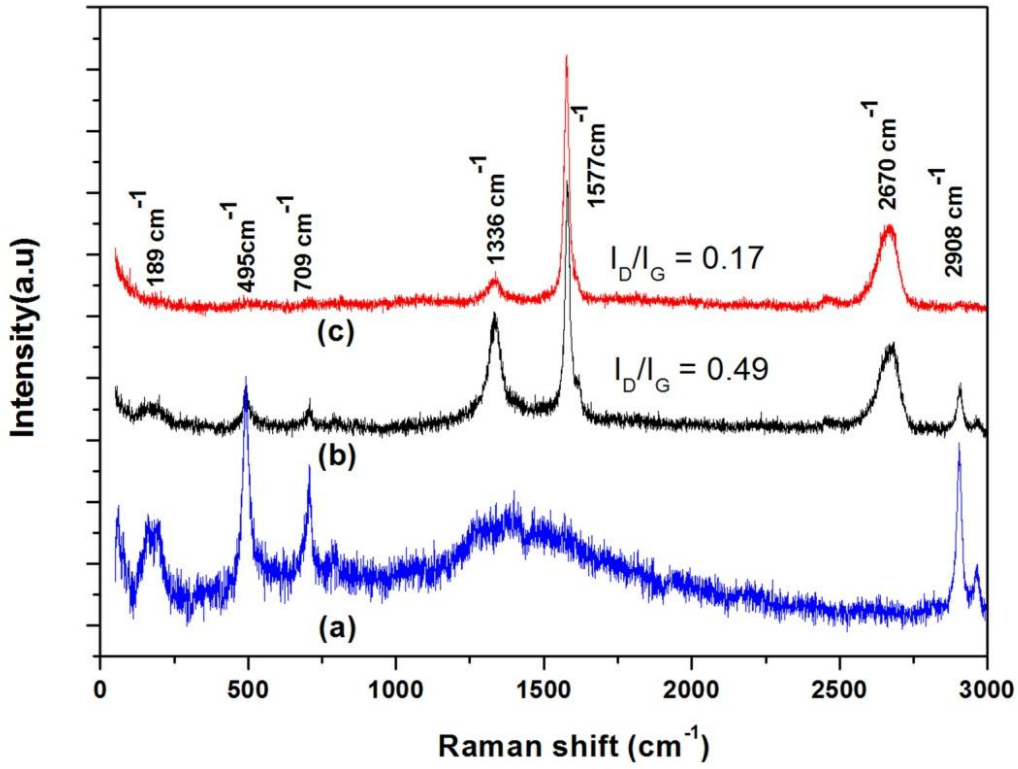

Fig. 5.3.*Raman spectra of Ni-NiOnanocomposites synthesized with graphite, graphene and precursor salt of Ni/NiO (a) Ni rich Ni-NiO (b) Ni-NiO-GT (c) Ni-NiO-GE.*

Table 5.1 *FTIR and Raman data of Ni-NiO nanocomposites synthesized with graphite, graphene and precursor salt of Ni/NiO (cm^{-1}).*

Ni-NiO-GT		**Ni-NiO-GE**		**Assignments**
FT-IR	Raman	FT-IR	Raman	
	189 vw			Lattice mode
445 w		448 w		νNiO
	495 w			νNi-O (1LO mode)
	709 vw			2TO of NiO
1048 w				νC-O
	1336 s		1336 w	D band
1402 w				C-OH bending vibrations
	1577 vvs		1577 vvs	G band
1637 s		1634 s		OH bending vibration or νC=C
	2670 s		2670 s	2D band
	2908 w			D+G band
3453 vs		3449 vs		νO-H

The presence of Raman peaks in Ni-NiO-GT is due to higher order distortion of NiO_6 octahedra. A very weak band located at 709 cm^{-1} is due to 2TO mode of NiO. Weak FTIR band observed at 1048 in Ni-NiO-GT is due to carbon and oxygen related impurities [Fu *et al*; 2014]. The characteristic peaks of graphite and graphene is evidenced by the presence of D and G bands and their harmonics in the Raman spectra. Raman band seen at 1336 cm^{-1} in the both samples is attributed to sp^3 hybridized D band, strong Raman bands at 1577 cm^{-1} in the both the sample are attributed to G band (Fig.5.3). A few weak bands are also seen in the IR spectra of the both the samples (table 5.1). Raman spectra of Ni-NiO-GT is having a band at 2908 cm^{-1}, which is a combination of D and G band. Some of the adsorbed hydroxyl group (OH) may produce C-OH vibrations at 1400 cm^{-1} [Peng *et al*; 2013,Trapalis *et al*; 2016]. In the present case this band is weak and observed at 1402 cm^{-1} in Ni-NiO-GT. Strong IR band seen at 1634-1637 cm^{-1} region may be ascribed to OH bending vibrations of water or C=C vibrations of graphite and graphene structure [Trapalis *et al*; 2016]. The I_D/I_G value of Ni-NiO-GT is 0.49 which is higher than that of Ni-NiO-GE (0.17). It can be understood from this observation that, defect levels of carbon is more in Ni-NiO-GT than Ni-NiO-GE, indicate that carbon present in Ni-NiO-GE is more crystalline than Ni-NiO-GT.

5.3.3. TEM, HRTEM, SAED analysis

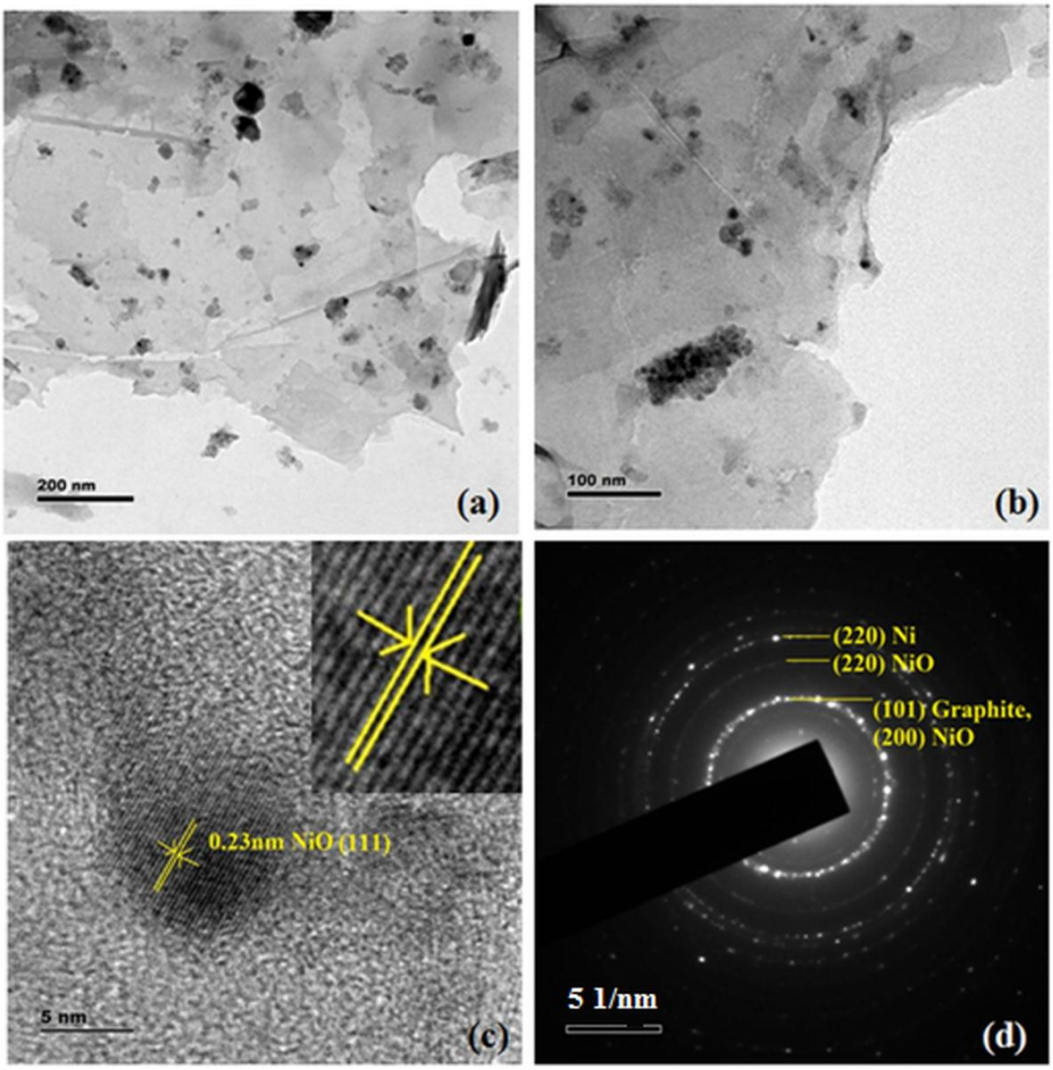

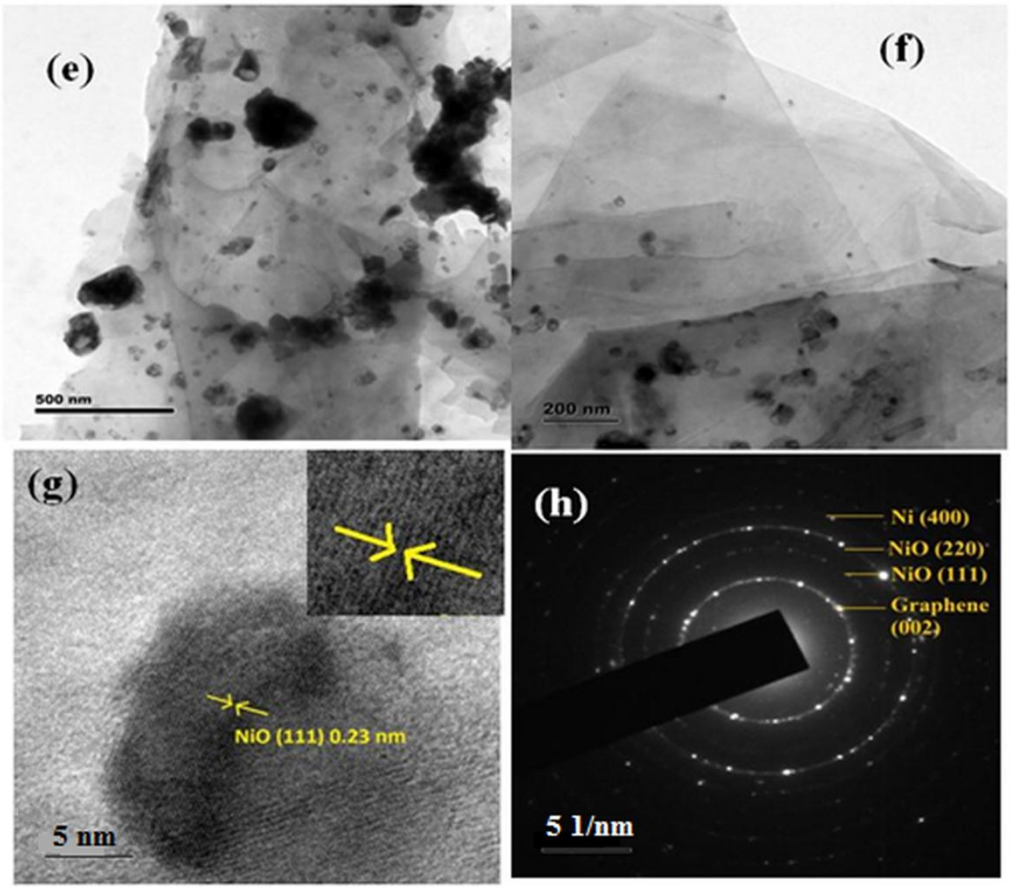

Fig. 5.4.*TEM images of Ni-NiOnanocomposites synthesized with graphite, graphene and precursor salt of Ni/NiO (a) & (b) TEM images at different resolutions of Ni-NiO-GT (c) HR-TEM image of Ni-NiO-GT (d) SAED pattern of Ni-NiO-GT, (e) &(f) TEM images at different resolutions of Ni-NiO-GE (g) HR-TEM image of Ni-NiO-GE (h) SAED pattern of Ni-NiO-GE.*

TEM images show that metallic Ni/NiO nanoparticles are dispersed in graphitic system (Fig. 5.4 (a) and (b)). These particles are seen to be agglomerated due to the local sintering attributed to the instantaneous high reaction temperature of solution during combustion process. In the case of Ni-NiO-GE, Ni-NiO nanoparticles are embedded in graphene layer and are agglomerated (Fig. 5.4 (e) and (f)). From the HR-TEM of Ni-NiO-GT sample the inter planar spacing is calculated to be 0.23 nm and it

corresponds to the plane (111) of NiO. SAED pattern of Ni-NiO-GT shows diffraction rings from the planes (200), (220) of NiO and (220) plane of Ni. In Ni-NiO-GT, diffraction ring corresponds to (101) plane is due to graphite (Fig.5.4 (d)). HR-TEM of Ni-NiO-GE shows inter planar spacing of 0.23 nm of NiO (111) plane (Fig. 5.4 (g)). SAED pattern of Ni-NiO-GE gives diffraction rings due to NiO (111), (220) planes and to Ni from the plane (400). Diffraction ring from (002) plane of graphene is also observed from this sample.

5.3.4. EDAX analysis

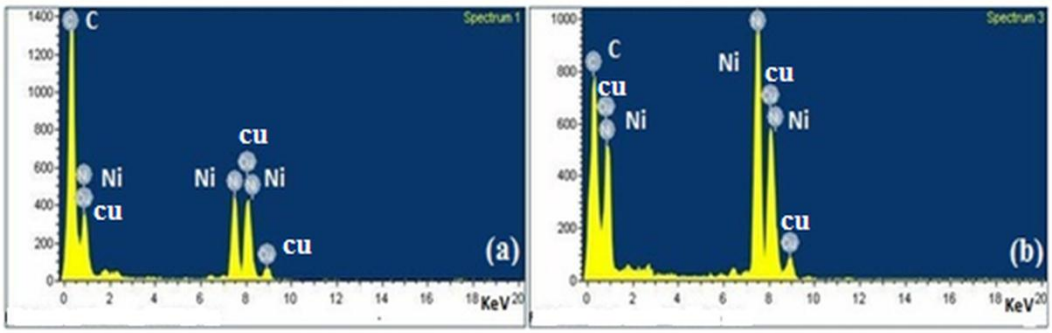

Fig. 5.5.*EDAX spectra of Ni-NiO nanocomposites synthesized with graphite, graphene and precursor salt of Ni/NiO (a) Ni-NiO-GT (b) Ni-NiO-GE.*

EDAX gives that, carbon atomic percentage is 72.67 % and that of Ni is about 13.34 % in Ni-NiO-GT. Ni-NiO-GE has carbon atomic percentage about 40 % and Ni is 37.52 %. From the EDAX analysis oxygen is not seen which suggest that Ni-NiO-GT and Ni-NiO-GE is mainly consists of Ni as a major content (Fig. 5.5). CHN analysis of Ni-NiO-GT gives 17.85 % carbon where as 14.88 % in the Ni-NiO-GE sample.

5.3.5. FESEM analysis

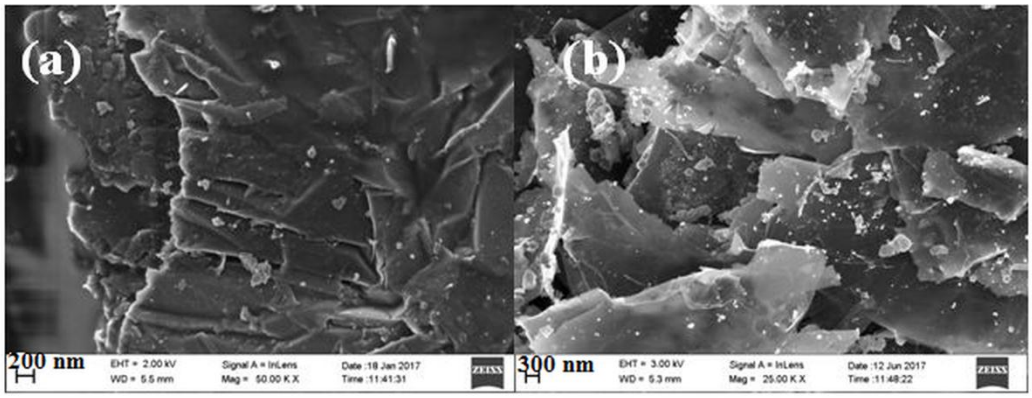

Fig.5.6. *FE-SEM images of Ni-NiO nanocomposites synthesized with graphite, graphene and precursor salt of Ni/NiO (a) Ni-NiO-GT (b) Ni-NiO-GE.*

In figure 5.6 (a) multilayer of graphite is found in the sample, Ni/NiO nanoparticles are dispersed on the graphite sheets. Figure 5.6 (b) shows that graphene layers are intermixed with Ni/NiO nanoparticles. In the present case graphite or graphene act as supporting matrix which likely to protect Ni/NiO nanoparticles from surrounding environment.

5.3.6. TGA analysis

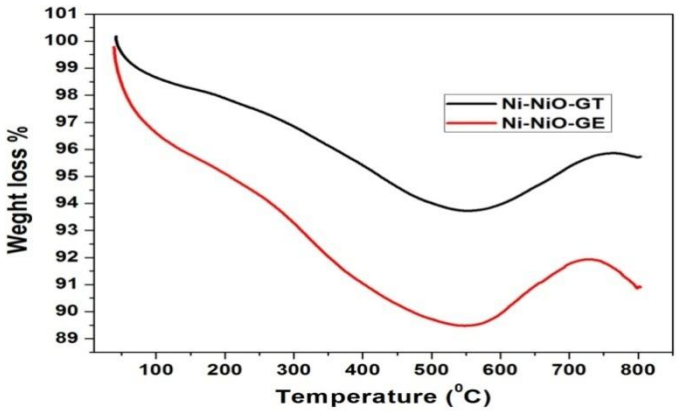

Fig.5.7. *TGA of Ni/NiO nanocomposites synthesized with graphite, graphene and precursor salt of Ni/NiO (a) Ni-NiO-GT (b) Ni-NiO-GE.*

Thermal stability and oxidation process of the samples are evaluated with TGA. Figure 5.7 shows TGA of Ni-NiO-GT and Ni-NiO-GE respectively. About 2% (±1.5) weight loss is observed for both Ni-NiO-GT and Ni-NiO-GE in the temperature range 40 to 100^0C (for Ni-NiO-GT) and 40 to 150^0C (for Ni-NiO-GE). After this, there is steady decrease of weight loss of sample in the case of Ni-NiO-GT. About 6.2 % weight is lost in the temperature interval from 150 to 550^o C. For the sample Ni-NiO-GE this weight loss is 10.5 %. This may be due to the conversion of carbon present in the sample in the form of graphite and graphene into carbon dioxide. There after weight gain observed from temperature 550 to 800^oC forming peak around 750^o C indicating the conversion of Ni to NiO.

XPS analysis reveals the presence of Ni, O, C which is consistent with the previously studied characterization tools (Fig. 5.8). In the case of Ni-NiO-GT, the peak seen at 855.99 eV and 861.42 eV (satellite) is attributed to $Ni2p_{3/2}$ of NiO [Tian *et al*; 2012]. Relatively weak peak is observed at 853.65 eV due to the presence of metallic nickel (Fig. 5.8(a)). Almost similar observations are found in the case of Ni-NiO-GE with slight differences in binding energies (Fig. 5.8(b)). Two peaks are obtained in the region 529 to 532 eV from both the samples, corresponds to O1s. The peak observed at ~529 eV in the samples Ni-NiO-GT and Ni-NiO-GE is attributed to NiO [Liu *et al*; 2015]. The peak seen at ~531 eV in both the samples is due to carbon and oxygen related bonds [Liu *et al*; 2015]. C1s peak of Ni-NiO-GT is observed at 284.76 eV, this peak is shifted to 279.26 eV in Ni-NiO-GE.

5.3.7. XPS analysis

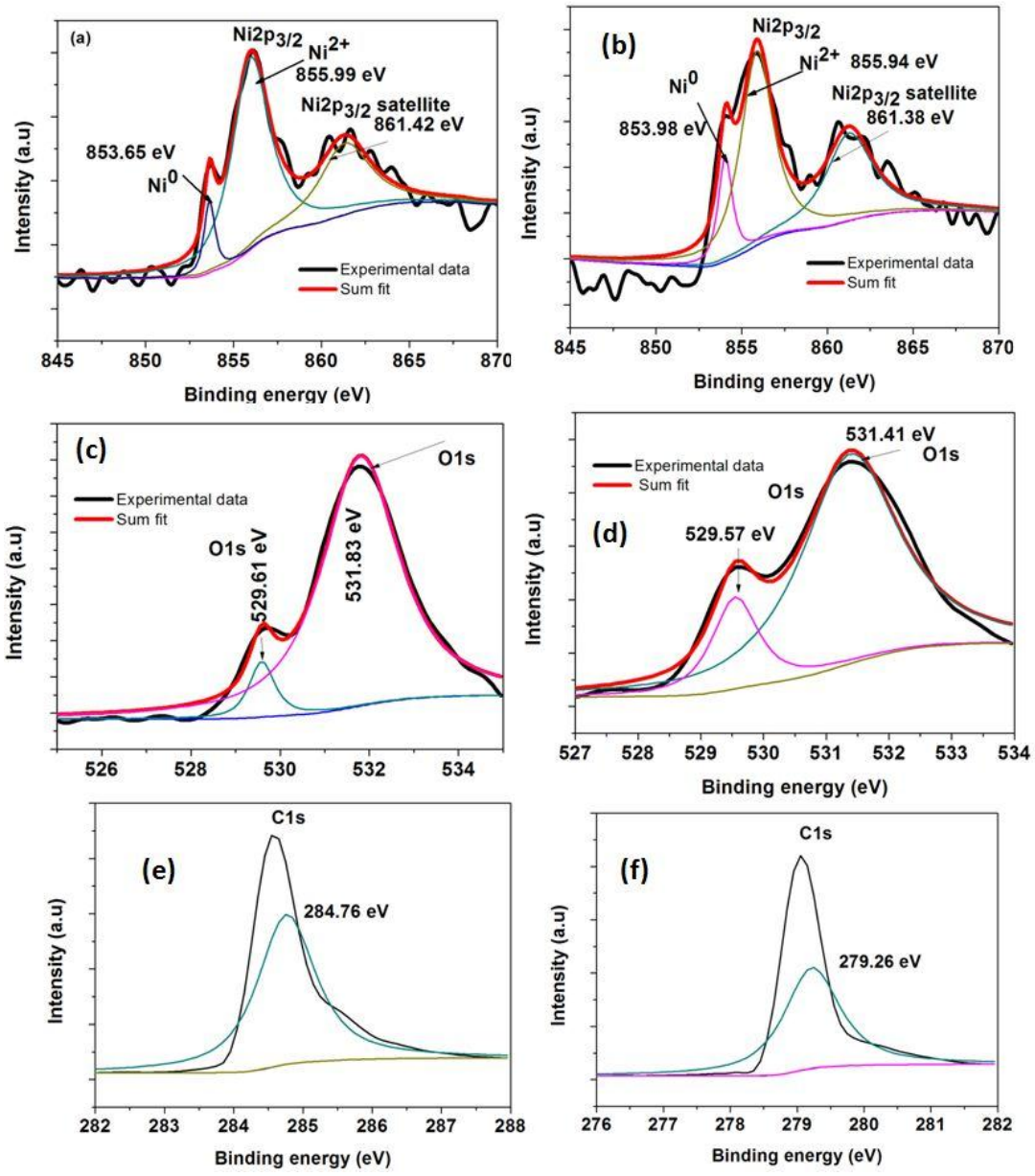

Fig.5.8. *XPS spectra of Ni/NiO nanocomposites synthesized with graphite, graphene and precursor salt of Ni/NiO (a) Ni2p of Ni-NiO-GT (b) Ni2p of Ni-NiO-GE (c) O1s of Ni-NiO-GT (d) O1s of N-NiO-GE (e) and (f) are C1s of Ni-NiO-GT and Ni-NiO-GE respectively.*

5.3.8. Electrical properties

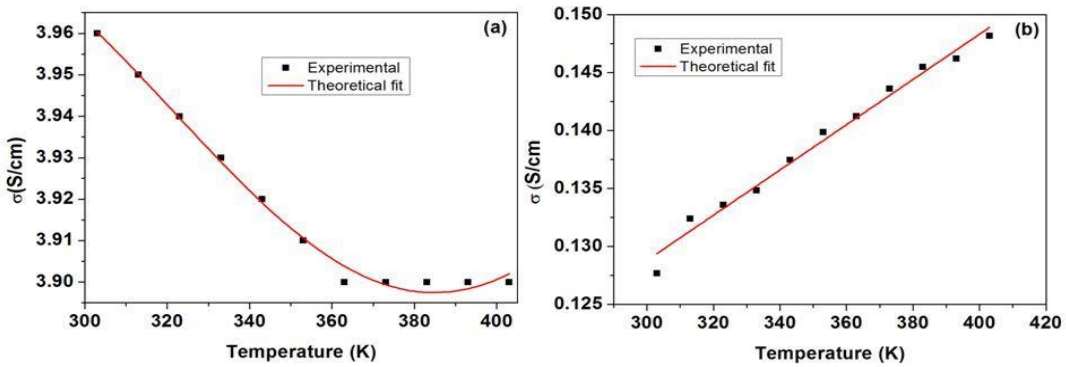

Fig.5.9.*d.c conductivity plots of Ni-NiOnanocomposites synthesized with graphite, graphene and precursor salt of Ni/NiO (a) Ni-NiO-GT (b) Ni-NiO-GE.*

Figure 5.9 shows the *d.c* conductivity plots of Ni-NiO-GT and Ni-NiO-GE. The *d.c* conductivity values of Ni-NiO-GT and Ni-NiO-GE are relatively less than Ni rich Ni-NiO which has a value of 24 S/cm (chapter 4). Ni-NiO-GT shows metallic behavior, in which conductivity decreases with increase in temperature and its room temperature *d.c*conductivity is 3.96 S/cm. But Ni-NiO-GE behaves like semiconductor and its conductivity is 0.13 S/cm at 300 K. Ni weight percentage is more in Ni-NiO-GT as understood from the XRD result. NiO content is more in Ni-NiO-GE from the XRD calculated by RIR method described previously. More Ni content in Ni-NiO-GT is responsible for the increases in conductivity as well as metallic conducting nature to the sample. Relatively higher amount of semiconducting NiO content in Ni-NiO-GE decreases the conductivity and the material behaves like semiconductor. From the Raman analysis the carbon present in Ni-NiO-GE is more crystalline than in Ni-NiO-GT. This increase in crystallinity of carbon causes the increase in number of grain boundaries. Electrons likely to scatter at the grain boundaries which decreases the conductivity of the sample.

5.3.9. Photocatalysis studies

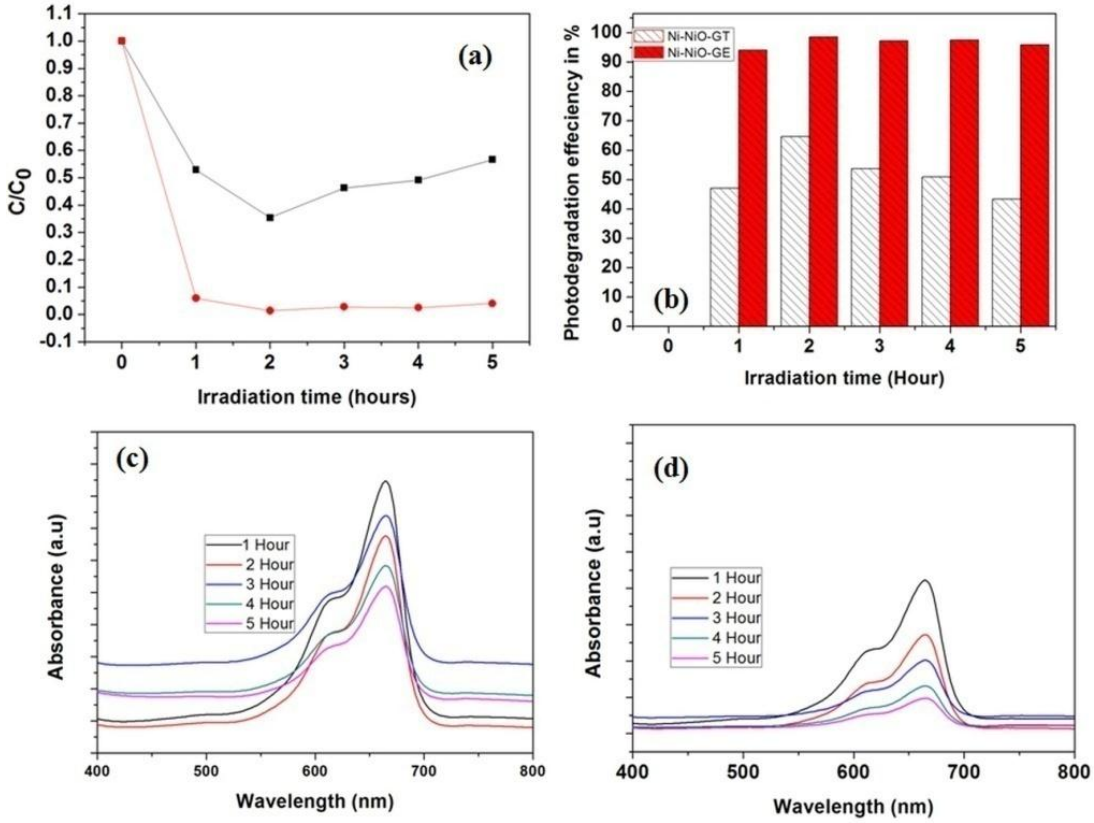

Fig.5.10. *Photodegradation characteristics of Ni-NiOnanocomposites synthesized with graphite, graphene and precursor salt of Ni/NiOunder sun light exposure by taking methylene blue as model system (a) C/C_0 plot of Ni-NiO-GT and Ni-NiO-GE (b) photodegradation efficiency of Ni-NiO-GT and Ni-NiO-GE (c) absorbance spectra of MB at different time durations with Ni-NiO-GT as photocatalyst (d) absorbance spectra of MB at different time durations with Ni-NiO-GE as photocatalyst.*

Figure 5.10 present the photodegradation characteristics of Ni-NiO-GT and Ni-NiO-GE under sun light exposure with MB solution as model dye system. Ni-NiO-GT shows about 43 % photodegradation efficiency while Ni-NiO-GE shows 96 % after five hours of sunlight irradiation. Photodegradation efficiency of both Ni-NiO-GT and Ni-NiO-GE is less

than Ni rich Ni-NiO under the same condition (chapter 4). Among the two samples, Ni-NiO-GT has about 64 % nickel content while Ni-NiO-GE with 54 %. Photocatalytic property of Ni-NiO is mediated by the activation of surface plasmon resonance of nickel nanoparticles (chapter 4). Hence sample with higher content of nickel is likely to show more photocatalytic efficiency. But in the present case, Ni-NiO-GE with less content of nickel with respect to Ni-NiO-GT shows higher photodegradation efficiency. The enhanced photocatalytic efficiency of Ni-NiO-GE is probably associated with combined effect of nickel and graphene system since grapheneposses relatively more surface area than that of graphite [Jain *et al*; 2014].

5.3.10. Magnetic properties

5.3.10.1. Field dependent magnetization (M-H)

Table 5. 2 *Magnetic properties of Ni-NiOnanocomposites synthesized with graphite, graphene and precursor salt of Ni/NiO.*

Sample	20 K			200 K			300 K		
	M_S (emu/g)	M_r (emu/g)	H_C (Oe)	M_S (emu/g)	M_r (emu/g)	H_C (Oe)	M_S (emu/g)	M_r (emu/g)	H_C (Oe)
Ni-NiO-GT	50	6	139	47	5	113	33	5	118
Ni-NiO-GE	32	3.5	125	31	2.5	96	34	2.2	78

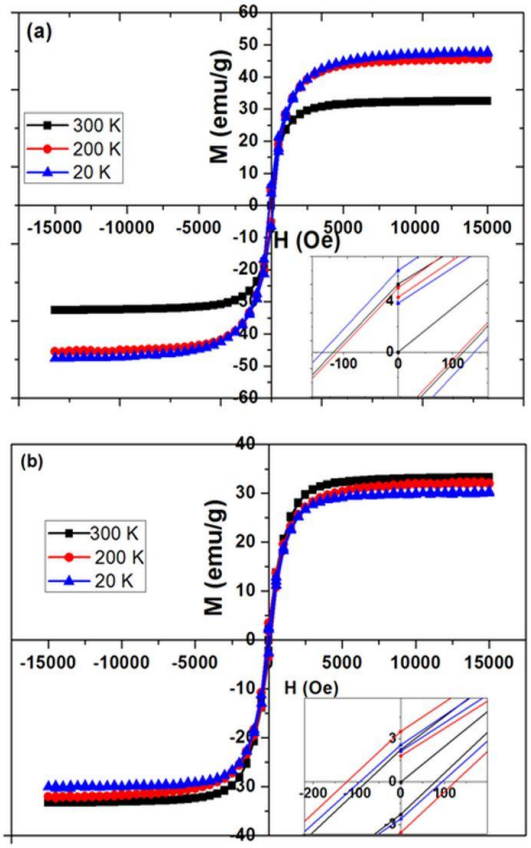

Fig.5.11. *M-H characteristics of Ni-NiOnanocomposites synthesized with graphite, graphene and precursor salt of Ni/NiO at different temperatures (a) Ni-NiO-GT (b) Ni-NiO-GE.*

Figure 5.11 shows the M-H characteristics of Ni-NiOnanocomposites with graphite and graphene synthesized by solution combustion method. From the Fig. 5.11 it can be observed that all the samples behave like ferromagnetic material at 20, 200, 300 K. In the case of Ni-NiO-GT saturation magnetization (M_s) is obtained as 50 emu/g (20 K). Saturation magnetization decreases with respect to increase of temperature which shows a value of 33 emu/g at 300 K (table 5.2). There is no appreciable change in value of remanant magnetization of Ni-NiO-GT with respect to temperature. Magnetic coercivity of Ni-NiO-GT is 139, 113, 118 Oe respectively at 20, 200, 300 K. It is interesting to note that magnetic

coercivity of Ni-NiO-GT is higher than that of Ni rich Ni-NiO (~80 Oe) discussed previously (chapter 3). Figure 5.11(b) presents the M-H behavior of Ni-NiO-GE at 20, 200, 300 K. Variation of M_s and M_r is feeble with respect to increases in temperature. $H_c$of this sample at 20 K is 125 Oe, which decreases with respect to temperature. Room temperature coercivity is 78 Oe which is less than that of Ni rich Ni-NiO (chapter 3).

5.3.10.2. Temperature dependent magnetization (M-T)

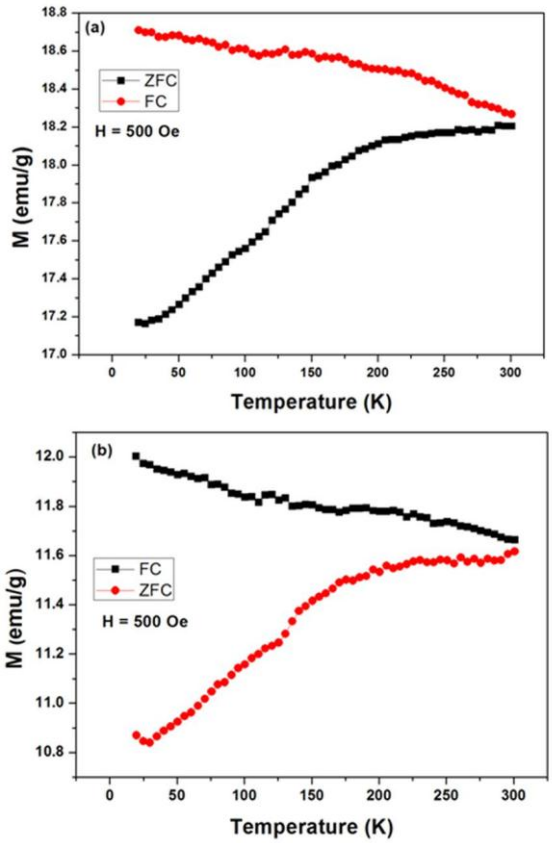

Fig.5.12. *FC-ZFC plots of Ni-NiOnanocomposites synthesized with graphite, graphene and precursor salt of Ni/NiO (a) Ni-NiO-GT (b) Ni-NiO-GE under external field of 500 Oe.*

There is no appreciable change in magnetization of both samples under filed cooling (FC) condition with respect to temperature. On the other hand magnetization of both samples decreases with the decrease of temperature under zero field cooling condition (ZFC). FC and ZFC curves are not meeting below room temperature. FC and ZFC magnetization of Ni-NiO-GT at 20 K is higher than that of Ni-NiO-GE.

5.4. Conclusions

Nickel rich Ni/NiOnanocomposites embedded in graphite and graphene matrices can be synthesized using solution combustion method. Raman band seen at about 1336 cm^{-1} (D band) and at about 1577 cm^{-1} (G band) in the both the samplesalong with the IR spectral data indicates the formation of Ni/NiO/graphite and Ni/NiO/graphenenanocomposite systems. XPS analysis shows the presence of nickel, oxygen and carbon as major elements in Ni/NiOnanocompositecarbonaceous systems. The*d.c* conductivity measurement reveals that Ni/NiO embedded in graphite matrix has relatively larger value of conductivity when compared to Ni/NiO embedded in graphene matrix due to more crystallinity of graphite. Sunlight assisted photodegradation efficiency of Ni/NiO embedded in graphene is more than that of Ni/NiO embedded in graphite, probably due to relatively higher surface area of graphene with respect to graphite. Room temperature coercivity of Ni/NiO embedded in graphite matrix is 118 Oe, which is higher than that of Ni/NiO embedded in graphene, attributed to the wrapping of magnetic moments of Ni by the graphite layers.

.....ൟ.....

magnetic properties. Some of the metallic-carbon materials are exhibiting catalytic properties in the presence of light. Fang *et al* reported photocatalytic hydrogen evolution properties of nickel nanoparticles coated with graphene layers [Fang *et al*; 2017]. Zirconium doped nickel cobalt ferrite-graphene nanocomposite is used as visible light based photocatalyst [Rasheed *et al*; 2016]. Nickel-ferrite-graphene, graphene/Ni/TiO_2/CNT composites are photocatalytic materials [Zhao *et al*; 2014, Hui *et al*; 2014]. Apart from this nickel based carbonaceous materials are showing morphology dependent magnetic properties. Ji *et al* synthesized reduced graphene oxide/Ni nanocomposites and studied its magnetic properties [Ji *et al*; 2012]. Thin film nanocomposites of nickel nanoparticles homogenously embedded in the amorphous carbon matrix shows superparamagnetic behavior and its blocking temperature is about ~13 K [Fonseca *et al*; 2005].

NiO/reduced graphene oxide nanocomposites can be synthesized by ball milling of bulk nickel and graphite [Kahimbi *et al*; 2017]. Carbon nanoparticles encapsulated in hollow nickel oxide were synthesized using hydrothermal method [Fan *et al*; 2012], Ni-activated carbon nanocomposites prepared through electroless deposition [Figueroa-Torres *et al*; 2012], nickel-graphene composites by electrochemical deposition [Ren *et al*; 2015], graphene/NiO nanorod composites using solvothermal method [Zahraei *et al*; 2015] and hybrid NiO/Ni/graphene nanocomposite prepared by an electrical wire explosion process [Lee *et al*; 2014] etc. Zhou *et al* prepared Ni/graphene composite from the precursors graphene oxide gel and nickel acetate [Zhou *et al*; 2016]. Mansour *et al* reported carbon/nickel nanocomposites prepared by sol-gel method [Mansour *et al*; 2015]. Out of these methods, solution combustion method can give good yield and very

simple procedure is required to carry out the synthesis. In this chapter we are describing this simple method for the synthesis of Ni rich Ni-NiO nanocomposites with graphite/graphene as matrix and its electric, photocatalytic and magnetic properties.

5.2. Experimental

5.2.1 Synthesis

All the reagents used for the synthesis were of AR grade and obtained from Spectro chem Pvt Ltd. Mumbai, India. Graphite/Ni-NiO nanocomposites (Ni-NiO-GT) was prepared from precursor solutions made by dissolving 6 g of nickel acetate, 12 g of citric acid in 20 ml of water separately and then adding 0.9 g of graphite powder. All these reactants were transferred to a 1000 ml beaker and stirred well. To this, 30 ml of HNO_3 was poured, ammonia solution was added to the above solution to adjust the pH to 7. The beaker was then placed on a preheated hot plate, nearly for one hour to occur the combustion reaction. Ash like powder was obtained after the combustion process, collected samples were ultrasonicated using isopropanol for 3 hour and dried. Graphene added Ni-NiO nanocomposites (Ni-NiO-GE) was synthesized by adding graphene instead of graphite with above mentioned protocol.

5.2.2 Characterization

XRD analysis of the samples were performed using PANALYTICAL XPERT-PRO X-ray diffractometer with CuKα radiation (1.5404 Å). Fourier Transform Infra Red spectroscopy (FTIR) of the samples were done with JASCO FTIR 4100 spectrometer with KBr pellet

method in the range 400-4000 cm^{-1}. A Horiba Jobin Yvon LabRAM HR system (resolution of the order of $3cm^{-1}$) equipped with He-Ne laser (632.8 nm) were used for the Raman spectral recording. TEM and HRTEM measurements were performed with a JEOL JEM 2100 model High Resolution Transmission Electron Microscope (HRTEM) operated at 200 KeV equipped with EDAX and SAED detector. Morphology of the samples was examined by using Carl Zeiss, sigma HV model Field emission scanning electron microscope (FE-SEM). ElementarVario EL III C-H-N analyser was used to know the presence of carbon, hydrogen, nitrogen in the samples. Thermal analysis of the samples was carried out with Perkin Elmer, Diamond TGA. X-ray photoelectron spectroscopy (XPS) analysis of the samples were performed by using Kratos AXIS Ultra spectrometer with AlKα radiation. *d.c* electrical conductivity measurement of the samples under study was carried out using Keithley model 2400 source meter automated with Lab-VIEW software. Photocatalytic studies were carried out by measuring the absorbance of the methelyne blue (MB) dye using UV-VIS-NIR spectrometer (JASCO-V-570). Magnetic properties of the samples were taken with Lakeshore make Model 7410 Vibrating Sample Magnetometer (VSM).

5.2.3 Photodegradation studies

Photodegradation properties of the samples were measured by using MB as a test solution. 0.025 mM MB solution was prepared and taken into borosil bottles (5 ml volume capacity). Catalyst loading was fixed to 5 g/L and the bottles were placed under direct sun light for the photocatalytic experiments. Absorption measurements of remnant MB solution were

performed with UV-VIS-NIR spectrometer after each one hour exposure to solar radiation.

5.3. Results and discussion

5.3.1. X-ray diffraction analysis

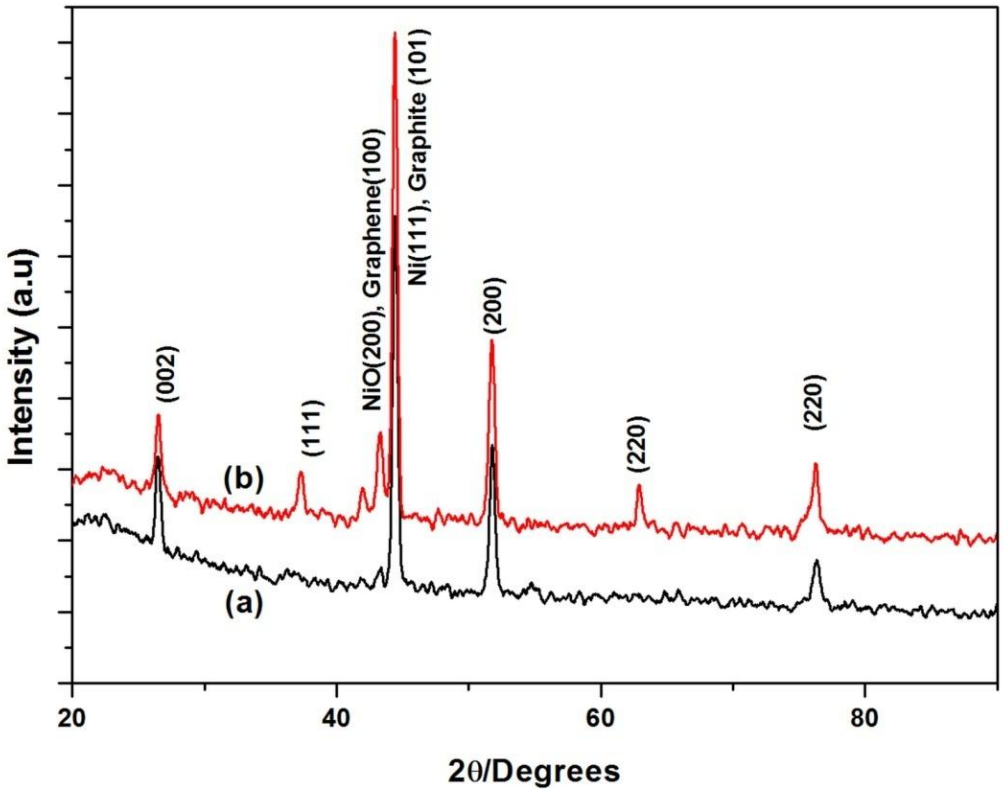

***Fig. 5.1**. X-ray diffraction patterns of Ni-NiO nanocomposites synthesized with graphite, graphene and precursor salt of Ni/NiO (a) Ni-NiO-GT (b) Ni-NiO-GE.*

XRD pattern of Ni-NiO-GT has diffraction peaks almost similar to Ni rich Ni-NiO nano composite discussed previously (chapter 3). In addition to Ni diffraction peaks, a diffraction peak is seen at 2θ value of 26.5^0 assigned to graphite (002) (Fig.5.1). XRD pattern of Ni-NiO-GE is

having diffraction peaks correspond to NiO at 2θ value 37.4^0 (111), 43.3^0 (200), 62.7^0 (220) and Ni at 2θ value of 44.5^0 (111), 51.8^0 (200), 76.5^0 (220) along with graphene at 26.5^0 (002). Unambiguous assignment of diffraction peaks at 44.4^0 and 43.3^0 of Ni-NiO-GT and Ni-NiO-GE respectively is limited since diffraction from planes (111) of Ni, (101) of graphite, (200) of NiO and (100) of graphene are expected in this position. Reference intensity ratio method (RIR) is used to calculate the weight percentages of Ni and NiO in both the samples [Hubbard *et al*; 1988]. In Ni-NiO- GT, the weight percentages of Ni and NiO are 64 and 36 % where as Ni-NiO-GE has 54 and 46 % of Ni and NiO respectively. From this one can conclude that NiO weight percentage is relatively higher in Ni-NiO-GE compared to Ni-NiO-GT. Average grain size of Ni in Ni-NiO-GT and Ni-NiO-GE calculated using Scherrer's formula [Cullity; 1956] based on the strongest diffraction peak of Ni at 2θ value of 44.4^0 is 23 and 22 nm . These values are less than the grain size obtained for Ni (38 nm) embedded in amorphous carbon matrix discussed previously (chapter 3). The presence of graphite and graphene in both crystal growth systems may hinder the agglomeration of Ni nanoparticles into relatively smaller one. This in turn contributes to reduction in size of Ni in Ni-NiO-GT and Ni-NiO-GE with respect to Ni in amorphous carbon matrix.

5.3.2. Fourier transform infrared (FTIR) and Raman vibrational spectroscopy analysis

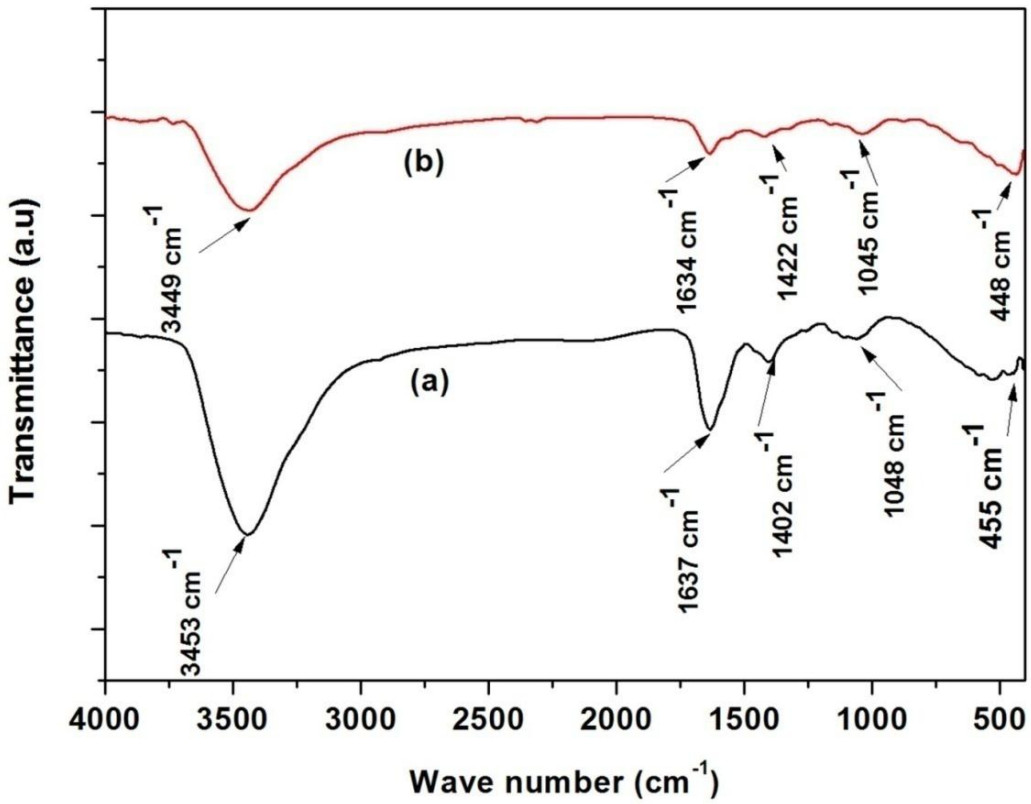

Fig. 5.2.*FTIR spectra of Ni-NiO nanocomposites synthesized with graphite, graphene and precursor salt of Ni/NiO (a) Ni-NiO-GT (b) Ni-NiO-GE.*

Table 5.1 gives the details of Raman and FTIR bands observed for Ni-NiO-GT and Ni-NiO-GE respectively. Ni-NiO-GT is having weak bands at 189 and 495 cm^{-1} in the Raman spectra contributed to NiO vibrations and the values are close to the previous report [Patange *et al*; 2015]. But in the IR spectra, a weak band is seen at 445 (Ni-NiO-GT) and 448 cm^{-1} (Ni-NiO-GE) are due O-Ni-O stretching vibrations in conformity with XRD of Ni-NiO-GT and Ni-NiO-GE where diffraction peaks related to NiO is present

(Fig. 5.2). The observed bands are close to the earlier reports [Rahdar *et al*; 2015, Yousefi *et al*; 2016]. The absence of Raman band related to NiO in Ni-NiO-GE is probably due to the presence of light absorbing graphene environment.

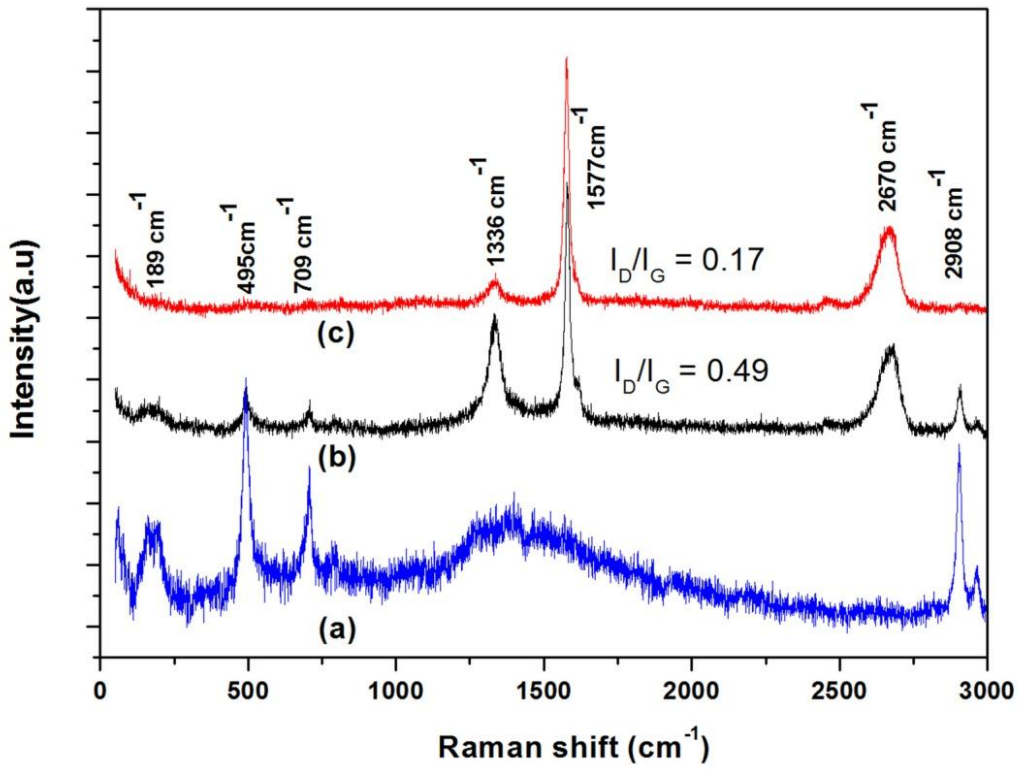

Fig. 5.3.*Raman spectra of Ni-NiO nanocomposites synthesized with graphite, graphene and precursor salt of Ni/NiO (a) Ni rich Ni-NiO (b) Ni-NiO-GT (c) Ni-NiO-GE.*

Table 5.1 *FTIR and Raman data of Ni-NiO nanocomposites synthesized with graphite, graphene and precursor salt of Ni/NiO (cm^{-1}).*

Ni-NiO-GT		**Ni-NiO-GE**		**Assignments**
FT-IR	Raman	FT-IR	Raman	
	189 vw			Lattice mode
445 w		448 w		νNiO
	495 w			νNi-O (1LO mode)
	709 vw			2TO of NiO
1048 w				νC-O
	1336 s		1336 w	D band
1402 w				C-OH bending vibrations
	1577 vvs		1577 vvs	G band
1637 s		1634 s		OH bending vibration or νC=C
	2670 s		2670 s	2D band
	2908 w			D+G band
3453 vs		3449 vs		νO-H

The presence of Raman peaks in Ni-NiO-GT is due to higher order distortion of NiO_6 octahedra. A very weak band located at 709 cm^{-1} is due to 2TO mode of NiO. Weak FTIR band observed at 1048 in Ni-NiO-GT is due to carbon and oxygen related impurities [Fu *et al*; 2014]. The characteristic peaks of graphite and graphene is evidenced by the presence of D and G bands and their harmonics in the Raman spectra. Raman band seen at 1336 cm^{-1} in the both samples is attributed to sp^3 hybridized D band, strong Raman bands at 1577 cm^{-1} in the both the sample are attributed to G band (Fig.5.3). A few weak bands are also seen in the IR spectra of the both the samples (table 5.1). Raman spectra of Ni-NiO-GT is having a band at 2908 cm^{-1}, which is a combination of D and G band. Some of the adsorbed hydroxyl group (OH) may produce C-OH vibrations at 1400 cm^{-1} [Peng *et al*; 2013,Trapalis *et al*; 2016]. In the present case this band is weak and observed at 1402 cm^{-1} in Ni-NiO-GT. Strong IR band seen at 1634-1637 cm^{-1} region may be ascribed to OH bending vibrations of water or C=C vibrations of graphite and graphene structure [Trapalis *et al*; 2016]. The I_D/I_G value of Ni-NiO-GT is 0.49 which is higher than that of Ni-NiO-GE (0.17). It can be understood from this observation that, defect levels of carbon is more in Ni-NiO-GT than Ni-NiO-GE, indicate that carbon present in Ni-NiO-GE is more crystalline than Ni-NiO-GT.

5.3.3. TEM, HRTEM, SAED analysis

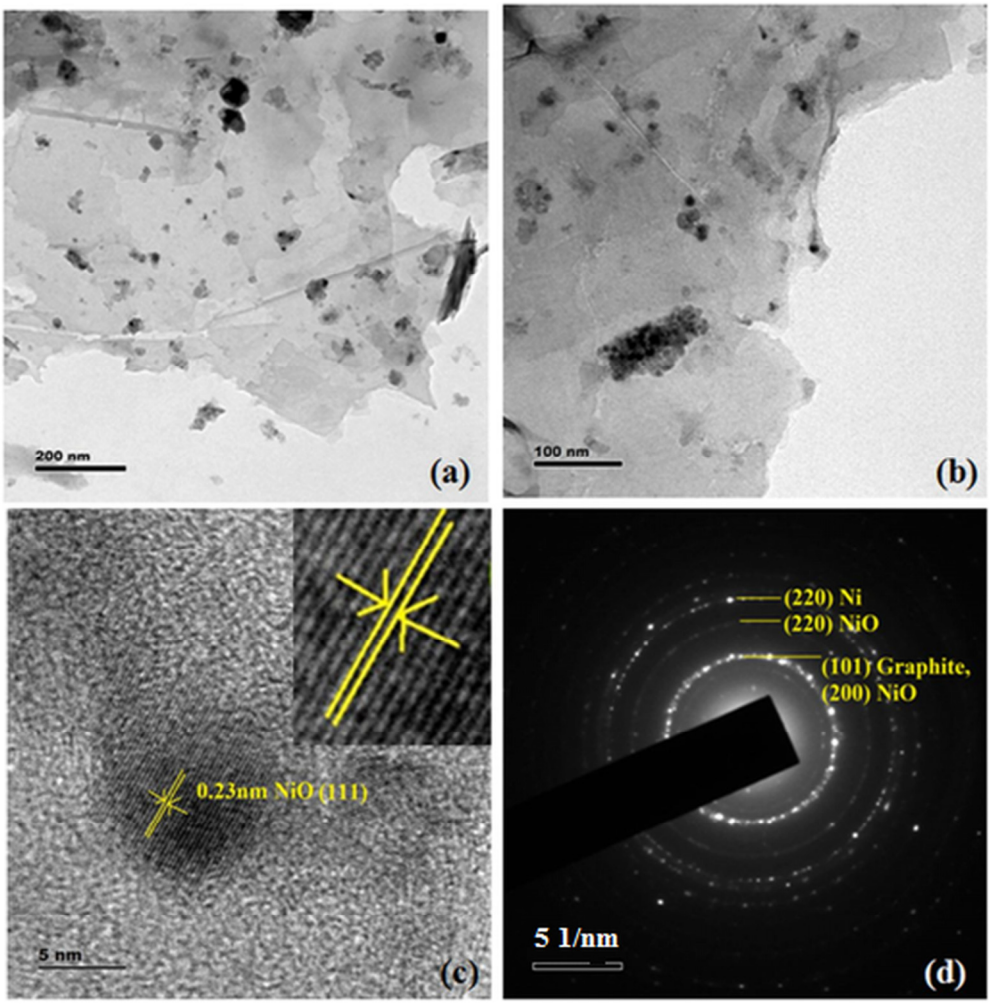

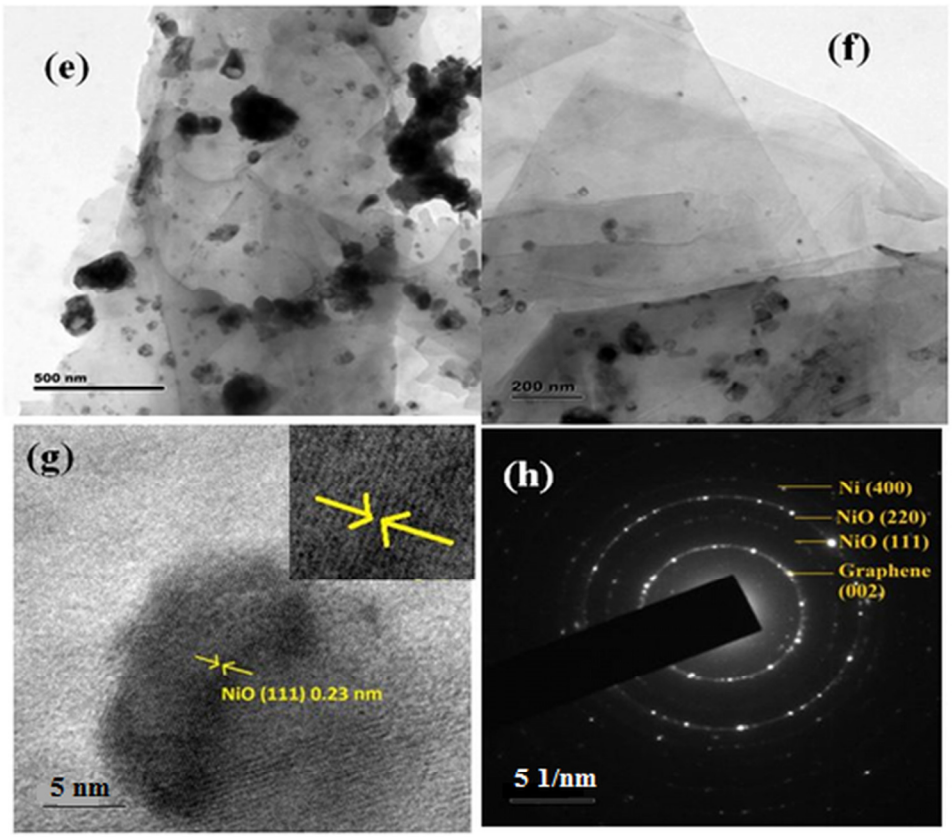

Fig. 5.4.*TEM images of Ni-NiOnanocomposites synthesized with graphite, graphene and precursor salt of Ni/NiO (a) & (b) TEM images at different resolutions of Ni-NiO-GT (c) HR-TEM image of Ni-NiO-GT (d) SAED pattern of Ni-NiO-GT, (e) &(f) TEM images at different resolutions of Ni-NiO-GE (g) HR-TEM image of Ni-NiO-GE (h) SAED pattern of Ni-NiO-GE.*

TEM images show that metallic Ni/NiO nanoparticles are dispersed in graphitic system (Fig. 5.4 (a) and (b)). These particles are seen to be agglomerated due to the local sintering attributed to the instantaneous high reaction temperature of solution during combustion process. In the case of Ni-NiO-GE, Ni-NiO nanoparticles are embedded in graphene layer and are agglomerated (Fig. 5.4 (e) and (f)). From the HR-TEM of Ni-NiO-GT sample the inter planar spacing is calculated to be 0.23 nm and it

corresponds to the plane (111) of NiO. SAED pattern of Ni-NiO-GT shows diffraction rings from the planes (200), (220) of NiO and (220) plane of Ni. In Ni-NiO-GT, diffraction ring corresponds to (101) plane is due to graphite (Fig.5.4 (d)). HR-TEM of Ni-NiO-GE shows inter planar spacing of 0.23 nm of NiO (111) plane (Fig. 5.4 (g)). SAED pattern of Ni-NiO-GE gives diffraction rings due to NiO (111), (220) planes and to Ni from the plane (400). Diffraction ring from (002) plane of graphene is also observed from this sample.

5.3.4. EDAX analysis

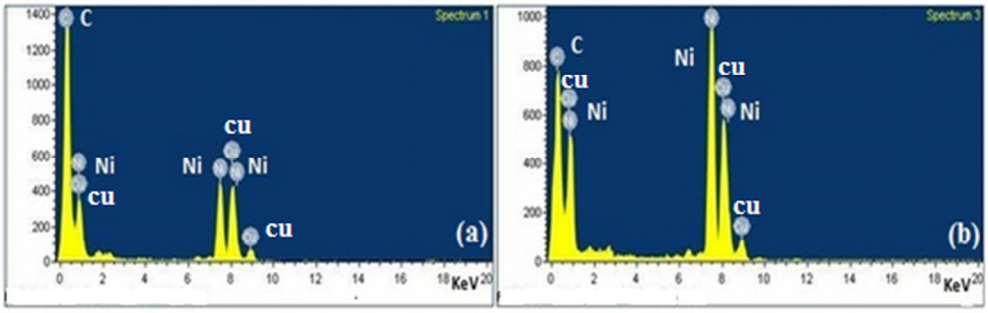

Fig. 5.5.*EDAX spectra of Ni-NiO nanocomposites synthesized with graphite, graphene and precursor salt of Ni/NiO (a) Ni-NiO-GT (b) Ni-NiO-GE.*

EDAX gives that, carbon atomic percentage is 72.67 % and that of Ni is about 13.34 % in Ni-NiO-GT. Ni-NiO-GE has carbon atomic percentage about 40 % and Ni is 37.52 %. From the EDAX analysis oxygen is not seen which suggest that Ni-NiO-GT and Ni-NiO-GE is mainly consists of Ni as a major content (Fig. 5.5). CHN analysis of Ni-NiO-GT gives 17.85 % carbon where as 14.88 % in the Ni-NiO-GE sample.

5.3.5. FESEM analysis

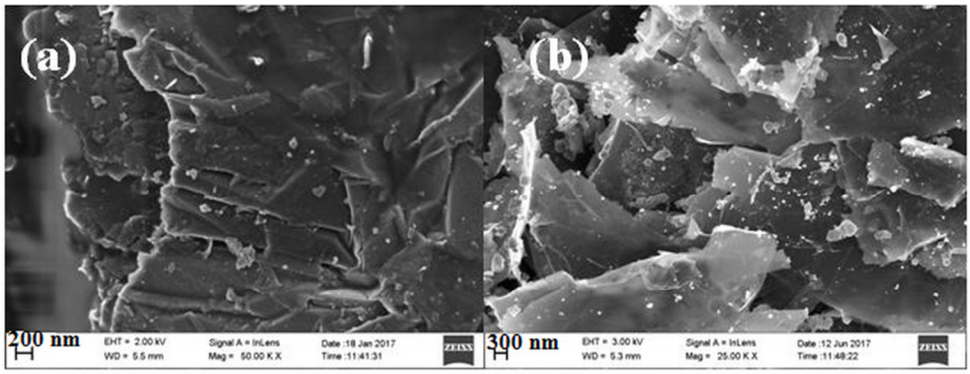

Fig.5.6. *FE-SEM images of Ni-NiO nanocomposites synthesized with graphite, graphene and precursor salt of Ni/NiO (a) Ni-NiO-GT (b) Ni-NiO-GE.*

In figure 5.6 (a) multilayer of graphite is found in the sample, Ni/NiO nanoparticles are dispersed on the graphite sheets. Figure 5.6 (b) shows that graphene layers are intermixed with Ni/NiO nanoparticles. In the present case graphite or graphene act as supporting matrix which likely to protect Ni/NiO nanoparticles from surrounding environment.

5.3.6. TGA analysis

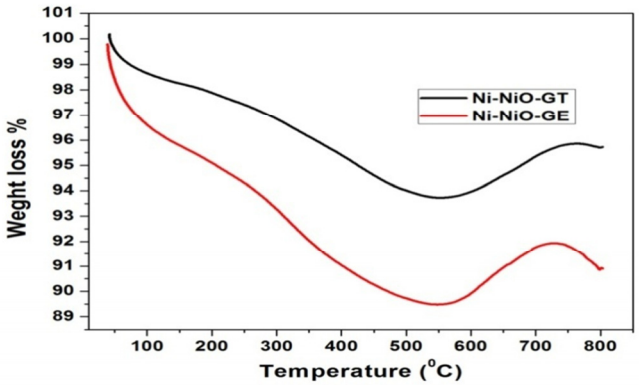

Fig.5.7. *TGA of Ni/NiO nanocomposites synthesized with graphite, graphene and precursor salt of Ni/NiO (a) Ni-NiO-GT (b) Ni-NiO-GE.*

Thermal stability and oxidation process of the samples are evaluated with TGA. Figure 5.7 shows TGA of Ni-NiO-GT and Ni-NiO-GE respectively. About 2% (±1.5) weight loss is observed for both Ni-NiO-GT and Ni-NiO-GE in the temperature range 40 to 100^0C (for Ni-NiO-GT) and 40 to 150^0C (for Ni-NiO-GE). After this, there is steady decrease of weight loss of sample in the case of Ni-NiO-GT. About 6.2 % weight is lost in the temperature interval from 150 to 550^o C. For the sample Ni-NiO-GE this weight loss is 10.5 %. This may be due to the conversion of carbon present in the sample in the form of graphite and graphene into carbon dioxide. There after weight gain observed from temperature 550 to 800^oC forming peak around 750^o C indicating the conversion of Ni to NiO.

XPS analysis reveals the presence of Ni, O, C which is consistent with the previously studied characterization tools (Fig. 5.8). In the case of Ni-NiO-GT, the peak seen at 855.99 eV and 861.42 eV (satellite) is attributed to $Ni2p_{3/2}$ of NiO [Tian *et al*; 2012]. Relatively weak peak is observed at 853.65 eV due to the presence of metallic nickel (Fig. 5.8(a)). Almost similar observations are found in the case of Ni-NiO-GE with slight differences in binding energies (Fig. 5.8(b)). Two peaks are obtained in the region 529 to 532 eV from both the samples, corresponds to O1s. The peak observed at ~529 eV in the samples Ni-NiO-GT and Ni-NiO-GE is attributed to NiO [Liu *et al*; 2015]. The peak seen at ~531 eV in both the samples is due to carbon and oxygen related bonds [Liu *et al*; 2015]. C1s peak of Ni-NiO-GT is observed at 284.76 eV, this peak is shifted to 279.26 eV in Ni-NiO-GE.

5.3.7. XPS analysis

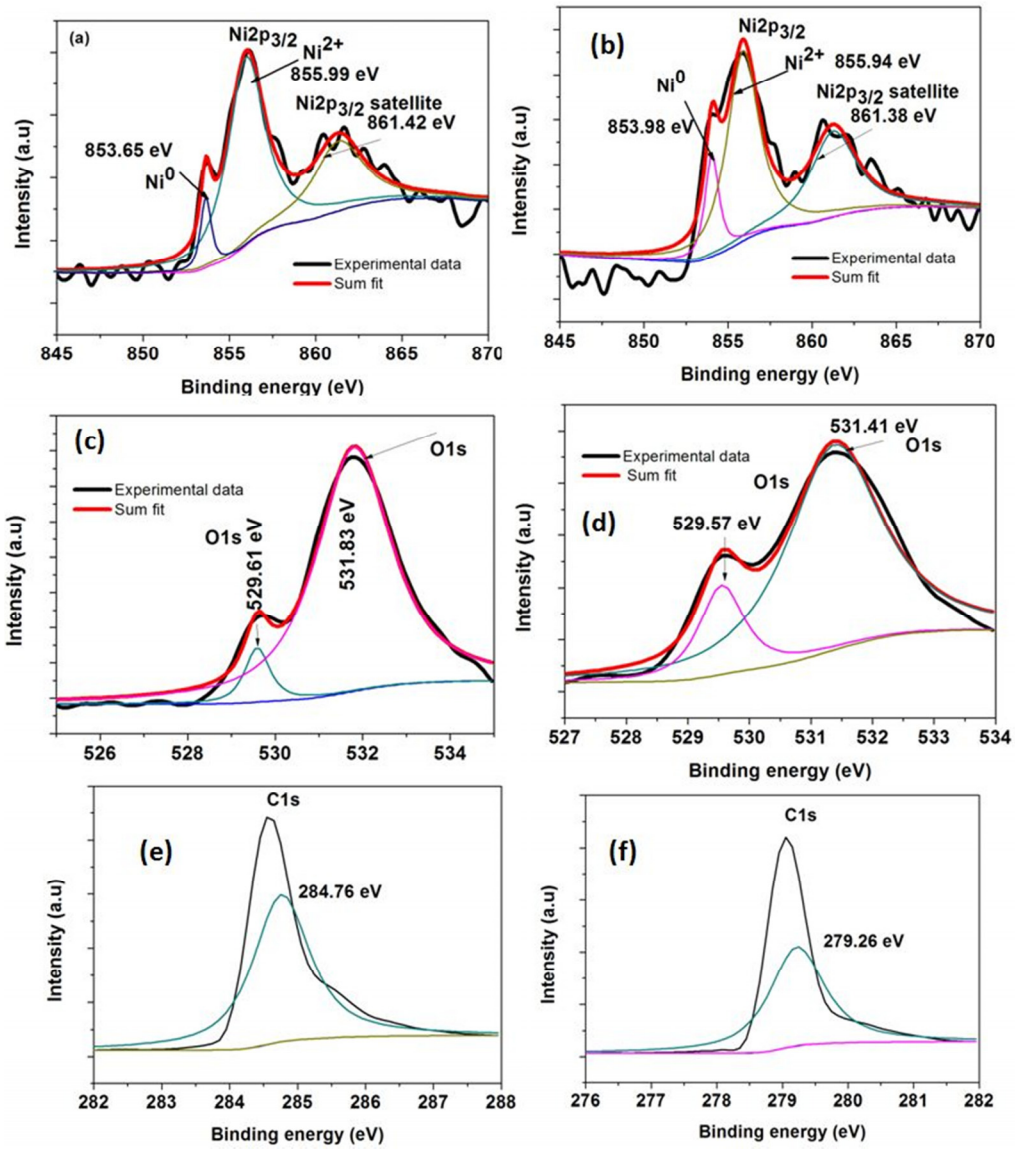

Fig.5.8. *XPS spectra of Ni/NiO nanocomposites synthesized with graphite, graphene and precursor salt of Ni/NiO (a) Ni2p of Ni-NiO-GT (b) Ni2p of Ni-NiO-GE (c) O1s of Ni-NiO-GT (d) O1s of N-NiO-GE (e) and (f) are C1s of Ni-NiO-GT and Ni-NiO-GE respectively.*

5.3.8. Electrical properties

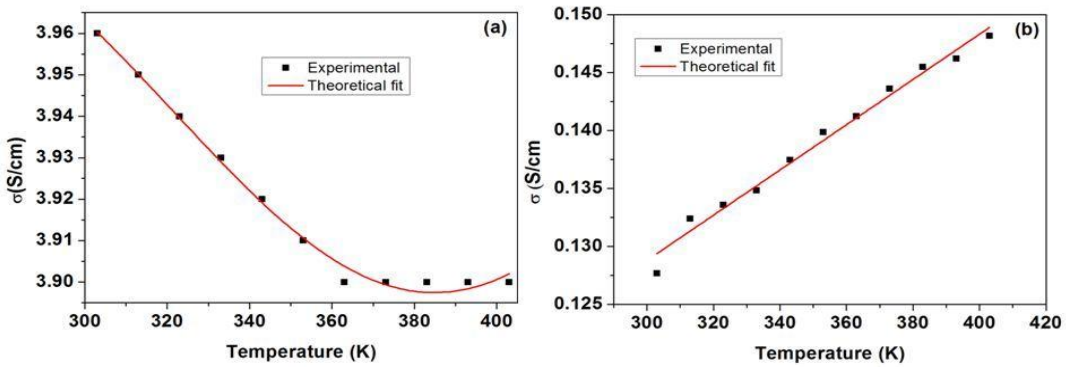

Fig.5.9. *d.c conductivity plots of Ni-NiO nanocomposites synthesized with graphite, graphene and precursor salt of Ni/NiO (a) Ni-NiO-GT (b) Ni-NiO-GE.*

Figure 5.9 shows the *d.c* conductivity plots of Ni-NiO-GT and Ni-NiO-GE. The *d.c* conductivity values of Ni-NiO-GT and Ni-NiO-GE are relatively less than Ni rich Ni-NiO which has a value of 24 S/cm (chapter 4). Ni-NiO-GT shows metallic behavior, in which conductivity decreases with increase in temperature and its room temperature *d.c* conductivity is 3.96 S/cm. But Ni-NiO-GE behaves like semiconductor and its conductivity is 0.13 S/cm at 300 K. Ni weight percentage is more in Ni-NiO-GT as understood from the XRD result. NiO content is more in Ni-NiO-GE from the XRD calculated by RIR method described previously. More Ni content in Ni-NiO-GT is responsible for the increases in conductivity as well as metallic conducting nature to the sample. Relatively higher amount of semiconducting NiO content in Ni-NiO-GE decreases the conductivity and the material behaves like semiconductor. From the Raman analysis the carbon present in Ni-NiO-GE is more crystalline than in Ni-NiO-GT. This increase in crystallinity of carbon causes the increase in number of grain boundaries. Electrons likely to scatter at the grain boundaries which decreases the conductivity of the sample.

5.3.9. Photocatalysis studies

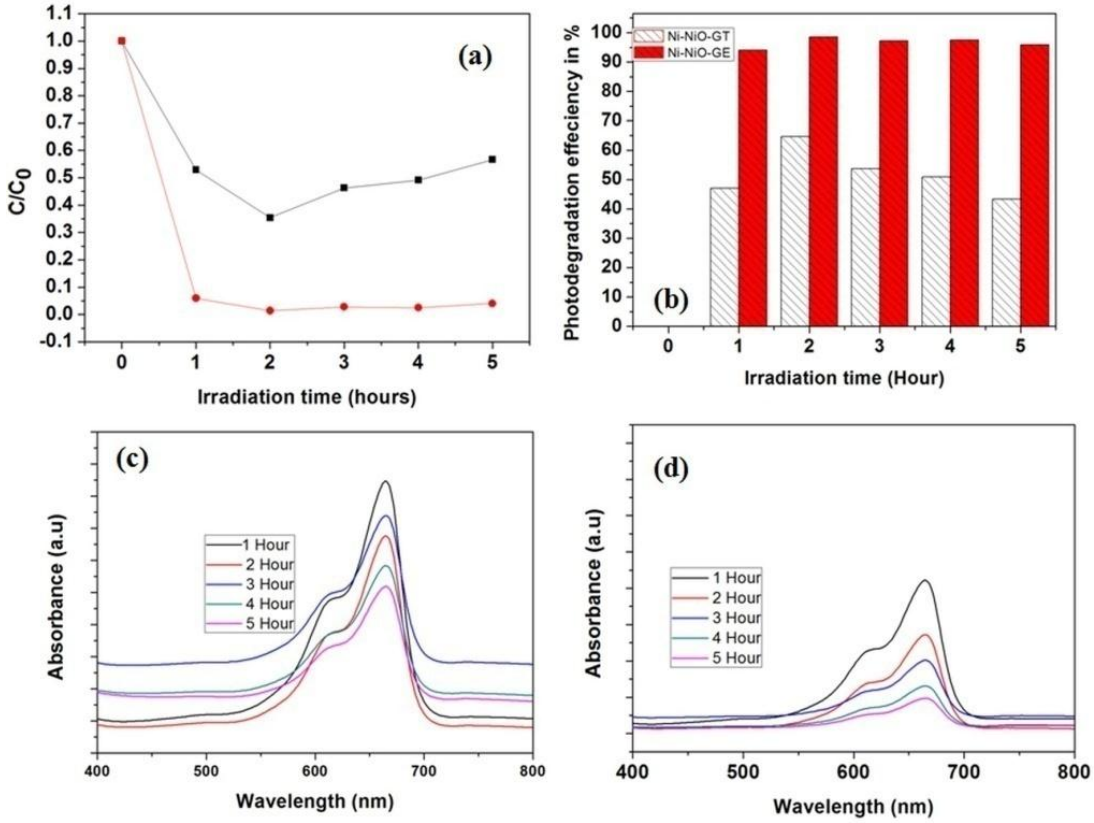

Fig.5.10. *Photodegradation characteristics of Ni-NiO nanocomposites synthesized with graphite, graphene and precursor salt of Ni/NiO under sun light exposure by taking methylene blue as model system (a) C/C_0 plot of Ni-NiO-GT and Ni-NiO-GE (b) photodegradation efficiency of Ni-NiO-GT and Ni-NiO-GE (c) absorbance spectra of MB at different time durations with Ni-NiO-GT as photocatalyst (d) absorbance spectra of MB at different time durations with Ni-NiO-GE as photocatalyst.*

Figure 5.10 present the photodegradation characteristics of Ni-NiO-GT and Ni-NiO-GE under sun light exposure with MB solution as model dye system. Ni-NiO-GT shows about 43 % photodegradation efficiency while Ni-NiO-GE shows 96 % after five hours of sunlight irradiation. Photodegradation efficiency of both Ni-NiO-GT and Ni-NiO-GE is less

than Ni rich Ni-NiO under the same condition (chapter 4). Among the two samples, Ni-NiO-GT has about 64 % nickel content while Ni-NiO-GE with 54 %. Photocatalytic property of Ni-NiO is mediated by the activation of surface plasmon resonance of nickel nanoparticles (chapter 4). Hence sample with higher content of nickel is likely to show more photocatalytic efficiency. But in the present case, Ni-NiO-GE with less content of nickel with respect to Ni-NiO-GT shows higher photodegradation efficiency. The enhanced photocatalytic efficiency of Ni-NiO-GE is probably associated with combined effect of nickel and graphene system since graphene posses relatively more surface area than that of graphite [Jain *et al*; 2014].

5.3.10. Magnetic properties

5.3.10.1. Field dependent magnetization (M-H)

Table 5. 2 *Magnetic properties of Ni-NiO nanocomposites synthesized with graphite, graphene and precursor salt of Ni/NiO.*

Sample	20 K			200 K			300 K		
	M_S (emu/g)	M_r (emu/g)	H_C (Oe)	M_S (emu/g)	M_r (emu/g)	H_C (Oe)	M_S (emu/g)	M_r (emu/g)	H_C (Oe)
Ni-NiO-GT	50	6	139	47	5	113	33	5	118
Ni-NiO-GE	32	3.5	125	31	2.5	96	34	2.2	78

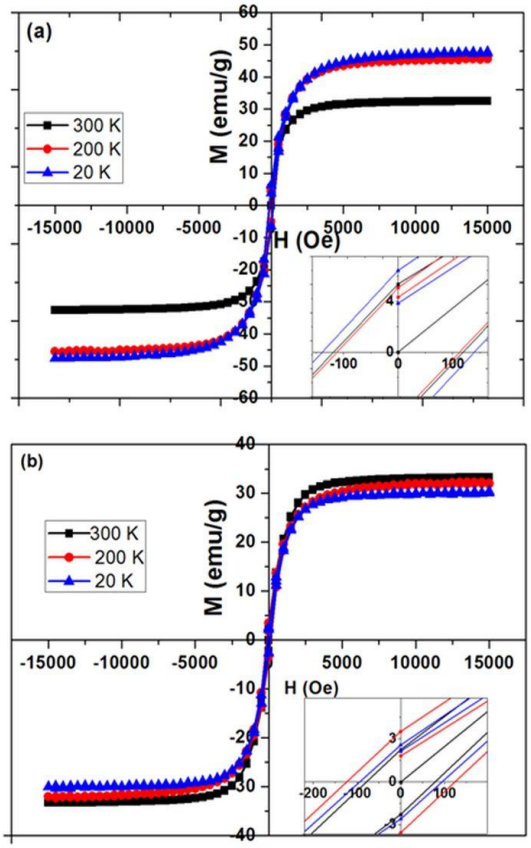

Fig.5.11. *M-H characteristics of Ni-NiO nanocomposites synthesized with graphite, graphene and precursor salt of Ni/NiO at different temperatures (a) Ni-NiO-GT (b) Ni-NiO-GE.*

Figure 5.11 shows the M-H characteristics of Ni-NiO nanocomposites with graphite and graphene synthesized by solution combustion method. From the Fig. 5.11 it can be observed that all the samples behave like ferromagnetic material at 20, 200, 300 K. In the case of Ni-NiO-GT saturation magnetization (M_s) is obtained as 50 emu/g (20 K). Saturation magnetization decreases with respect to increase of temperature which shows a value of 33 emu/g at 300 K (table 5.2). There is no appreciable change in value of remanant magnetization of Ni-NiO-GT with respect to temperature. Magnetic coercivity of Ni-NiO-GT is 139, 113, 118 Oe respectively at 20, 200, 300 K. It is interesting to note that magnetic

coercivity of Ni-NiO-GT is higher than that of Ni rich Ni-NiO (~80 Oe) discussed previously (chapter 3). Figure 5.11(b) presents the M-H behavior of Ni-NiO-GE at 20, 200, 300 K. Variation of M_s and M_r is feeble with respect to increases in temperature. H_c of this sample at 20 K is 125 Oe, which decreases with respect to temperature. Room temperature coercivity is 78 Oe which is less than that of Ni rich Ni-NiO (chapter 3).

5.3.10.2. Temperature dependent magnetization (M-T)

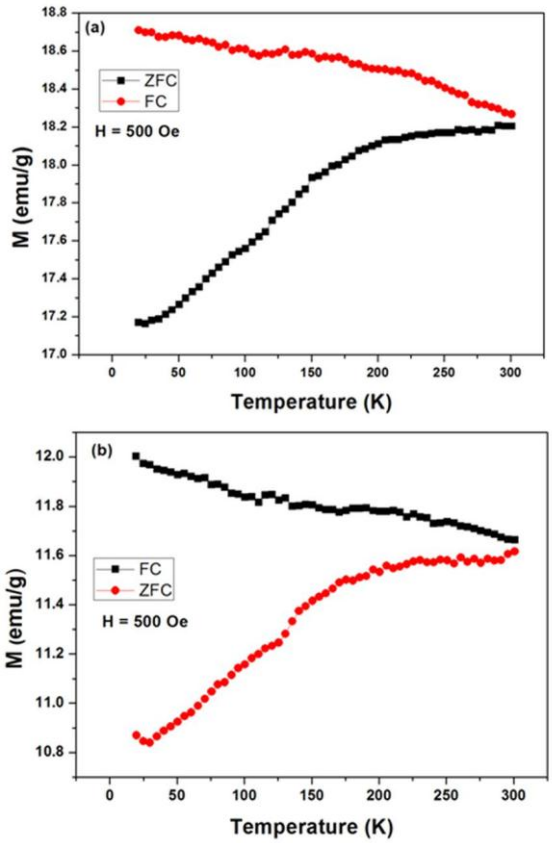

Fig.5.12. *FC-ZFC plots of Ni-NiO nanocomposites synthesized with graphite, graphene and precursor salt of Ni/NiO (a) Ni-NiO-GT (b) Ni-NiO-GE under external field of 500 Oe.*

There is no appreciable change in magnetization of both samples under filed cooling (FC) condition with respect to temperature. On the other hand magnetization of both samples decreases with the decrease of temperature under zero field cooling condition (ZFC). FC and ZFC curves are not meeting below room temperature. FC and ZFC magnetization of Ni-NiO-GT at 20 K is higher than that of Ni-NiO-GE.

5.4. Conclusions

Nickel rich Ni/NiO nanocomposites embedded in graphite and graphene matrices can be synthesized using solution combustion method. Raman band seen at about 1336 cm^{-1} (D band) and at about 1577 cm^{-1} (G band) in the both the samples along with the IR spectral data indicates the formation of Ni/NiO/graphite and Ni/NiO/graphene nanocomposite systems. XPS analysis shows the presence of nickel, oxygen and carbon as major elements in Ni/NiO nanocomposite carbonaceous systems. The *d.c* conductivity measurement reveals that Ni/NiO embedded in graphite matrix has relatively larger value of conductivity when compared to Ni/NiO embedded in graphene matrix due to more crystallinity of graphite. Sunlight assisted photodegradation efficiency of Ni/NiO embedded in graphene is more than that of Ni/NiO embedded in graphite, probably due to relatively higher surface area of graphene with respect to graphite. Room temperature coercivity of Ni/NiO embedded in graphite matrix is 118 Oe, which is higher than that of Ni/NiO embedded in graphene, attributed to the wrapping of magnetic moments of Ni by the graphite layers.

.....ൠ.....

Chapter-6

Contents

Photocatalytic and Magnetic Studies of Ni-NiO/MWCNT Nanocomposites

6.1 Introduction

Nanostructured metallic nickel particles and NiO nanoparticles are widely used as magnetic, photocatalytic, supercapacitors and additives in oils [Wu *et al*; 2012, Qiu *et al*; 2001]. Majority of metallic nanoparticles are prone to oxidation which may limit its applications, especially in air ambient. The metallic nanoparticles can be protected by embedding them in matrices like carbon, silicon, alumina etc. Carbon nano tubes (CNT) posses unique electronic, mechanical, chemical properties and is useful in dispersion and stabilization of metal/semiconductor nanoparticles [Georgakilas *et al*; 2007]. Decoration of CNT with nanoparticles has attracted the attention of researchers due to their additional functionalities that can be imparted to CNTs. Such process could give good dispersion of CNTs in solvents and enhance their optical, electric and magnetic properties [Kim *et al*; 2003, Chin *et al*; 2004, Watts *et al*; 2002, Wu *et al*; 2002]. Metal-CNTs are useful in microelectronic devices and in CNT-metal matrix composites that can enhance tribological properties [Unger *et al*; 2003, Chen *et al*; 2006]. Recently, MWCNT/Ag nanocomposites have been used for the detection of methelyne blue dye in water [Dinh *et al*; 2016]. Among the metal-CNT nanocomposites Ni/CNT nanocomposites are used as electrochemical sensor and hydrogen storage material [Adekunle *et al*;

2010, Lin *et al*; 2010,Kim *et al*; 2005]. Nickel oxide is fundamentally studied because of its applications in catalysis, pseudocapacitors, gas sensors, electrochromic coatings etc. [Goncharova *et al*; 1980, Justin *et al*; 2010, Luyo *et al*; 2009, Lin *et al*; 2008]. Also metal oxide/CNT nanocomposites have attracted a lot of interest due to their physical, chemical, electrical and thermal properties. Recently, multiwalled carbon nanotubes (MWCNT) are widely investigated because of its conducting properties and mechanical stability. NiO/MWCNT nanocomposites have been used for the removal of Pb^{2+} ions from aqueous solution, lithium storage and electrochemical detection of riboflavin [Diva *et al*; 2017, Xu *et al*; 2011, Kumar *et al*; 2014]. A combination of metal and metal oxide/CNT nanocomposites may be an attractive material but there are only a few reports on it. Nickel based carbon systems such as nickel species/CNT (including Ni and NiO) nanocomposites can be prepared through atomic layer deposition [Choi *et al*; 2015], successive ionic layer adsorption and reaction (SILAR) method [Gund *et al*; 2014], chemical method [Sahebian *et al*; 2016], coprecipitation [Diva *et al*; 2017], thermal decomposition [Xu *et al*; 2011], chemical evaporation [Masipa *et al*; 2013] etc. In this chapter, we are presenting the synthesis of nickel rich Ni/NiO/MWCNT nanocomposites with CNT and precursor salt for the Ni/NiO with solution combustion method. Its electric, photocatalytic and magnetic properties are also investigated.

6.2. Experimental

6.2.1 Synthesis

Nickel rich Ni-NiO/MWCNT nanocomposites was synthesized using solution combustion method. 6 g of nickel acetate (oxidizer) and 12 g of citric acid (fuel) were initially dissolved in water separately, stirred for 15 minutes and mixed together. In this solution, 30 ml of $HNO_3$and corresponding quantity of NH_3 solution was added until the whole solution became neutral. 0.9 g of MWCNT was added to this solution, which is equivalent to 15 % of nickel acetate. The resulting solution was heated by heater which was then subjected to combustion process. Final products were collected and washed with water several times. The washed sample was then poured into isopropanol and ultrasonicated for 3 hours time duration. Finally, the sample was filtered and dried. The sample is named as Ni-NiO-MWCNT.

6.2.2 Characterization

Analytical characterization of these materials were done using the equipments described in chapter 3. Magnetic properties of the sample were studied using Lakeshore make model 7410 Vibrating Sample Magnetometer (VSM).

6.2.3 Photodegradation studies

Initially 0.025 mM methelyne blue (MB) solution was prepared from the 1M MB stock solution. This was then transferred in to 5 ml capacity borosil bottles. The sample was poured in to these bottles by fixing the catalyst loading as 5 g/L and placed in direct sunlight. After each one hour duration, the remnant MB solution was obtained by magnetically separating the sample. Absorbance spectrum of remanant MB solution was then measured using UV-Vis-NIR spectrometer.

6.3. Results and discussion

6.3.1. X-ray diffraction analysis

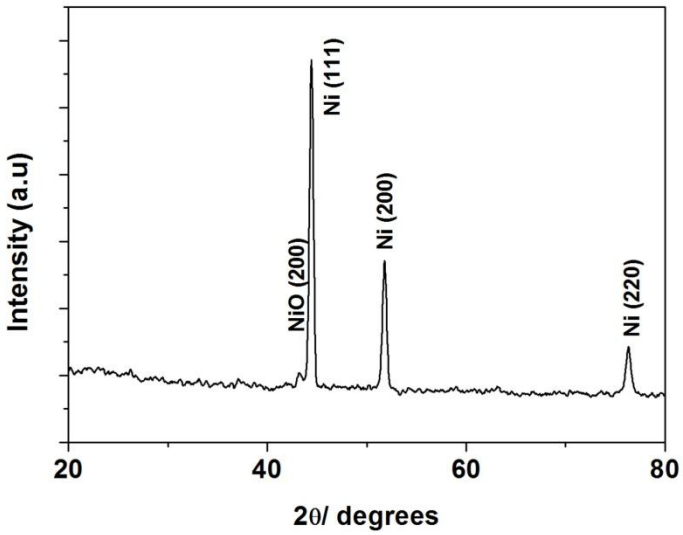

Fig.6.1. *X-ray diffraction pattern of nickel rich Ni/NiO/MWCNT nanocomposites synthesized with MWCNT and precursor salt of Ni/NiO using solution combustion method.*

X-ray diffraction pattern of Ni-NiO-MWCNT show diffraction peaks at 2θ values of 44.44 (111), 51.81(200) and 76.45 (220) which correspond to fcc nickel (JCPDS File No. 04-0850) (Fig.6.1). A low intense peak at 2θ value of 43.19 (200) is observed which corresponds to NiO. It has been noticed that no diffraction pattern was observed corresponding to MWCNT. Average grain size is found using Scherrer formula [Cullity ; 1976] for Ni-NiO-MWCNT and was obtained as ~22 nm for the strongest peak of nickel. The decrease in size of Ni-NiO-MWCNT, when compared to Ni rich Ni-NiO [chapter 3] is due to the influence of MWCNT which cause Ni-NiO nanoparticles to undergo less agglomeration during combustion reaction.

3.2. Vibrational spectral analysis

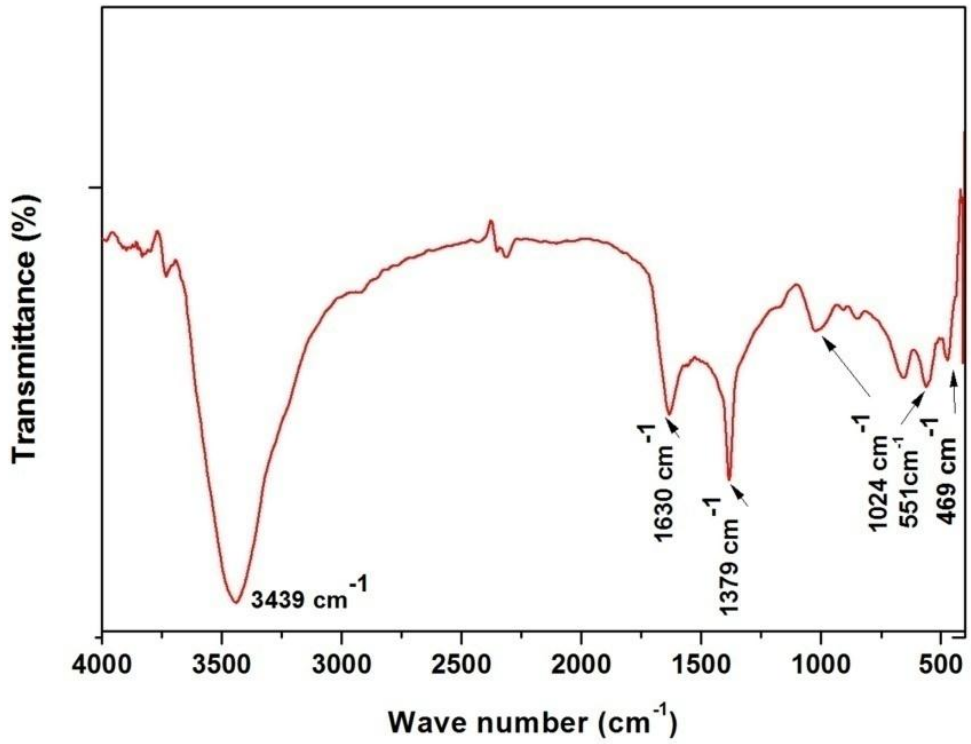

Fig.6.2. *FTIR spectrum of nickel rich Ni/NiO/MWCNT nanocomposites synthesized with MWCNT and precursor salt of Ni/NiO using solution combustion method*

Figure 6.2 and 6.3 presents the FTIR and Raman spectra of Ni-NiO-MWCNT and details of the spectral data is provided in the table 6.1. Moderate intense Raman bands are observed at 167, 195 cm^{-1} respectively. FTIR bands seen at 469 cm^{-1} and 551 cm^{-1} ascribed to O-Ni-O stretching vibrations of NiO bond and are close to reported values [Shanaj *et al*; 2016, Anandan *et al*; 2011].

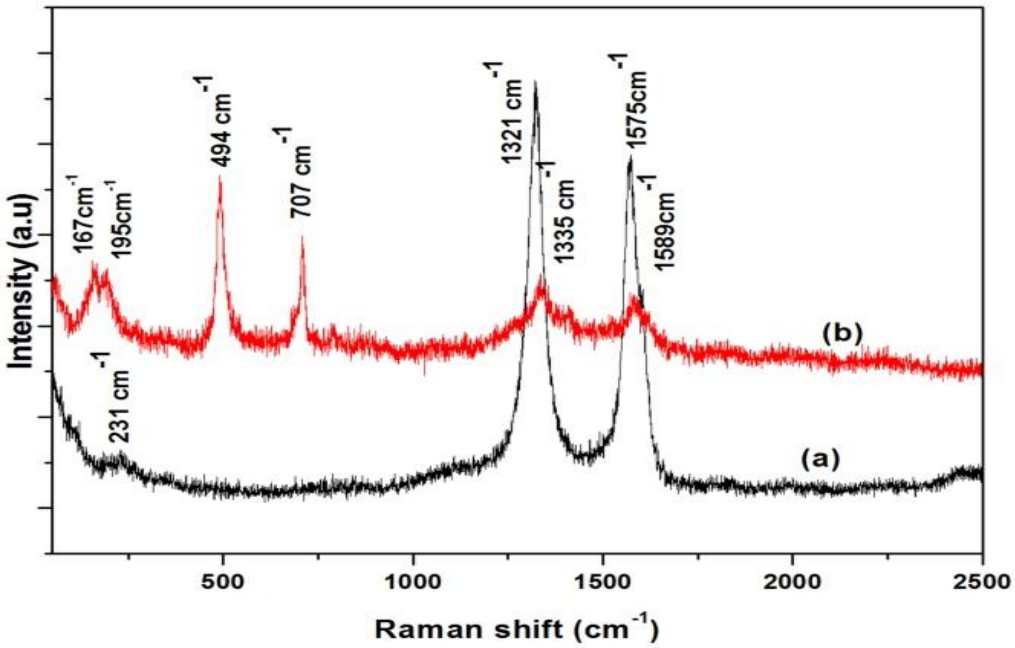

Fig.6.3. *Raman spectra of (a) virgin MWCNT (b) nickel rich Ni/NiO/MWCNT nanocomposites synthesized with MWCNT and precursor salt of Ni/NiO using solution combustion method.*

Table 6.1 Spectral data (cm^{-1})

Raman shift	FTIR	Assignments
	469 w	ν Ni-O
494 vs		ν Ni-O (1LO mode)
	551 w	ν Ni-O
707 s		2TO of NiO
	1024 w	ν C-O
1335 ms		D band
	1379 s	ν C=C
1589 ms		G band
	1630 ms	OH bending vibrations or C=C vibrations
	3439 vs	ν OH

w: weak, ms: medium strong, s: strong, vs: very strong.

The Raman band seen at 494 cm^{-1} is due to symmetric vibrations of nickel-oxygen bond (1 LO mode). This Raman result is closely matched with similar reports on the NiO [Pino *et al*; 2017, Muthu *et al*; 2017, Rajesh *et al*; 2014]. The band obtained at 707 cm^{-1} in Raman spectra could be attributed to 2 TO modes of NiO [Mironova-Ulmane *et al*; 2007, Wang *et al*; 2002]. Presence of carbon is indicated by D and G bands in Raman spectra. D and G bands are observed at 1335 and 1589 cm^{-1} respectively in Ni-NiO-MWCNT while these bands are observed at 1321 and 1575 cm^{-1} in virgin MWCNT. This shows that D and G Raman bands of Ni-NiO-MWCNT are shifted of the order of 14 cm^{-1} to higher energy region. This observation indicates that C-C distance is decreased with respect to that of virgin MWCNT. As stated previously in Ni-NiO-MWCNT two Raman bands are seen at 167 and 195 cm^{-1}, while in MWCNT a single band is seen at 231 cm^{-1}. The splitting of this radial breathing mode (RBM) of MWCNT is probably attributed to the lattice distortion endorsed by the Ni-NiO. Weak FTIR band observed at 1024 cm^{-1} in the present sample is due to C-O stretching vibrations [Shanaj *et al*; 2016]. Strong IR band found at 1379 cm^{-1} is ascribed as the stretching modes of C=C bonds [Wang *et al*; 2015]. Moderately strong FTIR band seen at 1630 cm^{-1} is attributed to C=C bonds of hexagonal network in MWCNT [Silva *et al*; 2012]. Very strong FTIR band observed at 3439 $cm^{-1}$is due to stretching vibrations of OH group of water. The ratio of I_D/I_G gives the crystallinity of carbon and value calculated in the present case is 1.21 for virgin MWCNT and 1.08 for Ni-NiO-MWCNT. This observation shows that MWCNT become slightly more crystalline in Ni-NiO-MWCNT and maintains sp^2 hybridization.

6.3.3. TEM, HRTEM and SAED analysis

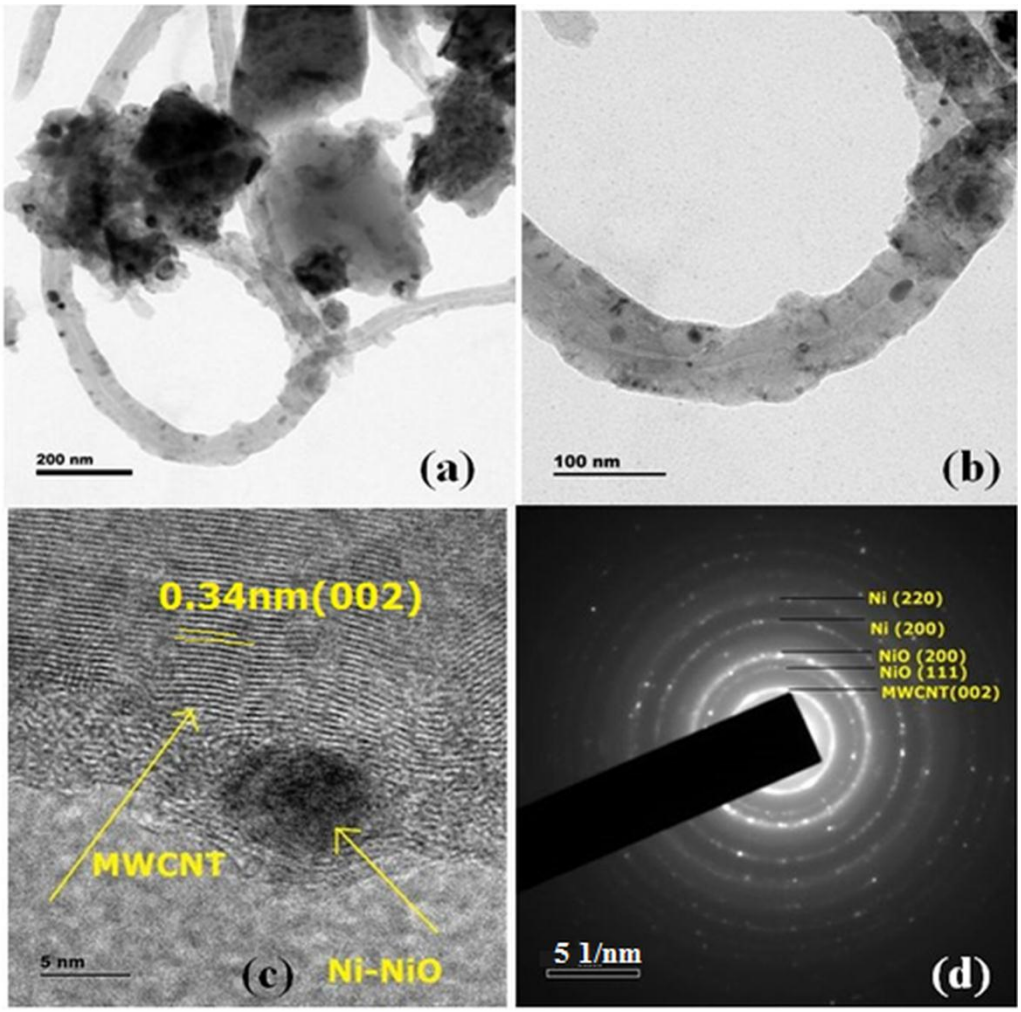

Fig.6.4. *TEM images of nickel rich Ni/NiO/MWCNT nanocomposites synthesised with MWCNT and precursor salt of Ni/NiO using solution combustion method (a) & (b) TEM images at different resolutions of Ni-NiO-MWCNT (c) HR-TEM image of Ni-NiO-MWCNT (d) SAED pattern of Ni-NiO-MWCNT.*

Ni-NiO nanoparticles intercalated with multiwalled carbon nanotube (MWCNT) are observed from the TEM images (Fig. 6.4). High resolution transmission electron microscopy (HR-TEM) shows that Ni-NiO particles are attached with MWCNT (Fig. 6.4c). Selected area electron diffraction pattern (SAED) shows diffraction rings that corresponds to the planes (111)

and (200) of NiO, (200) and (220) of Nickel. The innermost diffraction ring seen in SAED is related to (002) plane of MWCNT.

6.3.4. EDAX analysis

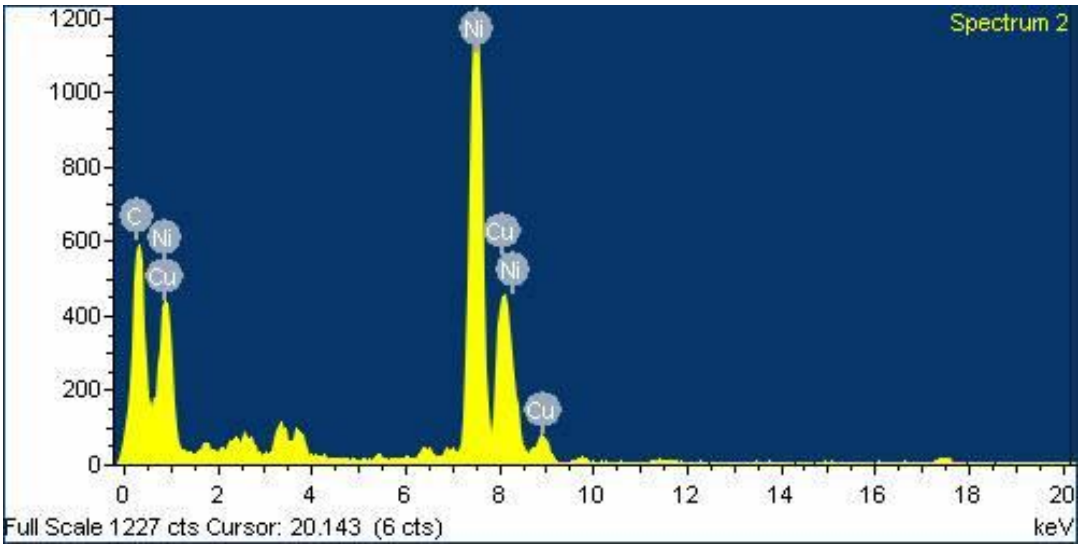

Fig.6.5. *EDAX spectrum of nickel rich Ni/NiO/MWCNT nanocomposites synthesized with MWCNT and precursor salt of Ni/NiO using solution combustion method.*

Figure 6.5 presents the energy dispersive spectroscopy image of sample Ni-NiO-MWCNT. From EDAX analysis, it is found that the atomic percentage of Ni element is about 47.26 % and that of carbon is 34.20 %. From the CHN analysis done on Ni-NiO-MWCNT, presence of carbon is about 3.6 %.

6.3.5. FESEM analysis

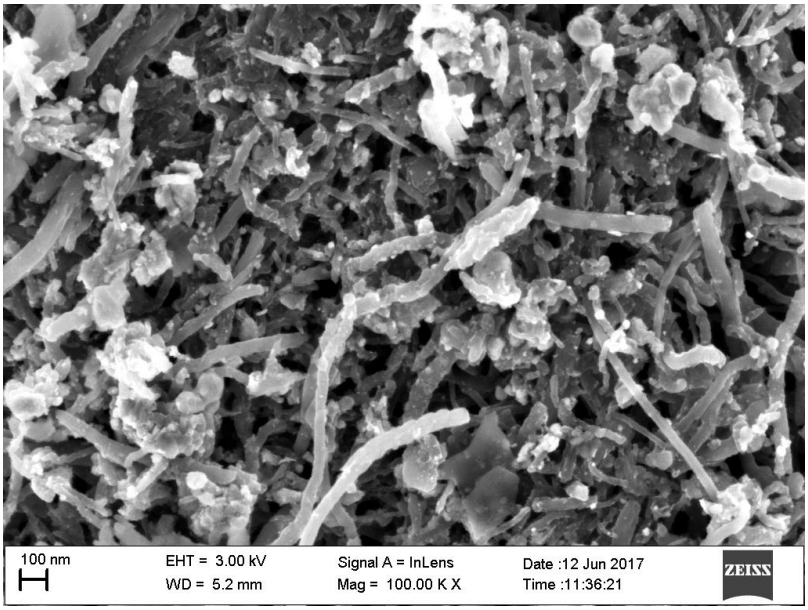

Fig.6.6. *FE-SEM image of nickel rich Ni/NiO/MWCNT nanocomposites synthesized with MWCNT and precursor salt of Ni/NiO using solution combustion method.*

Figure 6.6 shows field emission scanning electron microscopic image of Ni-NiO-MWCNT. It can be observed from figure that MWCNT is inter mixed with Ni-NiO.

Figure 6.7 presents the XPS spectra of Ni-NiO-MWCNT. $Ni2p_{3/2}$ main peak is observed at 855.89 eV and correspond to Ni^{2+} oxidation state of Nickel. Ni^{0} peak is found at 854.38 eV. Both these peaks are found to be shifted to higher binding energy region when compared to Ni rich Ni-NiO and may be attributed to MWCNT attachment to Ni-NiO.

6.3.6. XPS analysis

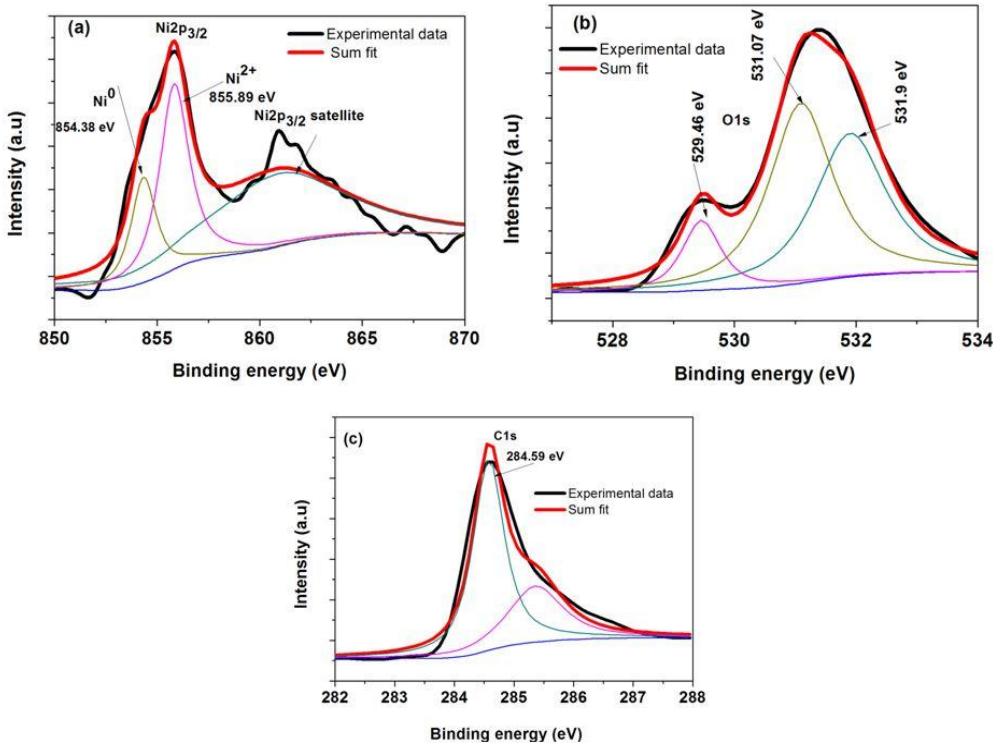

Fig.6.7. *XPS plots of nickel rich Ni/NiO/MWCNT nanocomposites synthesized with MWCNT and precursor salt of Ni/NiO using solution combustion method (a) Ni2p (b) O1s (c) C1s.*

O1s peak is resolved into three sub peaks which are observed at 529.46, 531.07 and 531.9 eV etc.. This means that there is formation of NiO in the present sample other than formation of Ni. Presence of carbon is confirmed by the XPS peaks of C1s found at 284.59 eV.

6.3.7. Electrical properties

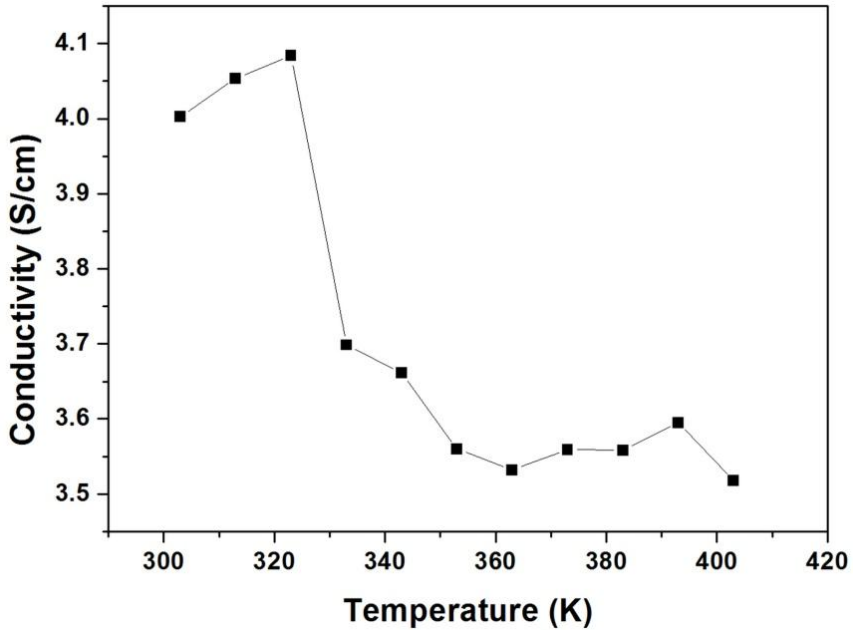

Fig.6.8. *d.c conductivity versus temperature plot of nickel rich Ni/NiO/MWCNT nanocomposites synthesized with MWCNT and precursor salt of Ni/NiO using solution combustion method.*

Figure 6.8 shows the *d.c* conductivity versus temperature plot of Ni-NiO-MWCNT synthesized by solution combustion method. *d.c* conductivity decreases with increase of temperature, showing metallic behavior. Room temperature conductivity of the sample is found to be ~ 4 S/cm which is less than that of Ni rich Ni-NiO in amorphous carbon matrix (~ 24 S/cm) discussed previously (chapter 3). Both MWCNT and Ni-NiO are crystalline materials and may have lattice mismatch. There may be the possibility of the formation of grains of Ni-NiO as well as MWCNT with grain boundaries. Further, our Raman and TEM analysis show that Ni-NiO grains are incorporated in MWCNT. The conducting electrons may likely to scatter at the grain boundaries which in turn lead to the increase of resistance of the material.

6.3.8. Photocatalysis studies

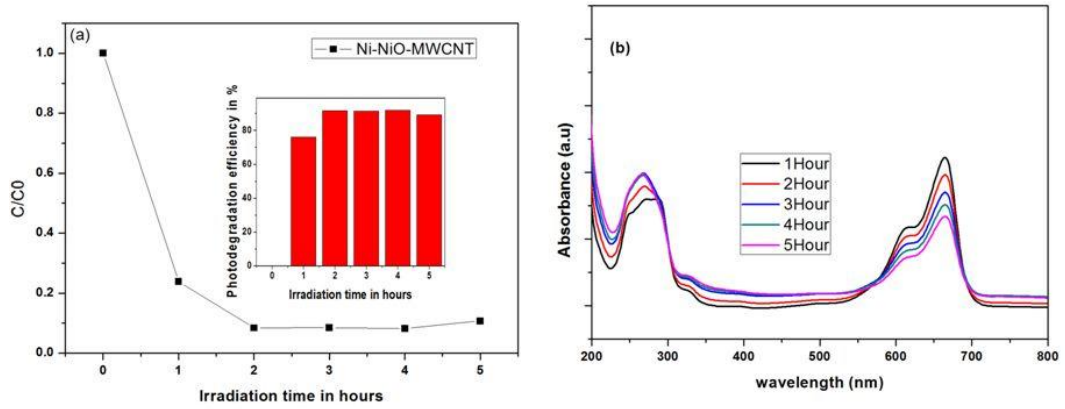

Fig.6.9. *Photodegradation characteristics of nickel rich Ni/NiO/MWCNT nanocomposites synthesized with MWCNT and precursor salt of Ni/NiO using solution combustion method under sun light exposure using methylene blue (MB) as model system (a) C/C_0 versus irradiation time (b) absorbance versus wavelength plot of MBat different time interval*.

Photodegradation investigation of Ni-NiO-MWCNT with MB as dye shows that, concentration of MB decreased with increase of irradiation time (Fig. 6.9). About 76 % of MB has undergone photodegradation process after 1 hour of irradiation time. About 91 % of MB is degraded after 2 hours of sunlight exposure. Photodegradation efficiency of material under investigation is less than that of Ni rich Ni-NiO in amorphous carbon matrix as discussed previously. (chapter 3). Recently Zhang *et al* reported that *d.c* conductivity of Al doped ZnO is related to photocatalytic performance [Zhang *et al*; 2014]. The *d.c* conductivity of Ni-NiO-MWCNT is relatively less than that of Ni rich Ni-NiO. The presence of MWCNT in between Ni-NiO nanoparticles may hinder the easy movement of electrons contributed to the increase in grain boundaries. Relative decrease of *d.c* conductivity of Ni-NiO-MWCNT may be one of the factors for the observed reduction in photodegradation property of Ni-NiO-MWCNT.

6.3.9. Magnetic properties

Table 6.2 : *Magnetic properties of nickel rich Ni/NiO/MWCNT nanocomposites synthesized with MWCNT and precursor salt of Ni/NiO using solution combustion method*

300 K			200 K			20 K		
M_s (emu/g)	M_r (emu/g)	H_c (Oe)	M_s (emu/g)	M_r (emu/g)	H_c (Oe)	M_s (emu/g)	M_r (emu/g)	H_c (Oe)
39	4.5	108	49	5.0	112	51	6.5	142

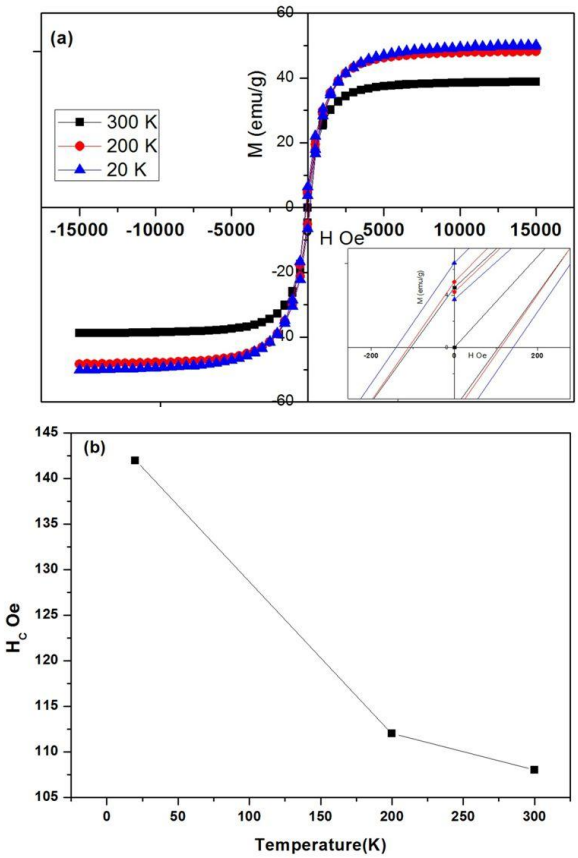

Fig.6.10. *(a) M-H curve of nickel rich Ni/NiO/MWCNT nanocomposites synthesized with MWCNT and precursor salt of Ni/NiO using solution combustion method at 300, 200 and 20 K (b) Coercivity versus temperature plot.*

Figure 6.10 (a) shows M-H curve of Ni-NiO-MWCNT at temperatures of 300, 200, and 20 K respectively. Room temperature coercivity of Ni-NiO-MWCNT is 108 Oe which is higher than that of nickel rich Ni-NiO discussed previously (chapter 3). Its magnetic saturation (M_s) at room temperature is 39 emu/g, with remanant magnetization (M_r) of 4.5 emu/g. Figure 6.10 (b) shows variation of coercivity with temperature. The M_s, M_r and H_c of the sample is slightly increased by lowering the temperature to 200 K (table 6.2). H_c is found to be increased to 142 Oe at 20 K and its M_s is 51 emu/g. The presence of MWCNT in between Ni nanoparticles may decrease the interaction between magnetic moments of the nearby Ni atoms. This will lead to the increase of coercivity in the present sample which is in agreement with our observation. The average grain size of Ni-NiO in Ni-NiO-MWCNT system is ~22 nm from the XRD measurement. This value is less than the average grain size obtained in nickel rich Ni-NiO discussed previously (chapter 3). Interestingly, magnetic coercivity of Ni-NiO-MWCNT is higher than that of Ni rich Ni-NiO with relatively higher size (38 nm) (chapter 3). The observed reduction of M_s in the present sample with respect to that of bulk nickel (55 emu/g) is probably contributed to the size reduction of Ni-NiO in Ni-NiO-MWCNT system. Similar observations are reported in Fe_2O_3/MWCNT system [Cao Y; 2014]. M versus T plot of Ni-NiO-MWCNT is separated each other under field cooling (FC 500 Oe) and zero field cooling (ZFC) (Fig. 6.11(a)). Its blocking temperature is above 300 K. But M-T curve of the sample under FC and ZFC condition is almost merged together up to 175 K, when the experiment is done at an applied field of 2500 Oe (Fig. 6.11 (b)).

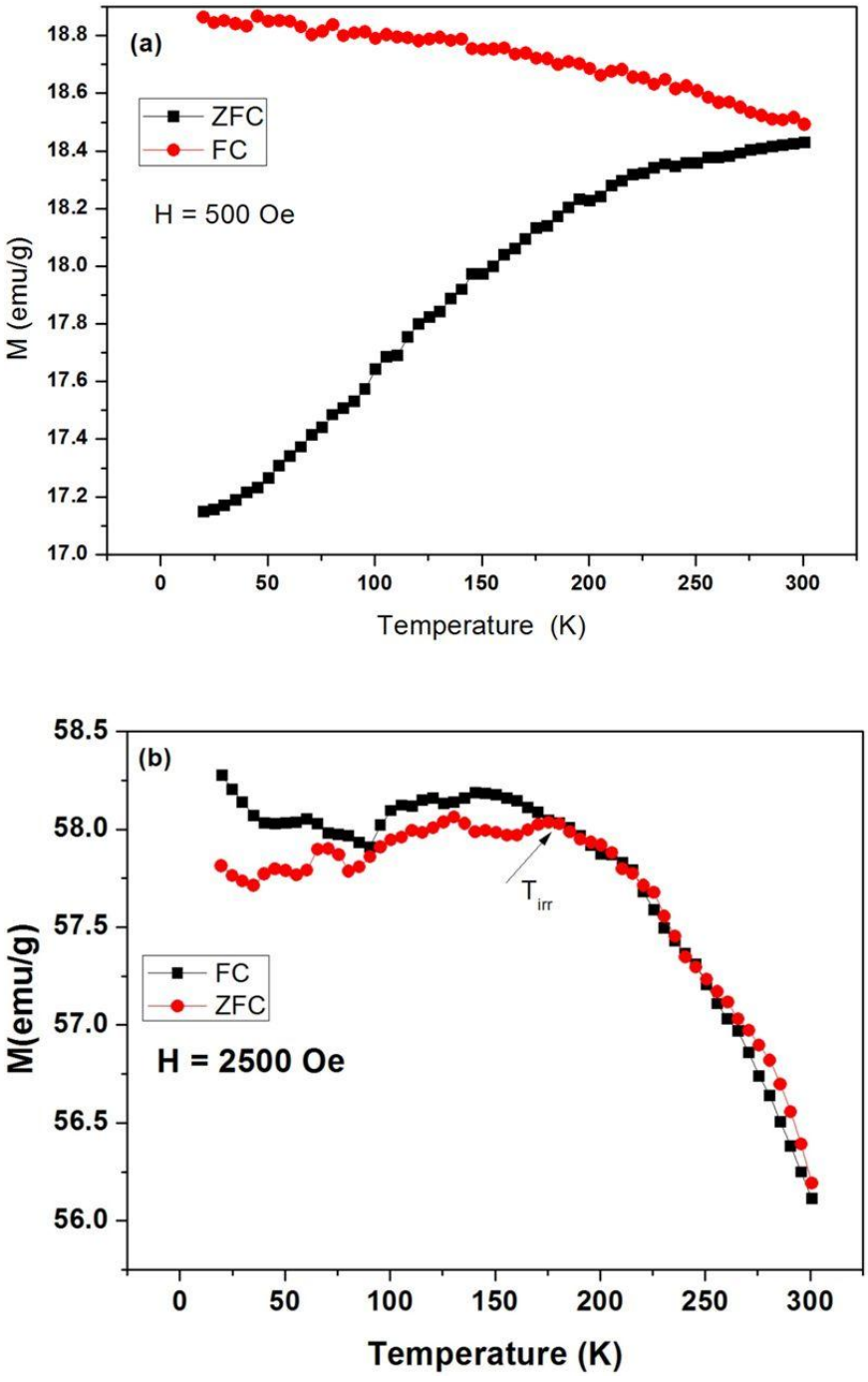

Fig.6.11. *M-T curve of nickel rich Ni/NiO/MWCNT nanocomposites synthesized with MWCNT and precursor salt of Ni/NiO using solution combustion method at field of (a) 500 Oe (b) 2500 Oe.*

6.4. Conclusions

Ni-NiO nanocomposites attached on MWCNT can be synthesized using CNT and Ni-NiO precursor salts by solution combustion method. Crystallinity of MWCNT in Ni-NiO-MWCNT is more than virgin MWCNT. Room temperature coercivity of the Ni-NiO-MWCNT is enhanced to 108 Oe when compared to Ni rich Ni/NiO. The enhancement in the magnetic coercivity of Ni-NiO-MWCNT is attributed the presence of MWCNT matrix which inhibit the interaction of the magnetic moments of adjacent magnetic clusters of Ni atoms. Ferromagnetic and conducting Ni-NiO-MWCNT can be used as an efficient photocatalyst for the photodegradation of methelyne blue (MB) in the presence of sunlight.

.....ൠ.....

Chapter-7

Summary and Future Scope of the Present Work

7.1. Summary of the present work

Magnetic nanoparticles attracted lots of interest due to its uses as catalyst support material, emulsion formation, photocatalyst and for waste water treatment etc. Magnetic nickel (Ni) and nickel oxide (NiO) is an interesting combination of metal and metal oxide which is better for the applications such as catalysis, fuel cells, gas sensors, supercapacitors, spintronic devices etc. Ni rich and NiO rich Ni/NiO nanocomposites in amorphous carbon matrix can be used for magnetic, conducting and photocatalytic applications especially in the presence of sunlight.

Ni rich Ni/NiO nanocomposites in amorphous carbon matrix can be synthesized using nickel acetate, citric acid, $HNO_3$and NH_3 solution at air atmosphere. Quantity of NiO content in Ni/NiO nanocomposites is related to the molarity, fuel (citric acid) to oxidiser (nickel acetate) ratio and the amount of HNO_3used in the combustion reaction. Raman and IR spectral data shows the existence of amorphous carbon matrix for supporting Ni/NiO. SAED pattern of Ni rich Ni/NiO confirms the presence of Ni and NiO in the sample. The oxidation states of Ni in Ni/NiO are Ni^0 and Ni^{2+} as understood from XPS measurement. Ni rich Ni/NiO shows metallic behaviour since its electrical conductivity decreases with respect to temperature. Photodegradation efficiency in the presence of sunlight is a linear function of Ni content and to certain extent it is contributed to the SPR of electrons of Ni in Ni/NiO nanocomposites. Saturation magnetization (M_s) remanant magnetization ($M_{r)}$ and coercivity of Ni rich sample is of the order of 54, 6 emu/g and 82 respectively where as these

values for relatively less nickel content sample is 34, 3 emu/g and 80 Oe. Saturation magnetization decreases with increase in the volume of HNO_3used for its synthesis due to the formation of higher content of antiferromagnetic NiO in Ni/NiO samples. Unintentionally incorporated carbon may decrease the exchange interaction between Ni and NiO and reduce the magnitude of EB and H_c. Ni/NiO nanocomposites having magnetic coercivity of H_c~ 413 Oe could find use in magnetic recording devices.

The ratio of citric acid (fuel) to nickel acetate (oxidiser) is important parameter which determines the quantity of oxidised (NiO) and metallic (Ni) content in solution combustion synthesis process. Nickel atoms in NiO exists in 2p oxidation state and oxygen is in 1s state in Ni/NiO nanocomposites in amorphous carbon matrix synthesized using solution combustion method. Raman spectra of NiO rich Ni/NiO along with carbon gives bands at ~1347 cm^{-1} (D band) and at ~1552cm^{-1}(G band). The intensity ratio of this band is (I_D/I_G) is more than 1 confirming the presence of amorphous carbon matrix. Room temperature electrical conductivity of NiO rich Ni/NiO samples in amorphous carbon matrix are $3.5x10^{-7}$ and $4.5x10^{-8}$ S/cm. Semiconducting behaviour is observed from Arrhenius plots and this behaviour is due to the presence of antiferromagnetic semiconducting NiO. Thermal activation energy increased with respect to Ni content in NiO rich Ni/NiO nanocomposites. UV-Vis absorption spectra of NiO rich Ni/NiO shows absorption at 339 and 381 nm probably due to surface plasmon resonance contributed to electrons from the metallic nickel. NiO rich samples shows photodegradation efficiency of ~89 % in methelyne blue when experiment for determining the photodegradation

efficiency is carried out at 5 g/L of Ni/NiO in 0.025 mM of methelyne blue solution. Photo degradation process of methelyne blue under sunlight exposure in the presence of NiO rich Ni/NiO is contributed to surface plasmon resonance of Ni in Ni-NiO composite system. Magnetic coercivity of NiO rich Ni/NiO samples is found to be 342 and 407 Oe at room temperature. The decrease in nickel content in NiO rich Ni/NiO nanocomposites may lead to the isolation of magnetic nickel nanoparticles with less magnetic interaction resulting in increase in magnetic coercivity. High coercivity values shown by the NiO rich Ni/NiO at room temperature are good for magnetic storage applications. Multifunctional Ni/NiO nanocomposites in amorphous matrix can be used for magnetic, electrical and photocatalytic applications in the presence of sunlight.

Graphite and graphene are important carbonaceous crystalline material with good mechanical strength. These materials can be used for protecting magnetic materials like Ni from its environment. Nickel rich Ni-NiO nanocomposites embedded in graphite and graphene matrix can be synthesized by using graphite/graphene and precursor salts of Ni/NiO in appropriate ratio. In order to get nickel rich compositions the quantity of HNO_3 used for the synthesis is limited to 30 ml. X-ray peaks corresponding to graphite and graphene are obtained at 2θ value of 26.5^0. IR and Raman spectra of Ni rich Ni/NiO in graphite and graphene matrix gives bands contributed to graphite and graphene in addition to bands from NiO. XPS and EDAX analysis shows presence of nickel, oxygen and carbon as major elements. Ni/NiO embedded in graphite shows *d.c* conductivity value of 3.96 S/cm at room temperature. However *d.c* conductivity value of Ni/NiO in graphene matrix is of the order of 0.13 S/cm at room. *d.c* conductivity

measurement establishes Ni-NiO embedded in graphite has larger value of conductivity when compared to Ni-NiO embedded in graphene. The I_D/I_G value of Ni-NiO embedded in graphite is 0.49 which is higher than Ni-NiO embedded in graphene (0.17). It can be understood from this observation that, defect levels of carbon is more in Ni-NiO embedded in graphite than Ni-NiO embedded in graphene. This indicates that carbon present Ni-NiO embedded in graphene is more crystalline than Ni-NiO embedded in graphite. This may be the reason for higher conductivity of Ni/NiO embedded in graphite when compared to Ni-NiO embedded in graphene. Photodegradation efficiency of Ni-NiO embedded in graphite is of the order of 43 % and that of Ni-NiO embedded in graphene is of the order of 96 %. Photodegradation efficiency of Ni-NiO embedded in graphene is higher than that of Ni-NiO embedded in graphite may be due to larger surface area of graphene. Room temperature coercivity of Ni-NiO embedded in graphite is obtained to be 118 Oe which is higher than Ni-NiO embedded in graphene because of its efficient wrapping of Ni magnetic moments.

Solution combustion method can be used for the synthesis of Ni-NiO nanocomposites attached on the MWCNT using MWCNT, nickel acetate, citric acid, HNO_3 and NH_3 solution. Raman spectra corresponds to MWCNT is observed at 1335 cm^{-1} (D band) and at 1589 cm^{-1} (G band). It is interesting note that crystallinity of MWCNT in Ni-NiO-MWCNT is higher than virgin MWCNT as evidenced from its I_D/I_G value as 1.08. Magnetic coercivity of Ni rich Ni/NiO in amorphous carbon matrix is of the order of 80 Oe. Room temperature coercivity of the Ni-NiO-MWCNT is enhanced to 108 Oe when compared to Ni rich Ni-NiO. The enhancement in coercivity of Ni-NiO-MWCNT is attributed to the presence of MWCNT

matrix which prevent interaction of the magnetic moments of adjacent magnetic clusters. Ni-NiO-MWCNT is showing conducting behaviour and its room temperature conductivity is of the order of 4 S/cm. Ni-NiO-MWCNT gives about 91 % photodegradation efficiency after 2 hour exposure to sunlight. The magnetically separable photocatalyst Ni-NiO-MWCNT can be used as efficient material for treating contaminated water from the textile industries with the irradiation of sunlight. This material can be also be used as conducting paints.

7.2. Future scope

In the present work, the effect of quantity of HNO_3 in the formation of NiO in Ni/NiO composite synthesized by solution combustion method is studied. It is also observed that pore sizes of the sample decreases with increase in amount of HNO_3 used for the combustion synthesis. It is interesting one to carryout experiments in this direction by further changing the volume of HNO_3 so as to get more information about the nature of pore and its sizes as a result of addition of HNO_3 in to the reactants. Porous Ni/NiO structures are good for gas sensing as well as hydrogen storage applications. Further, chemical composition and microstructure of the combustion products are related to fuel to oxidiser ratio, chemical nature of the fuel and acidity of the precursor medium. The study of effect of decreasing the fuel to oxidiser ratio gives NiO rich Ni/NiO sample, one can study the effect of fuel on evolution of microstructure of the sample by selecting the different types of fuels such as glucose, sugar, glycine, urea etc. Magnetic properties and chemical composition of the sample can be protected by embedding the Ni/NiO in different non magnetic materials such as carbon, silica, polymers etc. Studies on influence of the graphite,

graphene, MWCNT on conducting, photocatalytic and magnetic properties of Ni/NiO is presented in this work. Studies in this way can be extended by incorporating Ni/NiO in reduced graphene oxide (RGO), graphene oxide (GO), polymers such as polyaniline, polypyrrole etc. NiO rich Ni/NiO can be synthesized by changing the fuel to oxidiser ratio from 2:1 to 1:1 and 1:2. These nanocomposites are suitable for Li-ion batteries as future anode materials. The combustion synthesized Ni/NiO nanocomposites can be pelletised and converted into Ni/NiO bilayer film by sputtering or pulsed laser deposition. The information about exchange bias exists in Ni/NiO bilayer film will be effective for the fabrication magnetic storage devices. Structural studies of the materials are fundamentally important in materials science since materials may change its structure from one crystalline phase to another one when it is subjected to high pressure and temperature. It is interesting to know the phase transition of the Ni/NiO embedded in different matrices with respect to high pressure and temperature. Also the combustion synthesized Ni/NiO is having porous structure, the feasibility of using these materials in hydrogen storage application would be a research problem in future. As understood from our studies ferromagnetic Ni is protected with crystalline as well as amorphous carbon matrix. It is interesting to make thin films of these materials which have more data storage capacity. The thin films of these materials can be deposited on substrate like glass, silicon etc with the aid of pulsed laser sources.

Photocatalytic properties of these materials under exposure to sunlight is one of the important properties as understood from present investigation. We have investigated photodegradation property of Ni/NiO nanocomposites with methelyne blue as a model dye system. It is

interesting to investigate photodegradation properties of Ni rich and NiO rich Ni/NiO in different dyes such as methyl orange, Rhodamine B, crystal violet etc. These studies will provide fruitful information for the industrial use of Ni/NiO nanocomposites for treating waste water from textile industries in the presence of sunlight.

.....ൟ.....

Abbreviations

AFM	Antiferromagnetic
CBD	Cluster Beam Deposition
CCD	Charge Coupled Device
CNT	Carbon Nano Tube
CRT	Cathode Ray Tube
DRS	Diffuse Reflectance Spectroscopy
DTA	Differential Thermal Analysis
EB	Exchange Bias
EDAX	Energy Dispersive X-ray Spectroscopy
FC	Field Cooling
Fcc	Face Cantered cubic
FESEM	Field Emission Scanning Electron Microscope
FM	Ferromagnetic
FTIR	Fourier Transform Infrared Spectroscopy
FT-Raman	Fourier Transform Raman Spectroscopy
FWHM	Full Width at Half Maximum
hcp	Hexagonal close packed
HRTEM	High Resolution Transmission Electron Spectroscopy
IR	Infra Red
JCPDS	Joint Committee on Powder Diffraction Standards
LO	Longitudinal Optical
LO	Longitudinal Optical
MB	Methylene Blue
MWCNT	Multiwalled Carbon Nano Tube
Ni	Nickel

NiO	Nickel oxide
nm	nano meter
PMT	Photo Multiplier Tube
RBM	Radial Breathing Mode
RIR	Reference Intensity Ratio
SAED	Selected Area Electron Diffraction
SCS	Solution Combustion Synthesis
SEM	Scanning Electron Microscopy
SHS	Self propagating High temperature Synthesis
SPR	Surface Plasmon Resonance
Tc	Curie temperature
TEM	Transmission Electron Microscopy
TGA	Thermo Gravimetric Analysis
T_N	Neel temperature
TO	Transverse Optical
UV	Ultra Violet
VSM	Vibrating Sample Magnetometer
XPS	X-ray Photoelectron Spectroscopy
XRD	X-ray Diffraction
ZFC	Zero Field Cooling

.....ꕥ.....

References

1) Adekunle A S, Ozoemena K I, *J. Electroanal. Chem*., **645** 41 (2010).

2) Ahmadvand H, Salamati H, Kameli P, Razavi F S, *J. Supercond. Nov. Magn.,* **23** 1467 (2010).

3) Alagiri M, Ponnusamy S, Muthamizhchelvan C, *J. Mater Sci: Mater Electron,***23** 728 (2012).

4) Alammar T, Shekhah O, Wohlgemuth J, Mudring A-V, *J. Mater. Chem.,***22** 18252 (2012).

5) Anandan K, Rajendran V, *Mater. Sci. Semicond. Process.,***14** 43 (2011).

6) Anandan K, Rajendran V, *Nanosci. Nanotech. An Int.J,* **2** 24 (2012).

7) Aruna S T, Mukasyan A S, *Curr. Opin.Solid.St.Mat. Sci.,***12** 44 (2008).

8) Aruna S T, Rajam K S, *Mater. Res. Bull.*, **39** 157 (2004).

9) Bai L, Yuan F, Tang Q, *Mat.Let.,***62** 2267 (2008).

10) Banwell C N, McCash E M, Fundamentals of Molecular Spectroscopy, Tata McGraw Hill, 4th edition (1994).

11) Barakat A, Al-Noaimi M, Suleiman M, Aldwayyan A S, Hammouti B, Hadda T B, Haddad S F, Boshaala A, Warad I*, Int. J. Mol. Sci.,***14** 23941 (2013).

12) Baran S, Hoser A, Penc B, Szytuła A, *Acta. Phys. Pol. A*, **129** 35 (2016).

13) Behrad F, Farimani M H R, Shahtahmasebi N, Roknabadi M R, Karimipour M, *Eur. Phys. J. Plus,* **130** 144 (2015).

14) Bora C, Kalita A, Das D, Dolui S K, Mukhopadhyay P K, *Polym. Int.,* **63** 445 (2014).

15) Buerger M J, X-ray Crystallography, John Wiely and Sons, New York, 3rd edition, (1962).

16) BunaciuA,Udrstioiu E G,Aboul-Enein H, X-Ray Diffraction: Instrumentation and Applications, *Cr. Revs.An.Chem,* **45** 289 (2015).

17) Cakici M, Reddy K R, Alonso - Marroquin F, *Chemical Eng. J.*, **309** 151 (2017).

18) Cao P, Wang L, Xu Y, Fu Y, Ma X, *Electrochim. Acta,***157** 359 (2015).

19) Cao Y, *Fullerenes,Nanotubes and Carbon Nanostructures,***23** 623 (2014).

20) Carreno T, Morales M P, Serna C J, *J. Phys. D: Appl. Phys.,***42** 224002 (2009).

21) Chandra S, Kumar A, Tomar P K, *J.Saudi Chem. Soc.,* **18** 437 (2014).

22) Chang H, Su H-T, *Rev.Adv.Mater.Sci.*,**18** 667 (2008).

23) Chantry G W, Gebbie H, Hilsum A C, *Nature*, **203**, 1052 (1964).

24) Chase D B, Hirschfeld T, *Appl. Spectrosc.,***40** 133 (1986).

25) Chaudhary R G, Tanna J A, Gandhare N V, Rai A R, Juneja H D, *Adv. Mater. Lett.,***6** 990 (2015).

26) Chen D-H, Hsieh C-H, *J.Mater.Chem.*,**12** 2412 (2002).

27) Chen D-H, Wu S-H, *Chem. Mater.*, **12** 1354 (2000).

28) Chen X H, Chen C S, Xiao H N, Liu H B, Zhou L P, Li S L, Zhang G, *Tribol. Int*., **39** 22 (2006).

29) Chen X, Zheng Z, Ke X, Jaatinen E, Xie T, Wang D, Guo C, Zhao J, Zhu H, *Green Chem.,* **12** 414 (2010).

30) Chen Y, Peng D-L, Lin D, Luo X, *Nanotechnology,* **18**, 505703 (2007).

31) Chin K C , Gohel A, Elim H I, Ji W, Chong G L, Lim K Y, Sow C H, Wee A T S, *Chem. Phys. Lett.,***383** 72 (2004).

32) Chitpong N, Husson S M, *J. Membrane Sci.,* **523** 41 (2017).

33) Choi T, Kim S H, Lee C W, Kim H, Choi S-K, Kim S-H, Kim E, Park J, Kim H, *Biosens. Bioelectron*.,**63** 325 (2015).

34) Chopra N, Claypoole L, BachasL G, *J. Nanopart. Res*., **12** 2883 (2010).

35) Couto G G, Klein J J, Schreiner W H, Mosca D H, de Oliveira A J A, Zarbin A J G, *J.Coll. Inter. Sci*., **311** 461 (2007).

36) Cullity B D and Stock S R, Elements of X-ray diffraction , Prentice Hall, New Jersey, 3rd edition , (2001).

37) Cullity B D, Elements of X-ray Diffraction, Addison-Wesley Publishing Co. Inc. (1976).

38) Cullity B D, Graham C D, Introduction magnetic materials, Wiely , A John Wiely&Sons , Inc, Pub. (2009).

39) Del Bianco L, Spizzo F, Tamisari M, Castiglioni A, *J. Appl. Phys.,***110** 043922 **(**2011).

40) Deraz N M, *Int. J. Electrochem. Sci*., **7** 4608 (2012).

41) Deraz N M, *Curr. Appl. Phys.,* **12** 928 (2012).

42) Dewi S H, Sutanto, Fisli A, Wardiyati S, *J. Phys. Conf. Ser.,* **739**012113 (2016).

43) Dharmaraj N, Prabu P, Nagarajan S, Kim C H, Park J H, Kim H.Y,*Mater. Sci. Eng., B,* **128** 111 (2006).

44) Dinh N X, Huy T Q, Vu L V, Tam L T, Le A-T, *J.Sci. Adv. Mat. Devices,***1** 84 (2016) .

45) Diva T N, Zare K, Taleshi F, Yousefi M, *J. Nanostruct. Chem.,* **7** 273 (2017).

46) Dong P, Hou G, Xi X, Shao R, Dong F *Environ. Sci.: Nano,***4** 539 (2017).

47) Dooley K M, Chen S Y, Ross J R H,*J. Cats.,***145** 402 (1994).

48) Doppiu S, Langlais V, Sort J, Surinach S, Baro M D, Zhang Y, Hadjipanayis G, Nogues J, *Chem. Mater.*, **16** 5664 (2004).

49) Double M, Kumar A, Biotreatment of Industrial Effluents. Elsevier, Amsterdam, The Netherlands (2005).

50) Duan W J, Lu S H, Wu Z L, Wang Y S, *J. Phys. Chem. C*, **116** 26043 (2012).

51) Egerton R F, Physical Principles of Electron Microscopy, Springer (2005).

52) Elazab H A, Siamaki A R, Moussa S, Gupton B F, El- Shall M S, *Appl. Catal., A*, **491** 58 (2015).

53) El-Kemary M, Nagy N, El-Mehasseb I, *Mater. Sci. Semicond. Process.,***16** 1747 (2013).

54) Estournes C, Lutz T, Happich J, Quaranta T, Wissler P, Guille J L, *J. Magn. Magn.Mater*.,**173** 83 (1997).

55) Faezeh F, Sara H, *Mat. Sci. Appl.*, **3** 697 (2012).

56) Fan L, Tang L, Gong H, Yao Z, Guo R, *J. Mater. Chem.,* **22** 16376(2012).

57) Fang L J, Wang X L, Li Y H, Liu P F, Wang Y L, Zeng H D, Yang H G, *Appl. Catal., B Environ.,***200** 578 (2017).

58) Farhadi S, Roostaei-Zaniyani Z, *Polyhedron,***30** 971 (2011).

59) Fernanda G M, Jose D A, Rochel M L, Juliana C T, *J. Braz. Chem. Soc.,***26** 2379 (2015).

60) Figueroa-Torres M Z, Domınguez-Rios C, Cabanas-Moreno J G, Vega-Becerra O, Aguilar-Elguezabal A, *Int. J. Hydrog. Energy,* **37** 10743 (2012).

61) Flewitt P E J, Wild R K, Physical methods for materials characterization, CRC Press Second Ed.(2015).

62) Foner S, *Rev.Sci.Instr.,***30** 548(1959).

63) Fonseca F C, Ferlauto A S, Alvarez F, Goya G F, Jardim R F, *J. Appl. Phys,***97** 044313 (2005).

64) Fonseca F C, Goya G F, Jardim R F, Muccillo R, Carren˜o N L V, Longo E, Leite E R, *Phys. Rev. B*, **66** 104406 (2002).

65) Fraune M, Rüdiger U, GüntherodtG,Cardoso S, Freitas P, *Appl. Phys. Lett.*,**77**, 3815 (2000).

66) Frenkel J, Doefman J, *Nature,***126** 952 (1930).

67) Fu M, Jiao Q, Zhao Y, Li H, *J. Mater. Chem.A,***2** 735 (2014).

68) Fu Y, Lin C, Pan K, *J. Alloys Compd.,***349**228 (2003).

69) Georgakilas V, Gournis D, Tzitzios V, Pasquato L, Guldi D M,PratoM, *J. Mater. Chem.*, **17** 2679 (2007).

70) Ghosh M, Biswas K, Sundaresan A, Rao C N R, *J. Mater. Chem*., **16** 106 (2006).

71) Goncharova O I, Yurieva T M,*React. Kinet.Catal.Lett.,***15** 73 (1980).

72) Gondal M A, Hameed A, Yamani Z H, Suwaiyan A, *Chem. Phys. Let.,***385** 111 (2004).

73) Gondal M A, Sayeed M N, Alarfaj A, *Chem. Phys. Lett.*, **445** 325 (2007).

74) Gracia M A, *J.Phys. D: Appl.Phys,* **44**283001 (2011).

75) Granitzer P, Rumpf K, *Materials,***4** 908 (2011).

76) Gubin S P, Magnetic Nanoparticles, Wiley-VCH, Weinheim(2009).

77) Gund G S, Dubal D P, Shinde S S, Lokhande C D, *ACS Appl. Mater. Interfaces,***6** 3176 (2014).

78) Guskos N, Anagnostakis E A, Guskos A, *J. Achiev. Mater. Man.Eng*, **24**, 26 (2007).

79) Hameed A, Gondal M A, *J.Mol. Cat. A: Chem.,***219** 109 (2004).

80) Hao R, Xing R, Xu Z, Hou Y, Gao S and Sun S, *Adv. Mater.*, **22** 2729 (2010).

81) Harraz F A, Mohamed R M, Shawky A, Ibrahim I A, *J. Alloys Compd.*, **508** 133 (2010).

82) HassanA J,*J. Modern Phys.,* **5** 2184 (2014).

83) Hayat K, Gondal M A, Khaled M M, Ahmed S, *J. Mol. Catal. A: Chem.,***336** 64 (2011).

84) He X, Zhong W, Au C-T, Du Y, *Nanoscale Res. Lett.*, **8** 446 (2013)

85) Hotovy I, Huran J, Siciliano P, Capone S, Spiess L, Rehacek V, *Sens. Actuators B,***78** 126 (2001).

86) Hou Y, Gao S, *J. Mater. Chem.*, **13** 1510 (2003).

87) Hou Y, Kondoh H, Ohta T, Gao S, *Appl. Surf. Sci.,***241** 218 (2005).

88) Huang H X, Tu J P, Zhang B, Zhang C Q, Li Y, Yuan Y F, Wu H M,*J. Power Sources*, **161** 541 (2006).

89) Huang P, Zhang X, Wei J, Pan J, Sheng Y, Feng B, *Mater. Res. Bull.,***63** 112 (2015).

90) Hubbard C R, Snyder R L, *Powder Diffr.,***3**74 (1988).

91) Hui L, Ai-Ping C, Xiu-Li S, Jun T, Chun-Zhong L, *J.Inorg. Mat.,* **29**1061 (2014).

92) Hummel R E, Electronic Properties of Materials, Springer, (2010)

93) Hwang J-H, Dravid V P, Teng M H, Host J J, Elliot B R, Johnson D L, Mason T O, *J. Mater. Res.*, **12** 1076 (1997).

94) Iijima S, *Nature,***354** 56 (1991).

95) Ishizaki T, Yatsugi K, Akedo K, *Nanomaterials*,**6**172 (2016). *J Mater Sci: Mater Electron,***27** 1244 (2016).

96) Jain G M, Rajesh R, Venkatesan R, *Adv. Mat. Res.*,**938**91 (2014).

97) Jain P K, Huang X, El-Sayed I H, El-Sayed M A, *Plasmonics,* **2** 107 (2007).

98) Jan S, PavelH,*Chem. Eng. Trans.,***32** 79 (2013).

99) Jayalakshmi M, Palaniappa M, Balasubramanian K, *Int. J. Electrochem. Sci.,***3** 96 (2008).

100) Jeffrey J. W, X□Ray Photoelectron Spectroscopy, Wiley &Sons Inc. (2013).

101) Ji Z, Shen X, Zhu G, Zhou H, Yuan A, *J. Mater.Chem.,***22** 3471 (2012).

102) Johll H, Lee M D K, Ng S P N, Kang H C, Tok E S, *Sci. Rep.,* **4** 7594 (2014).

103) Johnston-Peck A C, Wang J, Tracy J B, *ACS Nano*, **3** 1077 (2009).

104) Joo S H, Park J Y, TsungCh -K,Yamada Y, Yang P, Somorjai G A *Nat. Mater.,***8** 126 (2009).

105) Joseph Antony R K, Viswanathan B, *Ind. J.Chem.,***50A** 176 (2011).

106) Jung C-H, Jalota S, Bhaduri S B, *Mater. Lett.,***59** 2426 (2005).

107) Justin P, Meher S K, Rao G R, *J. Phys. Chem. C*, **114**5203 (2010).

108) Kahimbi H, Hong S B, Yang M, Choi B G, *J. Electroanal. Chem.,***786** 14 (2017).

109) Kalaie M R, Youzbashi A A, Meshkot M A, Hosseini-Nasab F, *Appl.Nanosci*., **6** 789 (2016).

110) Kang L, Deng J, Liu T, Cui M, Zhang X, Li P, Li Y, Liu X, Liang W, *J. Power Sources,***275** 126 (2015).

111) Kannan M K, Fundamentals and Applications of magnetic materials, Oxford University press (2016).

112) Karmhag R, Niklasson G A,Nygren M, *J.Appl.Phys.*, **89** 3012 (2001).

113) Kerfoot D G E Nickel In: Ullmann's Encyclopedia of Industrial Chemistry Wiley-VCH Verlag GmbH & Co (2002).

114) Kianfar A H, Dehghani P, Momeni M M, *J. Mater.Sci: Mater Electron,* **27** 3368 (2016).

115) Kim H-S, Lee H, Han K-S, Kim J-H, Song M-S, Park M-S, Lee J-Y, Kang J-K , *J. Phys. Chem. B*, **109***,* 8983 (2005).

116) Kim O-K, Je J, Baldwin J W, Kooi S, Pehrsson P E, Buckley L J, *J. Am. Chem. Soc.*,**125** 4426 (2003).

117) KimS P, Choi M Y, ChoiH C **,** *Mat.Res.Bull.,***74** 85 (2016).

118) Kittel C. *Rev. Modern. Phys.,* **21(4)** 541 (1949).

119) Knobel M, Nunes W C, Socolovsky L M, De Biasi E, Vargas J M, Denardin J C,*J. Nanosci. Nanotechnol.,***8** 2836 (2008).

120) Kremenovic A, Jancar B, RisticM, Vucinic-Vasic M,Rogan J,Pacevski A, Antic B, J. *Phys. Chem. C*, **116** 4356 (2012).

121) Krishnan R V, Banerjee A, *Rev.Sci.Instr.,* **70**85 (1999).

122) Kumar D R, Manoj D, Santhanalakshmi J, *Anal. Methods*, **6** 1011 (2014).

123) Kurokawa A, Sakai N, Zhu L, Takeuchi H, Yano S, Yanoh T, Onuma K, Kondo T, Miike K, Miyasaka T, Ichiyanagi Y*, J. Kor. Phys. Soc.*, **63** 716 (2013).

124) Langevin P, *Ann. Chemieet Physique,* **5** 70 (1905).

125) Layek S, Verma H C, *J. Magn. Magn. Mater.*,**397**73 (2016).

126) Lee D-H, Kim J-C, Shim H-W, Kim D-W, *ACS Appl. Mater. Interfaces,* **6** 137 (2014).

127) Lee I S, Lee N, Park J, Kim B H, Yi Y-W, Kim T, Kim T K, Lee I H, Paik S R,Hyeon T, *J. Am. Chem. Soc.*, **128** 10658 (2006).

128) Lee S J, Kim H B, Oh S H, Kang P H, *J.Magn.*,**20**241 (2015).

129) Li G-J, Huang X-X, Shi Y, Guo J-K, *Mater. Lett.,* **51** 325 (2001).

130) Liang Z, Huo R, Yin Y-X, Zhang F, Xu S, Guo Y-G,*Electrochim. Acta*, **108** 429 (2013).

131) Lin K-Y, Tsai W-T, Chang J-K, *Int. J. Hydrogen Energy,* **35**7555 (2010).

132) Lin S-H, Chen F-R, Kai J-J,*Appl. Surf.Sci.*, **254** 3357 (2008).

133) Liu B, Weller D K, U.S. Patent 7, 158,346 B2 (2007).

134) Liu D, Li D, Yang D, *AIP Advances,* **7** 015028 (2017).

135) Liu T, Pang Y, Xie X, Qi W, Wu Y, Kobayashi S, Zheng J, Li X, *J. Alloys.Compd.,* **667** 287 (2016).

136) Liu W, Lu C, Wang X, Liang K, Tay B K, *J. Mater. Chem.A,* **3** 624 (2015).

137) Lund M S, Macedo W A A, Liu K, Nogues J, Schuller I K, Leighton C, *Phys. Rev. B,* **66** 054422 (2002).

138) Luyo C, Ionescu R, Reyes L F, Topalian Z, Estrada W, Llobet E, Granqvist C G, Heszler P, *Sens. Actuators B,***138** 14 (2009).

139) Mansour N B,Najeh I, Mansouri S, El Mir L, *Appl. Surf. Sci*., **337** 158 (2015).

140) Manukyan K V, Chen Y-S, Rouvimov S, Li P, Li X, Dong S, Liu X, Furdyna J K, Orlov A, Bernstein G H, Porod W, Roslyakov S, Mukasyan A S, *J. Phys. Chem. C,***118** 16264 (2014).

141) Manukyan K V, Cross A, Roslyakov S, Rouvimov S, Rogachev A S, Wolf E E, Mukasyan A S, *J.Phys.Chem. C,* **117** 24417 (2013).

142) Margaris G, Trohidou K N, Nogues J,*Adv. Mater.,***24 4331** (2012).

143) Masipa P M, Magadzu T, MkhondoB, *S. Afr. J. Chem.,***66** 173 (2013).

144) Meiklejohn W H and Bean C P, *Phys. Rev.,* **105** 904 (1957).

145) Meiklejohn W H, Bean C P, *Phys. Rev.*, **102** 1413 (1956).

146) Meiklejohn W H, *J. Appl. Phys.,* **33** 1328 (1962).

147) Miller E L and Rocheleau R E, *J. Electrochem. Soc.,***144** 3072 (1997).

148) Mironova-Ulmane N, Kuzmin A, Steins I, Grabis J, Sildos I, Pars M, *J. Phys.: Conf. Ser.,***93**012039 (2007).

149) Morrish A H, The Physical Principles of Magnetism, Wiley, New York, (1965).
Moshfegh A Z,*Thin Solid Film,***605** 2 (2016).

150) Motahari F, Mozdianfard M R, Soofivand F, Salavati-Niasari M, *RSC. Adv.,* **4** 27654 (2014).

151) Murai M., Takizawa K, Soejima K, Sotouchi H, *J. Electrochem. Soc.,***143** 2481 (1996).

152) Muthu K S, Perumal P, *J.Mater. Sci: Mater Electron,***28** 9612 (2017).

153) Nandapure B I, Kondawar S B, Salunkhe M Y, Nandapure A I, *Adv. Mat. Lett*.,**4** 134 (2013).

154) Neda A, Alireza N-E, *Mat. Sci. Semi. Proc.*, **36** 162 (2015).

155) Neel L, *Ann.de Physique,* **18** 5 (1932).

156) Neel L, *Ann.Phys.,* **3** 137 (1948).

157) Nelson P A, J R Owen,*J. Electrochem. Soc.,* **150** A1313 (2003).

158) Neppolian B, Choi H C, Sakthivel S, Arabindoo B, Murugesan V, *Chemosphere*, **46** 1173 (2002).

159) Nguyen V C, Nguyen N L G, Pho Q H, *Adv. Nat. Sci.: Nanosci. Nanotechnol*., **6** 035001 (2015).

160) Nikolaou V, CharisiadisA, CharalambidisG, CoutsolelosAG, OdobelF, *J. Mater. Chem.A*, **5** 21077 (2017).

161) Nogues J, Langlais V, Sort J, Doppiu S, Surinach S, Baro M D, *J. Nanosci. Nanotechnol.*, **8** 2923 (2008).

162) Nogues J, Schuller I K, *J. Magn. Magn.Mater.,* **192** 203 (1999).

163) Nogues J, Skumryev V, Sort J, Stoyanov S, Givord D, *Phys. Rev. Lett.,* **97** 157203 (2006).

164) Nogues J, Sort J, Langlais V, Skumryev V, Surinach S, Munoz J S, Baro M D, *Phys. Rep.,***422** 65 (2005).

165) Odenbach S, Handbook of Magnetic Materials, (Elsevier, Amsterdam, 2006).

166) Oliveira A A S, Teixeira I F, Ribeiro L P, Tristao J C, Dias A, Lago R M, *J. Braz. Chem. Soc.,***21** 2184 (2010).

167) Park J, Kang E, Son S U, Park H M, Lee M K, Kim J, Kim K W, Noh H-J, Park J-H,. Bae C J,Park J-G Hyeon T, *Adv. Mater.,***17** 429 (2005).

168) Patange M, Biswas S, Yadav A K, Jha S N, BhattacharyyaD,*Phys. Chem. Chem. Phys*., **17** 32398 (2015).

169) PaulG , Principles and applications of thermal analysis , John Wiley &Sons USA (2008).

170) Peng D, Tao-tao Y, Xin-xin Y, Zhi-man B, Ming-zai Wu, *Nanoscale Res. Let.,***11** 226 (2016).

171) Peng S, Fan X, Li S, Zhang J, J. Chil. Chem. Soc., **58**2213 (2013).

172) Peng T, Liu X, Dai K, Xiao J, Song H, *Mater. Res. Bull.,* 41 1638 (2006).

173) Peternel I T , Koprivanac N, LocaricBozic A M , Kusic H M, *J.Hazardous Mat.*, **148** 477 (2007).

174) Pino A P, Gyorgy E, Hussain S, Andujar J L, Pascual E, Amade R, Bertran E, *J.Mater. Sci.,***52** 4002 (2017).

175) Polisetti S, Deshpande P A, Madras G *Ind. Eng. Chem. Res.*, **50** 12915 (2011).

176) Pozio A, Masci A, Pasquali M, *Solar Energy,***136** 590 (2016).

177) Qamar M, Gondal M A, Yamani Z H, *J. Mol. Cat. A: Chem.,***341** 83 (2011).

178) Qiu S, Zhou Z, Dong J, Chen G, *J. Tribol.,***123** 441 (2001).

179) Rahdar A, Aliahmad M, Azizi Y, *J.Nano.Struct.,***5** 145 (2015).

180) Rajesh A, Raja MM, Gurunathan K, *Acta Metall. Sin.,***27**253 (2014).

181) Rajesh J T, Praveen K S, Ramachandra G K, Raksh V J , *Sci. Tech. Adv. Mat.,* **8** 455 (2007).

182) Rasheed A, Mahmood M, Ali U, Shahid M, Shakir I, Haider S, Khan M A, Warsi M F, *Ceram. Int.*, **42**15747 (2016).

183) Reddy K R, Gomes V G, Hassan M, *Mater. Res. Express,***1** 015012 (2014).

184) Reddy K R, Hassan M, Gomes V G, *Appl. Catal. A: Gen.,***489** 1 (2015).

185) Reddy K R, Karthik K V, Benaka Prasad S B, Soni S K, Jeong H M, Raghu AV, *Polyhedron,* **120** 169 (2016).

186) Reddy K R, Lee K-P, Gopalan A I, *Colloid and Surf. A: Physicochem. Eng. Aspects,***320** 49 (2008).

187) Reddy K R, Lee K-P, Iyengar A G, *J. Appl. Polymer Sci.*,**104**4127 (2007).

188) Reddy K R, Sin B C, Yoo C H, Park W, Ryu K S, Lee J-S, Sohn D, Lee Y, *ScriptaMaterialia,* **58** 1010 (2008).

189) Rellinghaus B, Stappert S, Wassermann E F, Sauer H, Spliethoff B, *Eur. Phys. J. D,* **16** 249 (2001).

190) Ren Z, Meng N, Shehzad K, Xu Y, Qu S, Yu B,Luo J K, *Nanotechnology,***26** 065706 (2015).

191) Roca A G, Costo R, Rebolledo A F, Veintemillas-Verdager S, Tartaj P, Gonzalez C T, Morales M P, Serna C J, *J.Phys.D. Appl.Phys*.,**42** 224002(2009).

192) Rossi L M, Garcia M A S, Vono L L R, *J. Braz. Chem. Soc*., **23** 1959 (2012).

193) Saghatforoush L A, Hasanzadeh M, Sanati S, Mehdizadeh R, *Bull. Kor. Chem. Soc.*, **33**2613 (2012).

194) Sahebian S, Zebarjad S M, Vahdati K J, Lazzeri A, *Int. Nano Lett*., **6** 183 (2016).

195) Sakiyama K , Koga K , Seto T, Hirasawa M , Orii T, J. *Phys. Chem. B,***108** 523 (2004).

196) Samadi M, Zirak M, Naseri A, Khorashadizade E,

197) Sato H, Minami T, Takata S, Yamada T, *Thin Solid Films,* **236** 27(1993).

198) Schroder D K, Rubin LG, *Phys.Today,***44** 107(1991).

199) Schroder D K, SemiconductorMaterial and Device Characterization. Wiley Interscience, New York (1998).

200) Schron A, Rodl C, Bechstedt F, *Phys. Rev. B,***86** 115134 (2012).

201) Sene C F B, McCann M C, Wilson R H, Crinter R, *Plant Physiol*.,**106** 1623 (1994).

202) Shajira P S, GaneshchandraPrabhu V, JunaidBushiri M, *J. Phys. Chem. Solids,***87** 244 (2015).

203) Shan G, Fu Y, Chu X, Chang C, Zhu L, *J. Colloid. Interf.Sci.,* **444** 123 (2015).

204) Shanaj B R , John X R*, J.Theor. Comput.Sci.*,**3**1000149 (2016).

205) Sharma P, Lotey G S, Singh S, VermaN K*,J .Nanopart. Res.,***13**2553 (2011).

206) Sharma S K, Vargas J M, Knobel M, Pirota K R, Meneses C T, Kumar S, Lee C G, Pagliuso P G, Rettori C, *J. Appl. Phys.,***107** 09D725 (2010).

207) Showkat A M, Zhang Y-P, Kim M S, Gopalan A I, Reddy K R, Lee K-P, *Bull.Kor. Chem. Soc.,* **28** 1985 (2007).

208) Shukla N, Nigra M M, Nuhfer T, Bartel M A, Gellman A J, *Nanotechnology,* **20** 065602 (2009).

209) Silva W M, Ribeiro H, Seara L M, Calado H D R, Ferlauto A S, Paniago R M, Leite C F,Silva G G, *J. Braz. Chem. Soc.,***23** 1078 (2012).

210) Skumryev V, Stoyanov S, Zhang Y, Hadjipanayis G, Givord D, Nogue´s J, *Nature,* **423**850(2003).

211) Smit J, Wijn H P J, *Ferriets*, Wiley, (1959).

212) Smith D J, *Reports Prog.Phys.,***60** 1513 (1997).

213) Song P, Wen D, Guo Z X, Korakianitis T, *Phys.Chem.Chem.Phys*., **10** 5057 (2008).

214) Song X, Gao L, *J. Phys. Chem., C***112** 15299 (2008).

215) Sort J, Nogues J, Amils X, Surinach S, Munoz J S, Baro M D, *Appl. Phys. Lett.,***75** 3177 (1999).

216) Suzuki M, Kudo K, Kojima K, Yasue T, Akutsu N, Dino W A,Kasai H, Bauer E, Koshikawa T, *J. Phys. Cond.Mat.,***25**406001 (2013).

217) Tanase M, Zhu J G, Liu C, Shukla N, Klemmer T J, Weller D, Laughlin D E, *Met.Mat.Trans. A,* **38** 798 (2007).

218) Teixeira A P C, Tristao J C, Araujo M H, Oliveira L C A, Moura F C C, Ardisson J D, Amorim C C, Lago R M, *J. Braz. Chem. Soc.,***23**1579 (2012).

219) Tian D, Li N,Wang F F, Mu S L, Li D Y, Xia G F, *ECS Electrochem. Lett.*,**1** H5 (2012).

220) Tiwari S D, Rajeev K P, *Thin Solid Films*, **505** 113 (2006).

221) Tiwari S D, Rajeev K P,*Phys. Rev. B,***72** 104433 (2005).

222) Toro J D, Marques D P, Muniz P, Skumryev V, Sort J, Givord D, Nogues J, *Phys. Rev. Lett.,***115** 057201 (2015).

223) Trapalis A, Todorova N, Giannakopoulou T, Boukos N, Speliotis T, Dimotikali D, Yu J, *Appl. Catal.BEnv.,***180** 637 (2016).

224) Tsai C-W, Chen H M, Liu R-S, Asakura K, Chan T-S, *J. Phys. Chem. C,* **115** 10180 (2011).

225) Tundermann J H, Tien J K, Howson T E, In:Kirk -Othmer encyclopedia of chemical technology **17** (2005).

226) Uchikoshi T, Sakka Y, Yoshitake M, Yoshihara K, *Nanostruct .Mater*., **4** 199 (1994).

227) Unger E, Duesberg G S, Liebau M, Graham A P, Seidel R, Kreupl F, Hoenlein W, *Appl. Phys. A*, **77** 735 (2003).

228) Wan X, Yuan M, Tie S-L, Lan S, *Appl. Surf. Sci.,***277** 40 (2013).

229) Wang H, Wang E, Liu Z, Gao D, Yuan R, Sun L, Zhu Y, *J. Mater. Chem., A3*266 (2015).

230) Wang S M, Leung C W, Chan P K L, *Appl. Phys. Lett.,* **97** 023511 (2010).

231) Wang W, Liu Y, Xu C, Zheng C, Wang G, *Chem. Phys. Lett.,***362** 119 (2002).

232) Watt I M, The Principals and Practice of Electron microscopy 2nd edition; Cambridge University Press (1997).

233) Watts P C P, Hsu W K, Randall D P, Kotzeva V, Chen G Z, *Chem. Mater.*, **14** 4505 (2002).

234) Wei X, Skomski R, Balamurugan B, Sellmyer D, *J. Appl. Phys.,***107** 09B516 (2010).

235) Weiss P, *Compt. Rend.,***143**1136(1906).

236) Wen W, Wu J-M, *ACS Appl. Mater. Interf.*,**3** 4112 (2011).

237) Wu X, Xing W , Zhang L, Zhuo S, Zhou J, Wang G, Qiao S, *Powder Technol*., **224** 162 (2012).

238) Wu Y H , Qiao P W , Qiu J J, Chong T C, Low T-S, *Nano. Lett.*,**2** 161 (2002).

239) Wu S-H, Chen D-H, *J.Coll.Inter. Sci.,***259** 282 (2003).

240) Wu Y, He Y, Wu T, Chen T, WengW,Wan H, *Mater. Lett.,***61**3174 (2007).

241) Wu Z G, Monoz M, Montero O, *Adv. Powder Technol*., **21**165 (2010).

242) Xiang X, Zua X T, Zhu S, Wang L M, *Appl. Phys. Lett.,***84** 52 (2004).

243) Xu C, Sun J,Gao L *J. Power Sources,***196** 5138 (2011).

244) XueGI ,*Prog. Polym. Sci.,***22**313 (1997).

245) Yan J, Wei T, Shao B, Fan Z, Qian W, Zang M, Wei F, *Carbon*, **48**487 (2010).

246) Yan X, Tian L, Chen X, *J. Power Sources,***300** 336 (2015).

247) Yan X, Tong X, Wang J, Gong C , Zhang M, Liang L, *Mater. Lett.*,**106** 250 (2013).

248) Yang H X, Dong Q F, Hu X H, Ai X P, Li S X, *J. Power Sources,* 79 256 (1999).

249) Yao X-J, He X-M, Song X-Y, Ding Q, Li Z-W, Zhong W, Au C-T, Du Y-W,*Phys.Chem.Chem.Phys.,* **16** 6925 (2014)

250) Yoon M, Kim Y, Kim Y M, Volkov V, Song H J, Park Y J, Park I-W, *Mater. Chem. Phys.,* **91** 104 (2005).

251) Yousefi S R, Ghanbari D, Salavati-Niasari M, Hassanpour M,

252) Yuan C L, *J. Phys. Chem. C*, **114** 2124 (2010).

253) Yuan F, Ni Y, Zhang L, Yuan S, Wei J, *J. Mater. Chem.A,* **1**8438 (2013).

254) Yung T-Y, Huang L-Y, Chan T-Y, Wang K-S, Liu T-Y, Chen P-T,Chao C-Y, Liu L-K,*Nanoscale Res. Let.,* **9**444 (2014).

255) Zahraei F, Rahimi K, Yazdani A, *Int. J. Nano Dimens.,* **6**371 (2015).

256) Zhang P, Hong R Y, Chen Q, Feng W G*, Powder Techn*., **253** 360 (2014).

257) Zhang Y-P, Lee S-H, Reddy K R, Gopalan A I, Lee K-P, *J. Appl. Polymer Sci.*, **104** 2743 (2007).

258) Zhao D F, Yang H, Li R S, Ma J Y, Feng W J, *Mater. Res. Innovations,* **18**519 (2014).

259) Zhao X Q, Liang Y, Hu Z Q, Liu B X *J. Appl. Phys.,* **80** 5857 (1996).

260) Zhou C H, Ma H T, Wang L, *Corros.Sci.*, **52** 210 (2010).

261) Zhou C,Szpunar J A, Cui X, *ACS Appl. Mat. Interfaces,* **8** 15232 (2016).

262) Zhou Y Z, Chen J S, Tay B K, Hu J F, Chow G M, Liu T, Yang P, *Appl. Phys. Lett.,* **90** 043111 (2007).

263) Zhu H, Chen X, Zheng Z, Ke X, Jaatinen E, Zhao J, Guo C, Xie T, Wang D, *Chem.Commun.*, (2009) 7524.

264) Zorkipli N N M, Kaus N H M, Mohamad A A*, Procedia Chemistry,* **19** 626 (2016).